

Title	High speed optical communication systems: From modulation formats to radically new fibres
Authors	Mac Suibhne, Naoise C.
Publication date	2014
Original Citation	Mac Suibhne, N. 2014. High speed optical communication systems: From modulation formats to radically new fibres. PhD Thesis, University College Cork.
Type of publication	Doctoral thesis
Rights	© 2014, Naoise Mac Suibhne. - <a href="http://creativecommons.org/licenses/by-nc-nd/3.0/">http://creativecommons.org/licenses/by-nc-nd/3.0/</a>
Download date	2025-08-01 05:43:29
Item downloaded from	<a href="https://hdl.handle.net/10468/1895">https://hdl.handle.net/10468/1895</a>

# High Speed Optical Communication Systems

## From Modulation Formats to Radically New Fibres

Naoise Mac Suibhne

BE

105464196



NATIONAL UNIVERSITY OF IRELAND, CORK

SCHOOL OF ENGINEERING

DEPARTMENT OF ELECTRICAL AND ELECTRONIC ENGINEERING

TYNDALL NATIONAL INSTITUTE

**Thesis submitted for the degree of  
Doctor of Philosophy**

2014

Supervisors: Prof Andrew Ellis

Dr Alan Morrison

Dr Fatima Garcia Gunning

Head of Department/School: Prof Nabeel Riza

Research supported by Science Foundation Ireland  
and EU Framework 7 under the project MODEGAP

## Contents

List of Figures . . . . .	v
List of Tables . . . . .	xi
Acknowledgements . . . . .	xii
Abstract . . . . .	xiii
<b>1 Introduction</b>	<b>1</b>
1.1 Historical Perspective . . . . .	2
1.2 Capacity Limits . . . . .	4
1.3 Objectives of This Thesis . . . . .	6
1.3.1 Future Improvements in SMF . . . . .	7
1.3.2 Advantages of New fibre Technology . . . . .	7
1.4 Outline of This Thesis . . . . .	8
<b>2 Fundamentals</b>	<b>10</b>
2.1 Optical Fibres . . . . .	10
2.1.1 Mode Support . . . . .	11
2.1.2 Band Gap Fibre . . . . .	13
2.2 Linear Fibre Impairments . . . . .	15
2.2.1 Fibre attenuation . . . . .	15
2.2.2 Dispersion . . . . .	16
2.2.2.1 Intra-mode Dispersion . . . . .	17
2.2.2.2 Inter-mode Dispersion . . . . .	18
2.3 Nonlinear Fibre Impairments . . . . .	18
2.3.1 Stimulated Inelastic Scattering . . . . .	19
2.3.1.1 Stimulated Raman Scattering . . . . .	19
2.3.1.2 Stimulated Brillouin Scattering: . . . . .	20
2.3.2 Optical Fibre Nonlinearity . . . . .	21
2.3.2.1 Self Phase Modulation . . . . .	22
2.3.2.2 Cross Phase Modulation . . . . .	22
2.3.2.3 Four Wave Mixing . . . . .	23
2.4 Modulation Formats . . . . .	25
2.4.1 Modulators . . . . .	25

2.4.2	Intensity Modulation . . . . .	28
2.4.3	Phase Modulation . . . . .	29
2.5	Information Theory . . . . .	31
2.5.1	Capacity Limits . . . . .	32
2.6	Chapter Summary . . . . .	35
<b>3</b>	<b>Power Efficient Modulation Formats</b>	<b>36</b>
3.1	Modulation Formats Dimensionality . . . . .	37
3.2	Visualisation Methods . . . . .	39
3.2.1	Simplexes . . . . .	40
3.2.2	DP-QPSK in Four Dimensions . . . . .	41
3.2.3	PS-QPSK in Four Dimensions . . . . .	42
3.3	What is Meant by Power Efficient? . . . . .	44
3.3.1	Comparing the Efficiency of Modulation Formats . . . . .	44
3.3.2	Power Efficient Modulation Formats in the Literature . . . . .	46
3.4	PS QPSK and Experiments . . . . .	46
3.4.1	Constructing a PS-QPSK Transmitter . . . . .	47
3.4.2	Back-to-back Sensitivity Comparison . . . . .	48
3.4.3	Receiver DSP Algorithms . . . . .	50
3.4.4	Transmission Experiment . . . . .	53
3.5	Chapter Summary . . . . .	57
<b>4</b>	<b>Benefits and Limits of Multi Mode Fibres</b>	<b>58</b>
4.1	Multi-mode and Few Mode Fibres . . . . .	59
4.1.1	Fibre in Use . . . . .	60
4.2	Investigations into Stimulated Brillouin Scattering in FMF . . . . .	62
4.2.1	Results of SBS Investigations . . . . .	63
4.3	Investigations into SPM Effects . . . . .	68
4.3.1	Initial Experimental Setup . . . . .	69
4.3.2	Phase Measurements Using a Frequency Discriminator Technique . . . . .	71
4.3.3	Initial Results . . . . .	72
4.3.4	Improvements to the Experimental Setup for SPM Measurements . . . . .	80
4.3.5	Results Using Mode Interrogator Technique . . . . .	81



4.4	Investigations into FWM Effects . . . . .	84
4.4.1	Experimental Technique for Measuring FWM in FMF . . . . .	85
4.4.2	FWM Numerical Model for FMF . . . . .	88
4.4.3	Experimental Results Comparison with Multi-mode FWM Model . . . . .	90
4.5	New Capacity Limits . . . . .	93
4.5.1	Choosing a Radically New Fibre . . . . .	94
<b>5</b>	<b>Transmission Over Hollow Core Photonic Bandgap Fibre at 2<math>\mu</math>m</b>	<b>96</b>
5.1	Moving to 2 $\mu$ m . . . . .	97
5.1.1	Transmission Windows and Loss Reduction . . . . .	97
5.2	2 $\mu$ m System Components . . . . .	100
5.2.1	2 $\mu$ m Single Mode Lasers . . . . .	101
5.2.2	2 $\mu$ m Photodiodes . . . . .	103
5.2.3	Thulium-Doped Fibre Amplifiers . . . . .	106
5.2.4	Hollow Core Photonic Bandgap Fibres . . . . .	108
5.2.5	Passive Components . . . . .	109
5.2.5.1	Couplers . . . . .	110
5.2.5.2	Filters . . . . .	110
5.2.5.3	Patch Cords, Polarisation Controllers and Attenuators . . . . .	111
5.3	System Experiments . . . . .	112
5.3.1	Performance of 2 $\mu$ m Subsystems . . . . .	115
5.3.2	Transmission Over Hollow Core Fibre . . . . .	117
5.4	Chapter Summary . . . . .	120
<b>6</b>	<b>Conclusions</b>	<b>121</b>
6.1	Future Improvements in SMF . . . . .	121
6.2	Advantages of New Fibre Technology . . . . .	122
<b>A</b>	<b>Author's Publications</b>	<b>140</b>
A.0.1	Publications Not Related to This Thesis . . . . .	141

I, Naoise Mac Suibhne, certify that this thesis is my own work and I have not obtained a degree in this university or elsewhere on the basis of the work submitted in this thesis.

*Naoise Mac Suibhne*

## List of Figures

1.1	Visual parallels between neural and optical networks showing diffusion spectral imaging of white matter fibres of a brain (left) and to the right an "internet map" of routers and hosts connected to the internet showing Asia in red, Europe/Middle East/Central Asia/Africa in green, North America in blue, Latin America and Caribbean in yellow, private addresses in cyan and unknown addresses in white . . . . .	3
1.2	Area cartogram of global internet users where a countries area corresponds to number of internet users. Country colour corresponds to internet penetration rates in that country, red countries having high penetration rates. . . . .	4
1.3	Shannon Capacity limit relation between spectral efficiency and power (blue). The red points show the year each spectral efficiency is required based on current growth. . . . .	6
2.1	Illustration of electric field mode profiles for the fundamental modes. Arrows indicate the direction of the electric field. . . . .	11
2.2	Mode profiles for LP modes showing $\pi$ phase shift between red and blue segments . . . . .	12
2.3	Normalised propagation constant as a function of normalised frequency for a few-mode fibre. Colours correspond to modes with near identical propagation constants that form LP modes as labelled . . . .	13
2.4	Cross section of a HC-PBGF. Labels indicate areas of interest. . . . .	14
2.5	Basic loss spectrum of a typical SMF indicating the contribution of major loss mechanisms. Including intrinsic absorption (dotted lines), Rayleigh scattering (black line) and extrinsic absorption . . . . .	16
2.6	Plan view of (a) Mach-Zehnder modulator structure and (b) Nested Mach-Zehnder modulator. . . . .	26
2.7	Bit sequence encoded in (a) non-return-to-zero and (b) 50% return-to-zero where the amplitude returns to zero for 50% of the bit period, $T$ . . . . .	28
2.8	Constellation diagrams showing (a) OOK, (b) 2 Phase shift keying and (c) QPSK. The dotted circles represent a region of constant amplitude. . . . .	29
2.9	Block diagram of a generic communication system . . . . .	31
2.10	Linear and nonlinear Shannon limits shown in red and black traces respectively. The plot shows the relationship between information spectral density and power spectral density for an optical system with characteristics shown in Table 2.2. . . . .	33
3.1	Illustration of real (solid line) and imaginary (dotted line) wavefunctions propagating in the x- and y-polarisation, shown in red and blue respectively. . . . .	38

3.2	Simplexes for increasing number of dimensions $N$ .	40
3.3	Construction of a four dimensional cubic constellation.	41
3.4	DP-QPSK visualised in four dimensions using stereographic projection.	42
3.5	PS-QPSK viewed as a subset of DP-QPSK, showing all symbol states relevant to PS-QPSK.	42
3.6	Triadic constellation for increasing dimensions	43
3.7	Two Dimensional constellations for increasing number of symbol states $M$ .	44
3.8	PS-QPSK Transmitter (left) and DP-QPSK Transmitter (right)	48
3.9	Experimental set-up for PS-QPSK back-to-back measurements. For DP-QPSK, a polarization multiplexing stage replaces the polarisation modulator, and 10.125Gb/s data signals are applied to the QPSK modulator.	48
3.10	Eye diagrams of PS-QPSK in each polarisation (left) and QPSK (right).	49
3.11	Back-to-back measurements for PS-QPSK and DP-QPSK	50
3.12	Offline digital signal processing flow chart.	50
3.13	Recovered constellation diagrams for back-to-back measurement of (a) 40.5Gb/s DP-QPSK and (b) 40.5Gb/s PS-QPSK.	52
3.14	Experimental set-up for WDM transmission experiments over $10 \times 100$ km of standard SMF.	53
3.15	WDM spectrum of PS-QPSK after transmission over 1000 km of fibre.	54
3.16	BER versus received OSNR for PS-QPSK after WDM transmission over $10 \times 100$ km SSMF.	55
3.17	Required OSNR for PS-QPSK and DP-QPSK (both at 40.5Gb/s) after WDM transmission over $10 \times 100$ km SMF for a range of launch powers into the spans.	56
4.1	Depiction of improved nonlinear performance and greater total capacity of FMFs (green) compared to standard SMF (black). The solid, dashed, dotted and dot-dashed lines correspond to the $LP_{01}$ , $LP_{02}$ , $LP_{11}$ and $LP_{21}$ respectively. The linear Shannon limit is depicted by the blue curve	60
4.2	Experimental setup for experimental investigations into SBS in FMF. LO is used as a local oscillator for a heterodyne technique explained in the text while port 3 of the $2 \times 2$ coupler allows back-reflected power to be measured.	62
4.3	Result of SBS threshold measurement with experimental data measuring back-reflected power is shown in black while the condition for stimulated Brillouin scattering is shown in red for a value of $\mu = 0.01$ based on Equation 4.1.	63

4.4	Surface plot showing all optical spectra of measured back-reflected power. Both the local oscillator (LO) seed pump and the SBS gain peak are labelled. . . . .	65
4.5	Measured SBS gain (black squares) compared against two analytical models for SBS in both the depleted (green) and undepleted (red) pump regime. . . . .	66
4.6	Measured RF spectrum of SBS gain (squares) with Lorentzian fit (red). . . . .	67
4.7	Experimental setup for investigating SPM using a SMF to FMF splice (a) where a frequency discriminator method is implemented using a WSS (b). . . . .	69
4.8	Effective index of four mode fibre in use including typical intensity profiles for each mode (insets). . . . .	70
4.9	Electrical setup for synchronisation between the MLL and receiver oscilloscope. . . . .	70
4.10	Screen capture showing temporally separated pulses corresponding to $LP_{01}$ (left) and $LP_{02}$ (right) modes after 20 km transmission . . . . .	72
4.11	Measured (a) temporal and (b) phase information for optical pulse before propagating through fibre for increasing powers. The zero time corresponds to the central intensity of the pulse. . . . .	74
4.12	Measured (a) temporal and (b) phase information for optical pulse corresponding to the $LP_{01}$ mode after 20 km transmission for increasing powers. The zero time corresponds to the central intensity of the pulse. . . . .	75
4.13	Measured (a) temporal and (b) phase information for optical pulse corresponding to the $LP_{02}$ mode after 20 km transmission for increasing powers. The zero time corresponds to the central intensity of the pulse. . . . .	76
4.14	Temporal pulse profiles for experimental (blue) and model simulations (red) assuming equal power coupled between modes. Each column refers to input, $LP_{01}$ and $LP_{02}$ outputs with each row corresponding to low power and high power launch conditions. . . . .	77
4.15	FWHM measurements for $LP_{01}$ (black) and $LP_{02}$ (red) modes. The measured results (circles and squares) are compared to a basic simulation model (asterisks and crosses) and a single-step split-step Fourier method (solid lines). . . . .	78
4.16	Schematic diagram (upper) and picture (lower) of improved experimental setup with mode interrogator. . . . .	80
4.17	Experimentally measured pulse input data. (a) Waterfall plot and (b) contour plot of pulse evolution with increasing average launch power . . . . .	81
4.18	Experimentally measured pulse data for $LP_{01}$ . (a) Waterfall plot and (b) contour plot of pulse evolution with increasing average launch power . . . . .	82
4.19	Experimentally measured pulse data for $LP_{11}$ . (a) Waterfall plot and (b) contour plot of pulse evolution with increasing average launch power. . . . .	82

4.20	Simulated model data. (a) Contour plot of $LP_{01}$ (b) $LP_{11}$ pulse evolution with increasing average launch power. . . . .	83
4.21	FWHM comparison of $LP_{11}$ (left) and $LP_{11}$ (right) for both experimentally measured (black squares) and simulated model data (red circles and crosses). . . . .	84
4.22	Relative group delay as a function of frequency for four modes in a FMF showing matched velocity between four modes (green circles) associated with higher inter-mode FWM effects, red circle indicates a condition where intra-mode FWM would dominate. . . . .	85
4.23	Conceptual illustration showing (a) the logarithmic bandwidth dependence with intra-mode (red) FWM effects and (b) the contribution of inter-mode FWM as bandwidth is increased, breaking the logarithmic bandwidth dependence. . . . .	86
4.24	Conceptual representation of measurement technique using filtered ASE (dashed black line) showing (a) intra-channel FWM (red) reducing central notch extinction ratio while for wider bandwidths (b) inter-mode FWM (dashed green) reduces the central notch extinction ratio even further. . . . .	87
4.25	Schematic diagram of experimental set up (lenses and positioning stages at the ends of few mode fibre are omitted for clarity and are similar to that shown in Figure 4.16). . . . .	87
4.26	Contour plots of $\eta_{ijkn}$ on a log scale as a function of effective area and frequency offset for a 5 THz WDM signal for four separate fibre designs with DGDs of (a) 102 ps/km (b) 210.8 ps/km (c) 223.2 ps/km and (d) 406.3 ps/km with the points on each graph corresponding to conditions where nonlinear noise is present for the various fibres. . . . .	90
4.27	Summed FWM noise as a function of WDM bandwidth, normalised to the $LP_{01}$ mode, for four separate fibre designs with DGDs of (a) 102 ps/km (b) 210.8 ps/km (c) 223.2 ps/km and (d) 406.3 ps/km . . .	91
4.28	Typical Spectrum measurement on central 50 GHz notch for a range of total bandwidths at (a) fibre input and (b) output of the fibre interrogating $LP_{01}$ mode . . . . .	91
4.29	Comparison of experimental data (dots) to FWM model (lines) for $LP_{01}$ (blue) and $LP_{11}$ (red) modes. The dotted line indicates expected FWM signal neglecting inter-mode effects. . . . .	92
4.30	Calculated nonlinear Shannon limit for modes of a FMF neglecting inter-mode FWM (black) and including inter-mode FWM (red). The blue trace shows the nonlinear limit of SMF for comparison. . . . .	94
4.31	Nonlinear Shannon limit for each mode of a FMF (red) based on new numerical model. Blue trace shows nonlinear limit for SMF and green trace the limit for HC-PBGF operating at 1550 nm with 0.2 dB loss. . .	95

5.1	Historical progress of loss reduction in solid core fibres (red), Hollow Core Photonic Bandgap fibres at 1.5 $\mu\text{m}$ (green) and Hollow Core Photonic Bandgap fibres at 2 $\mu\text{m}$ (blue). Loss divided by the fibre low-loss bandwidth ("window" bandwidth) is used to compare fibres operating in different wavelengths and provides a figure of merit to compare fibres with varying low-loss bandwidths. . . . .	98
5.2	Fibre loss illustrating the traditional low-loss windows (0.8 $\mu\text{m}$ , 1.3 $\mu\text{m}$ and 1.5 $\mu\text{m}$ ) with impurity losses as described in Chapter 2. The practical low-loss SMF is shown in green. Red traces show the predicted fourth transmission window for hollow core fibre at 2 $\mu\text{m}$ where infrared absorption is reduced and surface scattering ( $\sim \lambda^{-3}$ ) dominates over Rayleigh scattering . . . . .	100
5.3	SEM image of etched waveguide structure. . . . .	101
5.4	Laser characteristics: (a) Spectrum of a laser operating at 2005nm with $\approx 50$ dB SMSS, measured at 20°C with 100 mA bias current. (b) Output optical power as a function of bias current, threshold at 16 mA. . . . .	102
5.5	$s_{21}$ measurements of packaged 2 $\mu\text{m}$ laser, indicating a 3dB bandwidth $\approx 3$ GHz. . . . .	102
5.6	Schematic of 2 $\mu\text{m}$ photodiode layer structure. . . . .	104
5.7	Image of 2 $\mu\text{m}$ photodiode in unsealed package. . . . .	104
5.8	Setup for measuring $s_{21}$ of 2 $\mu\text{m}$ detector with optical paths shown in black and electrical paths shown in red. . . . .	105
5.9	Frequency response of 2 $\mu\text{m}$ photodiode, attained from $S_{21}$ measurements. . . . .	106
5.10	Comparison of first generation TDFA and EDFA ASE bandwidth. The sudden dips in the TDFA spectrum at high frequencies is likely due to gas absorption in the OSA. . . . .	107
5.11	TDFA Block Diagram. . . . .	107
5.12	(a) Gain and (b) Noise Figure Performance of first generation TDFA. . . . .	108
5.13	SEM image of the 19-cell hollow core fibre. . . . .	108
5.14	Plot of HC-PBGF transmission loss (red) along with ASE gain spectrum of TDFA (black). Green, blue and grey traces show intensity lines for HCl, H <sub>2</sub> O and CO <sub>2</sub> respectively. . . . .	109
5.15	Filter characterisation with optical spectrum at 0.1 nm resolution where the output spectrum of a 4:1 combiner is shown in the black traces of (a) and (b). Red traces taken at the return port of the circulator using two separate Bragg gratings to filter 2004.79 nm and 1997.64 nm channels in (a) and (b) respectively. . . . .	110
5.16	Plot of attenuation as a function of input power showing a nonlinear relation, particularly at high input powers. . . . .	112

5.17	Experimental setup showing (a) Transmitter, (b) Channel consisting of 290m of HC-PBGF and (c) Receiver. . . . .	112
5.18	(a) S21 measurement of the external modulator at 1.5 $\mu$ m (blue) and at 2 $\mu$ m (red). (b) Spectrum showing the four channel WDM transmitter measured at the output of the 4:1 combiner with 0.1nm resolution bandwidth. . . . .	113
5.19	Modulator output for four clock frequencies applied to the modulator RF port. The four clock frequencies were (a)2.5 GHz, (b)5 GHz, (c)7 GHz and (d)10 GHz. . . . .	114
5.20	Laser output for three clock frequencies applied directly to the laser showing a reduced response for higher frequencies. . . . .	114
5.21	Picture of experimental setup with visible components labelled. . . . .	116
5.22	BER measurements as a function of received power for (a) directly modulated BPSK Fast-OFDM channels and (b) externally modulated NRZ OOK channel for back-to-back (open symbols) and over 50m solid core Nufern fibre (solid symbols) . . . . .	117
5.23	Eye diagram of externally modulated channel (top row) before (left) and after (right) transmission. Bottom row shows constellation diagram for a directly modulated BPSK Fast-OFDM channel before (left) and after (right) transmission. . . . .	118
5.24	Bit error rate results for directly modulated (a) and externally modulated channels (b) for back-to-back (open symbols) and over 290 metres HC-PBGF (closed symbols). . . . .	119
5.25	(a)Spectrum of all four channels before (black) and after (red) transmission. (b) Eye diagram of externally modulated channel after transmission.(c) Eye diagram of directly modulated channel at 2004.79 nm. . .	120



## List of Tables

1.1	Internet and mobile cellular penetration . . . . .	5
2.1	Fundamental mode combinations for LP mode formation . . . . .	12
2.2	Data used to seed nonlinear Shannon models . . . . .	34
3.1	Truth Table to achieve PS-QPSK using the four data inputs of a DP-QPSK modulator (D1-D4) . . . . .	47
4.1	Data for OFS few mode fibres. Values for dispersion, dispersion slope and effective area, at 1550nm, are calculated from the index profile for all fibres. . . . .	61
4.2	Data used to seed nonlinear Shannon models . . . . .	93
5.1	Comparison of fibres since the 1960s with noteworthy achievements in solid core and hollow core fibre fabrication. . . . .	97
5.2	Key characteristics of the fibre used for transmission at 2 $\mu$ m . . . . .	109

## **Acknowledgements**

It sounds a cliché but there really are too many people to thank so if you are not mentioned I apologise. First of all, I would like to thank my parents for their efforts to raise me as best they could, they continue to inspire me daily to become more honest, hard-working and fervently optimistic. To my sister, Saorlaith, who will always be smarter than me no matter how hard I try!

To my supervisors, Andrew Ellis for setting a decent standard for research and more importantly for keeping research fun, I will find a way to repay you someday. To Fatima Gunning who is the number one person to have on your team in times of crisis, many times during my thesis you helped beyond the call of duty. Both Andrew and Fatima planted the seeds to all my research output to date. Your training was the best I could have ever hoped for and I hope that we will get many opportunities to work together in the future. I hope my future exploits will make you both proud. To Alan Morrison who understated how helpful he was, especially during the write-up phase and to everyone in the photonic systems group who helped me through... Thank you!

During my PhD I had the privilege to work with several people in AT&T Labs in New Jersey. Lynn Nelson thank you for all your help and patience, only as time goes on do I realise how much you've helped my understanding. Also, to all the others I worked with in AT&T thank you all!

I would like to thank everyone I worked with in the Tyndall National Institute, so many good minds under one roof. In particular I would like to thank Peter O'Brien, Brian Corbett, Paul Townsend and their students. Thanks to Martina Connolly for all her help in cutting through red tape.

All the colleagues and friends I made through the partners of the MODEGAP project, thank you for opening my mind to the research field at large.

I would like to thank all the visiting students for their invaluable help in the lab. Also, a special thanks to all the young scientists I spoke to while doing outreach, you kept things in perspective. Particularly, I would like to thank Regan Watts from DCU who contributed to some of the experiments and helped prof-read the thesis along with Stylianos Sygletos.

I would also like to thank Science foundation Ireland (SFI), and the European project MODEGAP for funding my efforts.

Helena, I didn't forget you, when the dust settles and the deadlines are hit or missed you are there, for that you have my eternal thanks.

Finally, to the reader, thank you for giving this document purpose. Now, "tread softly because you tread on my dreams".

Naoise.

## Abstract

High volumes of data traffic along with bandwidth hungry applications, such as cloud computing and video on demand, is driving the core optical communication links closer and closer to their maximum capacity.

At the start of my PhD studies, the research community was clearly identifying the coming approach of the nonlinear Shannon limit for standard single mode fibre [1, 2][3][4].

It is in this context that the work on modulation formats, contained in Chapter 3 of this thesis, was undertaken as part of an industrial placement with AT&T Labs in Middletown, New Jersey. The work investigates the proposed energy-efficient four-dimensional modulation formats. The work begins by studying a new visualisation technique for four dimensional modulation formats, akin to constellation diagrams. The work then carries out one of the first implementations of one such modulation format, polarisation-switched quadrature phase-shift keying (PS-QPSK). The experimental work demonstrated PS-QPSK in a typical terrestrial WDM system, where transmission of 40.5 Gbit/s over 1000 km was compared to dual-polarisation QPSK at the same bit rate.

When seeking to extend capacity in core networks even further it becomes necessary to investigate beyond standard single mode fibre at the potential of different fibres for high-capacity optical communication. During the time-frame of this thesis, interest in the research community began to grow in the area of novel fibre transmission, including few-mode fibre, multi-core fibre and hollow-core photonic band-gap fibre.

This thesis studies two potential next-generation fibres, few-mode and hollow-core photonic band-gap fibre. The area of few-mode fibres has garnered great interest of late with the potential of spatial division multiplexing to transmit data on each mode. While the larger core hints towards a higher nonlinear threshold. Chapter 4 studies ways to experimentally quantify the nonlinearities in few-mode fibre and assess the potential benefits and limitations of such fibres. It carries out detailed experiments to measure the effects of stimulated Brillouin scattering, self-phase modulation and four-wave mixing and compares the results to numerical models. This includes studies on the affects of cross-mode effects, particularly inter-mode four-wave mixing where a new closed-form approximation is experimentally verified. The work on few-mode fibre concludes by presenting capacity limit calculations of few-mode fibres based on closed-form approximation of multi-mode four wave mixing.

Chapter 5 investigates hollow-core photonic band-gap fibre, where it is predicted to have a low-loss minima at a wavelength of 2  $\mu\text{m}$ . To benefit from this potential low loss window requires the development of telecoms grade subsystems and components. This thesis investigates development and characterisation of these components, including lasers and high-speed detectors. The world's first wavelength division multiplexed (WDM) subsystem directly implemented at 2  $\mu\text{m}$  is presented. Followed by the world's first WDM transmission over hollow-core photonic band-gap fibre at 2  $\mu\text{m}$ .

To Mom,  
Dad,  
Saorlaith,  
and Helena.



Mac Suibhne, N. 2014. High speed optical communication systems: From modulation formats to radically new fibres. PhD Thesis, University College Cork.

Please note that Chapter 1 (pp.1-9) is unavailable due to a restriction requested by the author.

CORA Cork Open Research Archive <http://cora.ucc.ie>

## Chapter 2

# Fundamentals

This chapter will cover a brief introduction into the basic principles of optical communications. The information in this chapter will act as a foundation for many of the topics that will be expanded upon in the coming chapters. This will entail describing optical systems from the basic physical characteristics that govern their behaviour to more abstract theory on how optical communications convey information. The chapter will begin by describing the basic principles of optical fibre and the effects of signal propagation (Sections 2.1-2.3). The structure of when each topic is introduced is done so, in an effort, to avoid creating a false dichotomy. To this end some topics are introduced early with a more detailed explanation following some time later. The material starts by introducing the concept of electromagnetic modes before moving onto Section 2.2 and Section 2.3 that explain the physical attributes that govern fibre impairments where Section 2.3.2 reviews how high-power electromagnetic waves propagate through the fibre medium.

Section 2.4 will explain how modulation formats can be used to encode information onto an optical signal, including some examples of common modulation formats used in optical systems of today. Finally, a basic introduction into information theory in Section 2.5 will introduce topics such as the nonlinear Shannon limit and the basics governing the capacity of optical networks.

### 2.1 Optical Fibres

In recent years there has been a huge global research interest in the area of new optical fibres to increase the capacity of optical networks. Traditionally in optical communications standard single mode fibre (SMF) has been used almost exclusively in the core-network for optical communication systems (with some plastic optical fibres and multi-mode fibres being used in short haul and access networks). In optical com-

munications, engineers are constantly competing with the cost of a digger, or more specifically, the cost of excavating a track of ground to place a new length of fibre in the ground. To this end researchers and engineers attempt to increase capacity by upgrading the transmitters and receivers on either end of an installed optical link. Once this model of upgrading transmitters and receivers reaches a point of diminishing returns (and several people argue that this has already occurred!) then it is imperative for engineers to re-evaluate the channel in use and explore ways of improving the optical fibre so that the optimal fibre can be installed when the days-of-digging must begin. Some of the fibres under research include few mode fibre (FMF), multi-core fibre and hollow-core photonic band-gap fibre (HC-PBGF). This thesis assesses the potential of few-mode fibres and hollow-core photonic band-gap fibres as suitable replacements for SMF. The properties of FMF are very similar to that of standard SMF as the medium of propagation in both cases is silica, the properties that govern guidance in solid core fibres are discussed in Section 2.1.1. For HC-PBGF the principles of guidance are completely different to solid core fibres and are discussed in Section 2.1.2.

### 2.1.1 Mode Support

The signals propagating in an optical fibre are electromagnetic waves consisting of an electric field  $\mathbf{E}$  and magnetic field  $\mathbf{H}$  where the transverse electric (TE) consists of the magnetic field having a component in the direction of propagation with a transverse electric field. Conversely, TM modes correspond to the electric field in the direction of propagation with a transverse magnetic field. This is illustrated in Figure 2.1 where the electric field is plotted for each of the fundamental modes [19].

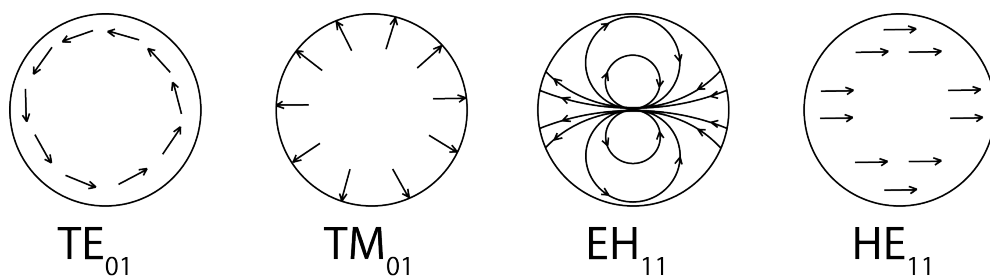


Figure 2.1: Illustration of electric field mode profiles for the fundamental modes. Arrows indicate the direction of the electric field based on [19, 20]

From here the fundamental four classes of modes are HE and EH (where the dominant contributor to the  $z$ -direction is designated the leading letter), TE and TM. For step index fibres, the effective index difference is small enough that the HE and EH modes propagate with almost identical propagation constants [20], these are known as the degenerate modes. The superposition of these degenerate modes correspond to various linearly polarised (LP) modes, leading to a well defined intensity across

the fibre cross-section. The generation of LP modes can be thought of as interference between the modes[21, 22]. The combination of the fundamental mode classes creates several solutions, with standing wave solutions being guided as LP modes, while all other solutions are no longer supported by the fibre, these include radiation modes, bend losses and coupling losses. Table 2.1 shows the contributing fundamental modes that make up the basic LP modes. The subscript notion for the linear polarised modes given by  $LP_{lm}$  where  $l$  and  $m$  correspond to the mode profile where  $l$  is related to the number of phase changes in the mode profile across its diameter. A depiction of this notation is shown in Figure 2.2 where  $m$  corresponds to the number of rings in the mode profile. This notation is different to that of the fundamental modes where the subscripts refer to the two dimensions of the cylindrical waveguide.

Table 2.1: Fundamental mode combinations for LP mode formation based on [21]

Mode Superposition	Fundamental mode contributors
$LP_{01}$	$HE_{11}$
$LP_{11}$	$HE_{21}, TE_{01}, TM_{01}$
$LP_{02}$	$HE_{12}$
$LP_{21}$	$HE_{31}, EH_{11}$

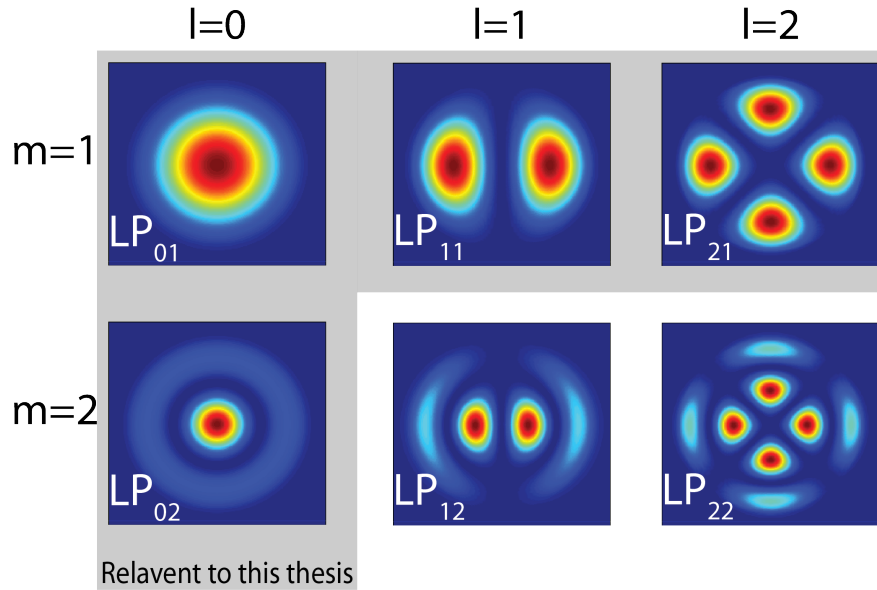


Figure 2.2: Mode profiles for LP modes showing  $\pi$  phase shift between red and blue segments

The  $V$  parameter is a parameter that takes into account core diameter and refractive index difference with a typical value of  $V < 2.4$  for single-mode operation. The single mode condition is determined by where the  $TE_{01}$  and  $TM_{01}$  modes reach cut-off, where cut-off is defined as, [23, 24]

$$V = k_0 a \sqrt{(n_1^2 - n_2^2)} = 2.4 \quad (2.1)$$



where  $k_0 = 2\pi/\lambda$  is the vacuum wavenumber,  $n_1$  the refractive index of the core,  $n_2$  the refractive index of the cladding and  $a$  is the core radius. How LP modes are composed of fundamental modes is further illustrated in Figure 2.3 where a typical fibre with a 20  $\mu\text{m}$  core diameter and a step in refractive index between core and cladding of 0.001 was simulated using Optiwave Optifiber simulation software. The normalised propagation constant  $b$  is plotted as a function of normalised frequency (or  $V$  parameter) where  $b = \frac{\beta}{k_0} - n_2$  and  $\frac{\beta}{k_0}$  is the effective index,  $\bar{n}$ , where  $\beta$  is the propagation constant and will be discussed in Section 2.2.2. Above single mode operation ( $V > 2.4$ ) the fibre supports a total of seven fundamental modes. Figure 2.3 clearly shows that several fundamental modes have identical propagation constants (in the figure the modes are grouped by colour) that correspond to four LP modes.

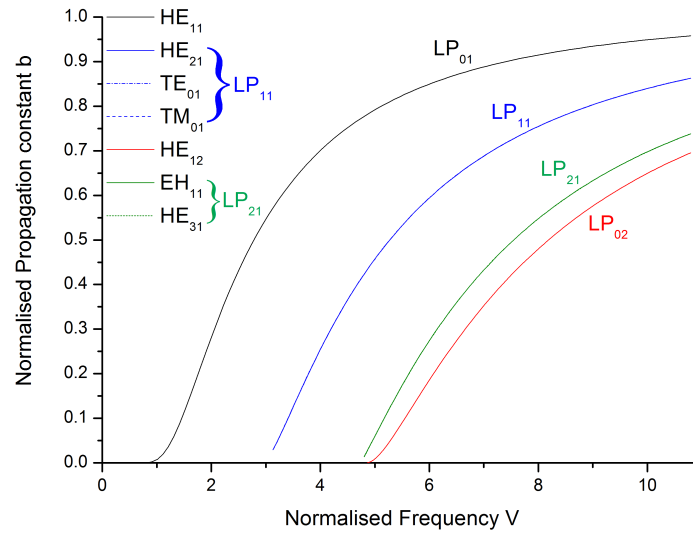


Figure 2.3: Normalised propagation constant as a function of normalised frequency for a few-mode fibre. Colours correspond to modes with near identical propagation constants that form LP modes as labelled

### 2.1.2 Band Gap Fibre

The properties governing the guidance in hollow core photonic band-gap fibre (HC-PBGF) can be thought of as being similar to SMF. The basic guidance mechanisms are discussed here briefly, but the linear and nonlinear impairments are beyond the scope of this thesis.

HC-PBGF's have the unique characteristics of guiding light in the core of a fibre with a lower refractive index than the cladding. Thus the light is not guided by traditional total internal reflection (as is the case for standard SMF, where it is confined to the core due to Snell's law), instead the light is kept to the core by the presence of an

optical band gap in the cladding interface. From an engineering point of view this can be thought of as total internal reflection through Bragg reflection where the micro-structure of the fibre cladding acts as a cylindrical Bragg reflector, where the cladding can be engineered to reflect a broad range of wavelengths and thus keep light in the core.

For PBGF the band-gap is placed in the fibre cladding along the length of the fibre. This allows the light to be reflected back into the core of the fibre even if the core has a lower refractive index than the cladding, such as an air or vacuum core. This leads to exciting possibilities in high-power and low-latency applications [25].

The basic HC-PBGF design is shown in Figure 2.4 where the air core is surrounded by a micro-structure cladding structure and was first demonstrated by Knight et al. [26]. Hollow core fibre has a theoretically lower loss than standard SMF, where silica fibre is limited by Rayleigh scattering. However, due to the complexity in fabricating a complex and uniform micro-structure, this theoretical low-loss has not been achieved to date. The band-gap is controlled by adjusting the diameter of the air holes and spacing between them (the pitch) [27]. The nodal points between air holes should also be kept thin to reduce scattering. Another source of loss is the air to glass interface, by controlling the shape of the core and maintaining it uniform along its length this loss can be reduced. Though the fibre itself is drawn in a similar manner to SMF the topic of micro-structured fibre fabrication is covered in much greater detail in [28].

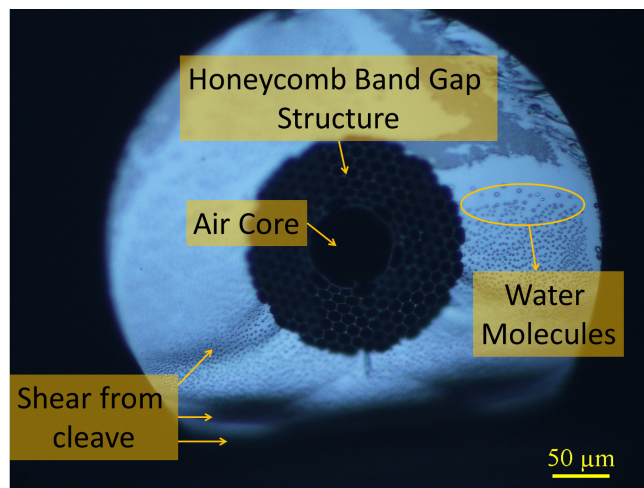


Figure 2.4: Cross section of a HC-PBGF. Labels indicate areas of interest.

## 2.2 Linear Fibre Impairments

### 2.2.1 Fibre attenuation

Attenuation, sometimes referred to as linear fibre loss, is one of the main parameters that define performance of an optical fibre. Engineering low-loss fibre has been one of the main achievements that has enabled optical communications on a global scale (and it's also worthy of a Nobel Prize [29]). Attenuation, as the name suggests, is the depletion of optical power through a length of fibre as measured by the receiver. A typical expression for power at a given point,  $L$ , along the fibre is expressed as,

$$\frac{dI}{dL} = -\alpha I(L) \quad (2.2)$$

Where  $I$  is the intensity of the optical signal and  $\alpha$  is the loss parameter which is the summation of several loss mechanisms.

**Intrinsic absorption:** is one of the fundamental sources of loss in a fibre. This is due to the material structure of the silicate glass causing light to interact with the material. The limits due to intrinsic absorption are highlighted in Figure 2.5 where ultraviolet and infrared absorption contribute to loss in varying degrees as a function of wavelength. Here, the ultraviolet and infrared absorption lines were calculated based on the work of [30, 31] for a fibre with an  $\text{SiO}_2$  cladding and  $\text{GeO}_2$  doped silica core. In the case of ultraviolet absorption, this results from the photon energies being high enough to move electrons in the material to a higher conduction band with the photons being absorbed in the process. In the infrared, absorption occurs due to the interaction of photons with molecular vibrations [20]. Both infrared and ultraviolet absorption lines can be adjusted by altering the core and cladding material.

**Extrinsic absorption:** as the name suggests, extrinsic absorption is absorption as a result of impurities in the glass. This is a major contributor to loss and results from fibre fabrication techniques that introduce impurities in the form of metals and hydroxyl. Figure 2.5 shows a typical loss spectrum due to extrinsic absorptions (blue trace) based on the work of [30] and [33] showing absorption for two metals (Cu and Fe) while in practice several other metals commonly contribute to extrinsic absorption. Figure 2.5 also shows the absorption due to water, in the form of hydroxyl or  $\text{OH}^-$ , being present in the fibre. This leads to a water-peak at  $1.38 \mu\text{m}$  with overtones at shorter wavelengths. These impurities can be removed with advanced fabrication techniques such as vapour disposition and modern low loss fibres have successfully removed virtually all impurities along with radically reducing the water-peaks [34].

**Rayleigh scattering:** this form of scattering is a result of inhomogeneities being frozen into the lattice of the glass after cooling. The inhomogeneities are small in relation to the wavelength of the light and causes a variation in the refractive index along the

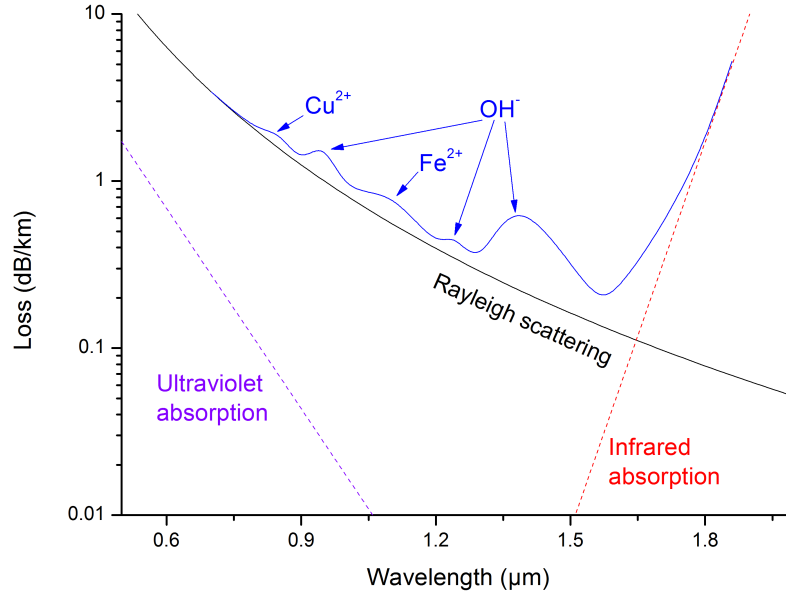


Figure 2.5: Basic loss spectrum of a typical SMF indicating the contribution of major loss mechanisms. Including intrinsic absorption (dotted lines), Rayleigh scattering (black line) and extrinsic absorption based on results in [20, 30, 31, 32]

length of the fibre. This causes a scattering in all directions and is expressed as the Rayleigh scattering coefficient [35]

$$\gamma_r = \frac{8\pi^3}{3\lambda^4} n^8 p^2 \beta_c K_b T_f \quad (2.3)$$

where  $\lambda$  is the optical wavelength,  $n$  the refractive index,  $p$  the average photoelastic coefficient,  $\beta_c$  the isothermal compressibility,  $K_b$  is Boltzmann's constant and  $T_f$  the fictive temperature. Figure 2.5 shows the calculated Rayleigh scattering loss (black trace) with typical values [20] for  $n = 1.46$ ,  $T_f = 1400$  K,  $\beta_c = 7 \times 10^{-11} \text{m}^2/\text{N}$  and  $p = 0.286$ . The loss in dB for a fibre of length  $L$  is thus expressed mathematically as,

$$(dB) = 10 \log_{10} (e^{\gamma_r L}) \quad (2.4)$$

Rayleigh scattering is the dominant loss mechanism in modern optical fibres and cannot be reduced with current fabrication techniques.

### 2.2.2 Dispersion

Dispersion and loss are the two major impairments of any optical communication channel operating under linear conditions (linear conditions being loosely defined as power concentrations before nonlinear effects become prevalent). Dispersion is the fre-

quency dependant change in the phase velocity of a wave. The most common manifestation being the distortion of optical pulses through temporal broadening due to the various frequency components of the pulse travelling at differing velocities. There are two major types of dispersion, intra-mode dispersion and inter-mode dispersion.

### 2.2.2.1 Intra-mode Dispersion

Intra-mode dispersion is by far the most common form of dispersion in optical fibre communications today, as it is prevalent in SMF. It is often referred to a chromatic dispersion. In optics it refers to how different frequencies travel at different velocities through an optical fibre, due to refractive index and material characteristics. Since an optical pulse has a finite spectral bandwidth different frequency components of the pulse will travel at different velocities leading to a broadening of the pulse in the temporal domain. This is mathematically given as the Taylor expansion series of the propagation constant with a centre frequency  $\omega_0$

$$\beta(\omega) = n_1(\omega) \frac{\omega}{c} = \beta + \beta'(\omega - \omega_0) + \beta'' \frac{(\omega - \omega_0)^2}{2} + \beta''' \frac{(\omega - \omega_0)^3}{6} + \dots \quad (2.5)$$

where  $\omega$  is the instantaneous angular frequency and prime represents the number of differentiations with respect to angular frequency [36]. Where the propagation constant  $\beta$  is defined as,

$$\beta = n_1 \frac{2\pi}{\lambda} = \frac{n_1 \omega}{c} \quad (2.6)$$

where  $n_1$  is the refractive index,  $\lambda$  the centre wavelength and  $c$  is the speed of light. The group delay can be expressed mathematically as,

$$\tau_g = \frac{1}{v_g} = \frac{d\beta}{d\omega} \quad (2.7)$$

where  $v_g$  is the group velocity which is the speed of a pulse envelope as it moves through a medium. The group delay ( $\tau_g$ ) is a commonly quoted fibre parameter and is measured in ps/km. Another commonly used parameter is the dispersion parameter  $D$  which is expressed as,

$$D = \frac{d\beta'}{d\lambda} = -\beta'' \frac{2\pi c}{\lambda^2} \quad (2.8)$$

and is measured in ps/nm km. A system is said to be in the normal regime for  $D < 0$  and in the anomalous regime for  $D > 0$ , with larger positive and negative values for dispersion leading to greater pulse spreading over a length of fibre. Equation 2.8 also shows a relation to  $\beta''$  which is the group velocity dispersion (GVD) and is given in units of ps<sup>2</sup>/km.

Finally, there is the effects of third order dispersion,  $\beta'''$ , which is simply the change is GVD as a function of the angular frequency. It is most commonly expressed in the

parameter called dispersion slope,  $s$ , given by

$$s = \frac{dD}{d\lambda} = \beta'' \frac{4\pi c}{\lambda^3} + \beta''' \left( \frac{2\pi c}{\lambda^2} \right)^2 \quad (2.9)$$

This is a useful parameter when designing fibres to support DWDM signals. Due to different frequencies travelling at different velocities this leads to pulse broadening and in extreme circumstances this can cause inter-symbol interference (ISI). By controlling the dispersion, through careful fibre design, it is possible to minimise ISI in WDM systems.

### 2.2.2.2 Inter-mode Dispersion

Though the thought of inter-mode dispersion seems like a discouraging limitation to multi-mode fibres it also applies to SMF. Under strict SMF conditions SMF only supports a single mode leading to intra-mode dispersion being the only contributor to fibre dispersion. However, SMF supports two degenerate modes with orthogonal polarisation ( $HE_{11}^x$  and  $HE_{11}^y$ ), thus making the fibre bimodal. Often inter-mode dispersion is referred to as mode dispersion or polarisation mode dispersion (PMD). Similarly to intra-mode dispersion its primary manifestation is in the temporal broadening of optical pulses propagating through the fibre causing ISI in severe circumstances. In an ideally circular symmetric SMF both polarisations would travel with equal velocities, however real-life fibres lack this ideal symmetry and thus have a birefringence.

Though the above discussion only studies the simple case of two modes (in this case the x- and y-polarisation) these inter-mode dispersion effects can be extended to include an even higher number of modes, as is the case in multi-mode fibre. The challenge to avoid inter-mode dispersion is to ensure the receiver is mode sensitive. A receiver incapable of separating each mode will receive the same optical pulse at different times leading to ISI. However, a receiver capable of separating each mode from each other would increase the total capacity of the fibre by increasing the number of usable optical paths. This has already been done in the case of polarisation modes, where each polarisation is separated in modulation formats such as DP-QPSK [37], leading to a doubling in capacity. A similar attempt to separate LP modes has also had considerable success and is currently a keenly researched topic [38, 39, 40]. For this, MIMO DSP is being used to separate temporally separated modes in a FMF.

## 2.3 Nonlinear Fibre Impairments

As optical fibre systems increase their span lengths and power density increases as a result of greater throughput, the risk of fibre nonlinearities affecting a system increases

considerably. Nonlinearity is yet another form of signal distortion that affects optical signals. One major source of fibre nonlinearities is stimulated inelastic scattering. This is due to energy being transferred directly into the material in the form of phonons. A second form of nonlinearity occurs due to the nonlinear interaction of the incident light with bound electrons of the material, this is often referred to as fibre nonlinearity. Both processes, along with the most common manifestation of their affects are discussed below.

### 2.3.1 Stimulated Inelastic Scattering

For stimulated inelastic scattering the light is absorbed, resulting in a nonlinear refractive index change, and then re-emitted at a down shifted frequency. Conservation of energy is maintained by the creation of a phonon, where phonons are material vibrations that are categorised as optical or acoustic. Two common forms of inelastic scattering are stimulated Raman scattering (SRS) and stimulated Brillouin scattering (SBS), both discussed here.

#### 2.3.1.1 Stimulated Raman Scattering

Stimulated Raman scattering (SRS) is a scattering that is induced due to molecular vibrations within the fibre. These lattice vibrations are characterised by phonons with significant energies being generated as a result of a small amount of an incident light being absorbed. These optical phonons are a result of neighbouring atoms in the lattice being displaced out of phase to one another and are generated at a frequency  $f_p$ . This results in a frequency down-shifted Stokes wave that propagates with the original signal. The coupled wave equations expressing the behaviour of the incident, or pump signal power  $P_p$ , Stokes seed power  $P_s$  are given as,

$$\frac{dP_p}{dz} = -g_{SRS}P_pP_s - \alpha P_p \quad (2.10)$$

$$\frac{dP_s}{dz} = g_{SRS}P_pP_s - \alpha P_s \quad (2.11)$$

in the stimulated regime for forward pumped SRS. SRS can also be backward pumped where the derivative in equation 2.11 would have a minus placed before it. For the coupled equations  $\alpha$  is the loss coefficient and  $g_{SRS}$  is the Raman gain coefficient given by [41]

$$g_{SRS} = \frac{3\omega_s}{\epsilon_0 c^2 n_p n_s} \frac{\Im[\chi_{iii}''' + \chi_{ijji}''']}{2A_{eff}^{ol}} P_p \quad (2.12)$$

where  $\omega_s$  is the Stokes frequency,  $\epsilon_0$  is the permittivity of free space,  $c$  the speed of light,  $n_p$  and  $n_s$  the occupation number of the pump and scattered photons respectively,  $A_{eff}^{ol}$  the effective area overlap of the pump and Stokes signal.  $\chi_{iii}^3$  and  $\chi_{ijji}^3$

represent non-zero elements of the fourth rank tensor where  $\chi_{iiii}^3$  is responsible for the Raman interaction of co-polarised pump and Stokes signals and  $\chi_{ijji}^3$  is responsible for orthogonally polarised signals.

The creation of a Stokes wave can be detrimental in WDM systems if the Stokes wave falls within the spectrum of frequencies being used. A typical Stokes wave will have its maximum gain  $\approx 13$  THz at a down-shifted frequency. Even if the Stokes wave does not coincide with another WDM channel it can still have a detrimental effect on the system, with undesirable effects such as pump depletion. This can be avoided by keeping the power density in the fibre below a certain threshold power, estimated to be [23]

$$P_{th} \approx \frac{16A_{eff}^{\omega}}{g_{SRS}L_{eff}} \quad (2.13)$$

where  $L_{eff}$  is the effective length of the fibre where  $L_{eff} = 1 - \exp^{-\alpha L} / \alpha$ .

### 2.3.1.2 Stimulated Brillouin Scattering:

Stimulated Brillouin scattering (SBS) is similar to SRS but it differs in that the phonons excited are acoustic in nature. SBS also propagates primarily in the backward direction. The acoustic phonons generate a back-propagating (backward in comparison to the pump power signal) acoustic wave that acts as a Bragg grating travelling through the length of the fibre, which in turn diffracts a portion of the pump signal to a down-shifted frequency (typically  $\approx 11$  GHz in standard SMF). The equations that express the proportion of input signal power  $P_0$  and Stokes seed power  $P_S$  are given as,

$$\frac{dP_0}{dz} = -\gamma_{SBS}\mathcal{L}(\nu)P_0P_S - \alpha P_0 \quad (2.14)$$

$$\frac{dP_S}{dz} = -\gamma_{SBS}\mathcal{L}(\nu)P_0P_S - \alpha P_S \quad (2.15)$$

where the peak SBS efficiency is expressed as, [42]

$$\gamma_{SBS} = \frac{g_m}{A_m^{ao}} \quad (2.16)$$

and  $\alpha$  is the loss coefficient.  $A_m^{ao}$  is the effective area of the  $m^{th}$  acousto-optic mode and  $\mathcal{L}(\nu)$  is the Lorentzian profile of the Brillouin gain as a function of frequency.  $g_m$  refers to the Brillouin gain of the  $m^{th}$  mode expressed as,

$$g_m = \frac{4\pi n^8 p_{12}^2}{c\lambda^3 \rho_0 \nu_m w_m} \quad (2.17)$$

where  $n$  is the refractive index,  $p_{12}$  is a component of the electrostriction tensor,  $c$  the speed of light,  $\lambda$  the pump wavelength,  $\rho_0$  is the mean of the material density,  $\nu_m$  the frequency shift and  $w_m$  the FWHM of the  $m^{th}$  line of the peak Brillouin gain spectrum



$(g_B)$ .

The effects of of SBS are most pronounced for CW pump sources. SBS can be detrimental is slow speed signals but this can be avoided by phase modulation of the signal [43, 44]

### 2.3.2 Optical Fibre Nonlinearity

Optical fibre nonlinearity refers to the relationship of the refractive index to the square of the electric field. For high optical intensities this leads to several effects that are termed nonlinear due to the squared relationship between the electric field and the refractive index change [23, 45, 46]. The relationship between the polarisation vector  $\mathbf{P}$  and the electric field  $\mathbf{E}$  is expressed as,

$$\mathbf{P} = \epsilon_0 (\chi' : \mathbf{E} + \chi'' : \mathbf{E}\mathbf{E} + \chi''' : \mathbf{E}\mathbf{E}\mathbf{E} + \dots) \quad (2.18)$$

where  $\epsilon_0$  is the permeability of free-space and  $\chi$  refers to the electrical susceptibility and  $:$  represents the salar product function between electrical susceptibility and electric field,  $\mathbf{E}$ . Here,  $\chi'$  refers to the linear susceptibility where its real and imaginary parts are responsible for the linear refractive index,  $n$ , and fibre loss coefficient,  $\alpha$ , expressed as,

$$n_0 = 1 + \frac{1}{2}\Re[\chi'] \quad (2.19)$$

$$\alpha = \frac{\omega}{c}\Im[\chi'] \quad (2.20)$$

In a centro-symmetric dielectric such as optical fibre all elements of  $\chi''$  are zero and thus  $\chi''$  effects are neglected for consideration. The main source of nonlinear refractive index changes and nonlinear loss are related to the real and imaginary parts, respectively, of the  $\chi'''$  term, as discussed previously for Raman where the imaginary part of  $\chi'''$  was used in Equation 2.12 to calculate the Raman gain. In a similar manner the nonlinear refractive index, or Kerr coefficient,  $n_2$  (not to be confused with the refractive index of the cladding) is expressed mathematically as the real part of the  $\chi'''$  electric susceptibility term where

$$n_2 = \frac{3\chi'''}{4\epsilon_0 cn_0^2} \quad (2.21)$$

where the Kerr coefficient has a typical value of  $2.6 \times 10^{-20} \text{ m}^2/\text{W}$  for standard SMF [23] and is related to the total refractive index such that

$$n = n_0 + n_2 I \quad (2.22)$$

where  $I$  refers to the light intensity ( $I = |\mathbf{E}|^2$ ). From here it is possible to define another useful non-linearity coefficient (as will become apparent in the next section),  $\gamma$ , expressed as [36, 47]

$$\gamma = \frac{n_2 \omega_0}{c A_{eff}} = \frac{3 \omega_0 \chi'''}{4 \epsilon_0 c^2 A_{eff} n_0^2} \quad (2.23)$$

where  $A_{eff}$  is the effective area of the optical mode and  $\omega_0$  is the frequency of the optical signal. A typical value for  $\gamma$  is in the region of  $2.5 \text{ W}^{-1} \text{ km}^{-1}$  for standard SMF.

### 2.3.2.1 Self Phase Modulation

The fibre nonlinearity effect, discussed above, can cause severe distortions to optical signals propagating in a fibre. One of the most commonly discussed and easiest to understand nonlinear distortions is caused by self-phase modulation. The SPM effect is due to an induced phase change on the optical signal itself and is related to phase change only, as the refractive index changes are real and the total optical power is conserved [36, 47]. The maximum phase change can be expressed as the integral of signal power along the fibre length

$$\phi_{SPM} = \gamma \int_0^L P_0 dz = \gamma P_0 L_{eff} \quad (2.24)$$

where  $\gamma$ ,  $P_0$  and  $L_{eff}$  have been predefined as the non-linearity coefficient, optical power and effective length respectively. SPM can become prevalent when the peak optical intensity of a pulse has a substantially different phase ( $\sim \pi$ ) to the leading and trailing edge. This difference in phase across the intensity profile of the pulse results in a time varying instantaneous frequency (or chirp) expressed as,

$$\Delta\nu(t) = \frac{1}{2\pi} \frac{d}{dt} \phi(t) \quad (2.25)$$

Thus a time-varying phase creates a time-varying frequency and can lead to distortions and broadening of the frequency spectrum of a given optical pulse. In the time domain SPM has no direct influence over pulse distortions. However, SPM can alter how dispersion alters an optical pulse in the temporal domain, with the result being pulse broadening and splitting over long distances of fibre.

### 2.3.2.2 Cross Phase Modulation

In a similar way to SPM cross phase modulation (XPM) also causes distortions in the frequency domain of an optical pulse. This is caused by interaction between two co-polarised signals. The intensity of one signal modulates the refractive index of the fibre for the second signal, this then causes phase modulation in the second signal. For a system with two signals ( $a$ ) and ( $b$ ), with respective powers  $P_0^{(a)}$  and  $P_0^{(b)}$ , the

phase change of the first signal,  $\phi^{(a)}$ , is expressed as,

$$\phi_{XPM}^{(a)} = 2\gamma \int_0^L P_0^{(b)} \left( \frac{z}{\Delta\nu_g} \right) dz = \gamma L_{eff} (P_0^{(a)} + 2P_0^{(b)}) \quad (2.26)$$

where  $P_0^{(b)}$  refers to the power of the adjacent signal and  $\Delta\nu_g$  is used to express the frequency matched offset between the two signals. When the two co-propagating signals are strongly velocity matched XPM effects will dominate over SPM. This is detrimental in DWDM systems where the spectral broadening can cause crosstalk between channels but can be mitigated by placing adjacent frequency channels on orthogonal polarisations in order to decrease the velocity matching [23, 48, 49].

### 2.3.2.3 Four Wave Mixing

At this point we have covered some of the major impairments in optical fibres. The final effect due to fibre nonlinearity discussed here is four wave mixing (FWM). All the impairments covered in this chapter can be summarised in the nonlinear Schrödinger equation that describes small perturbations through a fibre, assuming an adiabatic evolution, and is expressed in Equation 2.27

$$\frac{\delta E}{\delta z} = \underbrace{-\frac{\alpha}{2}E}_{\text{loss}} - \underbrace{\frac{i\beta''}{2} \frac{\delta^2 E}{\delta t^2}}_{\text{Dispersion}} + \underbrace{i\gamma E|E|^2}_{\chi''' \text{ nonlinearities}} \quad (2.27)$$

where FWM is an effect that occurs in a similar manner to SPM and XPM when a high optical intensity of one channel induces a refractive index change that causes a phase modulation. This is related to the  $\chi'''$  parameter through Equation 2.18, expressed here as

$$\mathbf{P}_{NL} = \epsilon_0 \chi''' : \mathbf{EEE} \quad (2.28)$$

where  $\mathbf{P}_{NL}$  is referred to as the induced nonlinear phase shift [47]. When this phase modulation occurs between multiple channels it creates new frequencies at side-band positions to the phase modulated signal, the creation of these new frequencies is known as four wave mixing. Take an example of four waves on a single polarisation with frequencies  $\omega_{1 \rightarrow 4}$ . The total electric field can be expressed as

$$\mathbf{E} = \frac{1}{2} \hat{e} \sum_{j=1}^4 E_j \exp [i(\beta_j z - \omega_j t)] \quad (2.29)$$

where  $\hat{e}$  is the polarisation vector and  $\beta_j$  is the propagation constant for each frequency  $\omega_{1 \rightarrow 4}$ . Substituting  $\mathbf{E}$  for  $\mathbf{P}_{NL}$  in Equation 2.28 and solving for  $E_{j=4}$  we get [47]

$$E_4 = \frac{3\epsilon_0}{4} \chi_{xxxx}''' \left[ \underbrace{|E_4|^2 E_4}_{SPM} + \underbrace{2(|E_1|^2 + |E_2|^2 + |E_3|^2) E_4}_{XPM} + \underbrace{2E_1 E_2 E_3 \exp(i\theta_+) + 2E_1 E_2 E_3 \exp(i\theta_-)}_{FWM} + \dots \right] \quad (2.30)$$

where  $\theta_+$  and  $\theta_-$  are expressed as

$$\theta_+ = (\beta_1 + \beta_2 + \beta_3 - \beta_4)z - (\omega_1 + \omega_2 + \omega_3 - \omega_4) \quad (2.31)$$

$$\theta_- = (\beta_1 + \beta_2 - \beta_3 - \beta_4)z - (\omega_1 + \omega_2 - \omega_3 - \omega_4) \quad (2.32)$$

The first and second terms in Equation 2.30 containing  $E_4$  represent SPM and XPM respectively with the remaining terms resulting from frequency combinations of all four signals resulting in an effect commonly referred to as four-wave mixing. This FWM signal is relatively weak but can accumulate over long transmission distances due to phase matching between channels, where the phase matching condition is satisfied in Equation 2.32 when all beta terms cancel to give  $\delta\beta = 0$ . This phase matching condition is often expressed for a SMF as,

$$\frac{2\pi\Delta\nu^2 D \lambda_c^2 L}{c} \ll 1 \quad (2.33)$$

where  $\Delta\nu$  is the frequency spacing between signals,  $D$  is the dispersion,  $\lambda_c$  is centre wavelength and  $L$  the fibre length. A classic example of where the new side-band frequency is created,  $\omega_4$ , is expressed by [20, 47]

$$\omega_4 = \omega_1 + \omega_2 - \omega_3 \quad (2.34)$$

and express the conservation of energy. This is for a discrete case where the effect of FWM can be integrated along the length of the fibre. In WDM systems this requires the contributions of all frequencies to be summed to get a total impact of FWM and this has been the standard approach for estimating FWM effects [47][50]. More recently the FWM equations have been solved by integrating along the length of the fibre and integrating across all frequencies [51, 52], to give a more accurate measure of FWM impact on WDM systems. It is useful to be able to quantify such effects accurately as the creation of these new frequencies can be a hindrance in WDM systems. In Chapter 4 of this thesis we seek to apply the new solution to few mode fibres in order to calculate capacity limits for few mode fibre systems.

More recently FWM has been used as a beneficial technique to achieve wave conversion and other useful applications due to the phase relationship between the original

signals and the newly created side-bands [53, 54, 18].

## 2.4 Modulation Formats

Modulation formats are the standard format for the process of encoding information onto an electromagnetic wave. A wave carries information by having an encoded signal modulated onto a carrier wave. This process is known as modulation. There are several different forms of modulation, some of which are discussed here. In optical communications, the process of placing an encoded signal onto a carrier wave is done by a device called a modulator.

### 2.4.1 Modulators

There are several types of optical modulators available as commercial devices. All modulators aim to control different dimensions of the optical signal independently. The dimensions in question generally refer to amplitude, phase, frequency and polarisation or the optical carrier wave and is expressed as the electric field  $\mathbf{E}(t)$  where

$$\mathbf{E}(t) = \hat{e}\Re[a \exp(i\phi - i\omega_0 t)] \quad (2.35)$$

and  $\hat{e}$  refers to the polarisation unit vector,  $a$  the amplitude,  $\phi$  the phase and  $\omega_0$  the frequency. The dimensional representation of modulation formats is readdressed in Chapter 3 where additional degrees of freedom are discussed.

Some modulators will only modulate certain dimensions, such as intensity modulators that aim to control only the amplitude of the carrier signal. In optics the two main forms of modulators are electro-absorption modulators and electro-optic modulators. Different modulator structures exist within each class. Depending on the target design characteristics of a given optical system there could be several trade-offs in selecting the optimum modulator.

**Electro-Optic Modulators:** Are a class of optical modulators that operate by exploiting the Pockels effect. The Pockels effect is similar to the Kerr effect that draws a relation between the refractive index of the medium and an applied electric field, through relations with  $\chi''$  and  $\chi'''$  susceptibility tensors. The Pockels effect exhibits a linear relation between birefringence and an applied electric field while the Kerr effect has a quadratic relation. This effect is present in non-centrosymmetric materials such as  $\text{LiNbO}_3$  and  $\text{InP}$ . This allows for the phase of the light propagating through the medium to be altered in phase by applying a voltage across the material. This phase

change is given by the relation [48, 55]

$$\phi(t) = \phi_0 - \pi \frac{\tau n^3 V(t) L}{\lambda d} \quad (2.36)$$

where  $\phi_0$  is the initial phase,  $\tau$  the Pockel coefficient,  $n$  the refractive index,  $V(t)$  the voltage applied across the material,  $\lambda$  the centre wavelength of the incident light where  $L$  and  $d$  refer to the length and depth of the material being used. More commonly [23], this is simplified to represent the metric known as  $V_\pi$

$$\phi(t) = \phi_0 - \pi \frac{V(t)}{V_\pi} \quad (2.37)$$

where  $V_\pi$  refers to the voltage required to induce a  $\pi$  phase shift on the light propagating through the modulator.

Materials such as  $\text{LiNbO}_3$  are now widely used for phase modulation, where they exhibit low insertion loss and high operating bandwidths. However, due to the material structure there is a strong birefringence dependency. This has not stopped the development of EOM structures that can modulate both phase and amplitude.

**Mach-Zehnder Interferometer:** In order to create EOMs that are capable of modulating the intensity of light an interferometric technique, known as the Mach-Zehnder interferometer is used. Modulators that use such a technique are called Mach-Zehnder modulators (MZM) and are one of the most common optical modulators. The basic structure is shown in Figure 2.6 (a) where the power is split in a ratio between the upper and lower arm, where ideally the power in both arms is equal. They work using the voltage dependence described in Equation 2.37, inducing a phase change as a function of applied voltage in each arm of the interferometer.

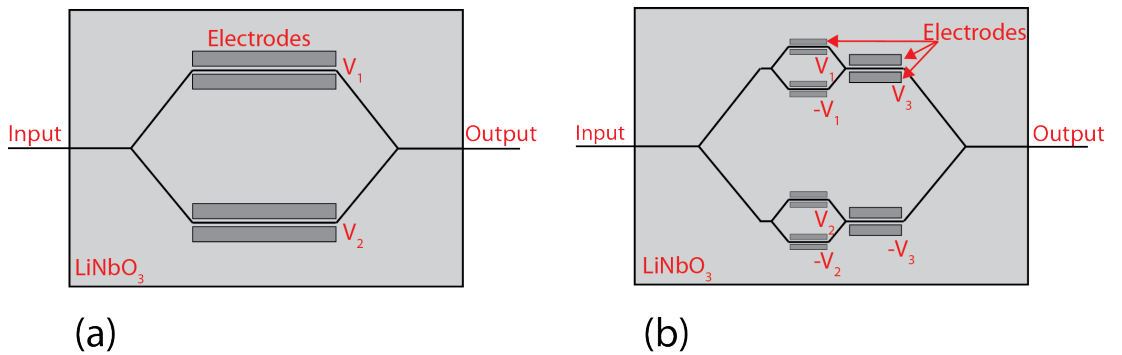


Figure 2.6: Plan view of (a) Mach-Zehnder modulator structure and (b) Nested Mach-Zehnder modulator.

The ratio of the output signal power with respect to the input signal is given as [48],

$$\frac{E_{out}(t)}{E_{in}(t)} = \frac{1}{2} \left[ \exp\left(\frac{i\pi V_1(t)}{V_\pi}\right) + \exp\left(\frac{i\pi V_2(t)}{V_\pi}\right) \right] \quad (2.38)$$

$$= \underbrace{\cos\left(\frac{\pi V_1(t) - \pi V_2(t)}{2V_\pi}\right)}_{\text{Amplitude Modulation}} \underbrace{\exp\left(\frac{i\pi V_1(t) + i\pi V_2(t)}{2V_\pi}\right)}_{\text{Phase Modulation}} \quad (2.39)$$

where  $V_1$  and  $V_2$  refer to the voltage applied across the electrodes on the upper and lower arm of the interferometer respectively. As can be seen from Equation 2.39 the modulator allows both the intensity and phase of the light to be modulated by adjusting the voltages applied to each arm. One way of simplifying the bias circuitry for amplitude modulation is to make  $V_1(t) = -V_2(t)$ . In practice it is incredibly difficult to match the length of each arm. To compensate for this a bias voltage is introduced,  $V_{bias}$ , onto one arm. The transform function of the modulator can thus be written as [23, 48]

$$T_{MZM} = \alpha_p \exp\left(\frac{i\pi V(t)}{V_\pi} + V_{bias}\right) + (1 - \alpha_p) \exp\left(\frac{i\pi V(t)}{V_\pi}\right) \quad (2.40)$$

where  $\alpha_p$  is the parameter given to the ratio of amplitude and phase modulation, expressed as [56]

$$\alpha_p = 2I \frac{\frac{d\phi}{dt}}{\frac{dI}{dt}} \quad (2.41)$$

where  $I$  represents the instantaneous intensity ( $I = |E|^2$ ) and  $\phi$  the phase. For an ideal Mach-Zehnder the chirp will be zero ( $\frac{d\phi}{dt} = 0$ ) and thus the  $\alpha_p$  parameter in this ideal situation will be zero.

One draw-back of the Mach-Zehnder structure is that intensity and phase cannot be modulated independently. This can be achieved by nesting three Mach-Zehnder interferometers in a single sample of LiNbO<sub>3</sub> as seen in Figure 2.6 (b). By selecting voltages in a particular way the modulator can reach any point in the signal space (the signal space will be discussed in Section 2.5). In this thesis a nested MZM was used to modulate a signal in a format known as quadrature phase-shift keying (QPSK is discussed further in Chapter 3). This was achieved using the nested MZM in the so-called push-pull regime where voltage  $V_1$  and  $-V_1$  in Figure 2.6 (b) are selected to achieve a phase modulation known as differential phase-shift keying (DPSK), this is repeated for the nested interferometer on the lower arm ( $V_2$  and  $-V_2$  in Figure 2.6 (b)). The information is encoded onto these two modulators and are mutually exclusive. To avoid interference in the signal space the third interferometer is used to keep a  $\pi/2$  phase change between the interferometers on each arm. The output of the modulator has four phase states,  $\pi/4$ ,  $3\pi/4$ ,  $5\pi/4$  and  $7\pi/4$ , each corresponding to a symbol point.

With the set of modulators discussed above it is possible to begin modulating an optical signal. The modulation format dictates in what way the electrical signals modulate

the optical signal. The two most common modulation formats in optical communications, and the formats used in this thesis, are intensity and phase modulation.

### 2.4.2 Intensity Modulation

Intensity modulation is one of the most basic forms of modulation. By modulating the amplitude of the carrier signal it is possible to encode a message onto the carrier. In binary encoding systems, as used for digital modulation, the information is represented as ones and zeros corresponding to when the light is on and off. This modulation format is referred to as on-off-keying (OOK) and is one of the most common modulation formats.

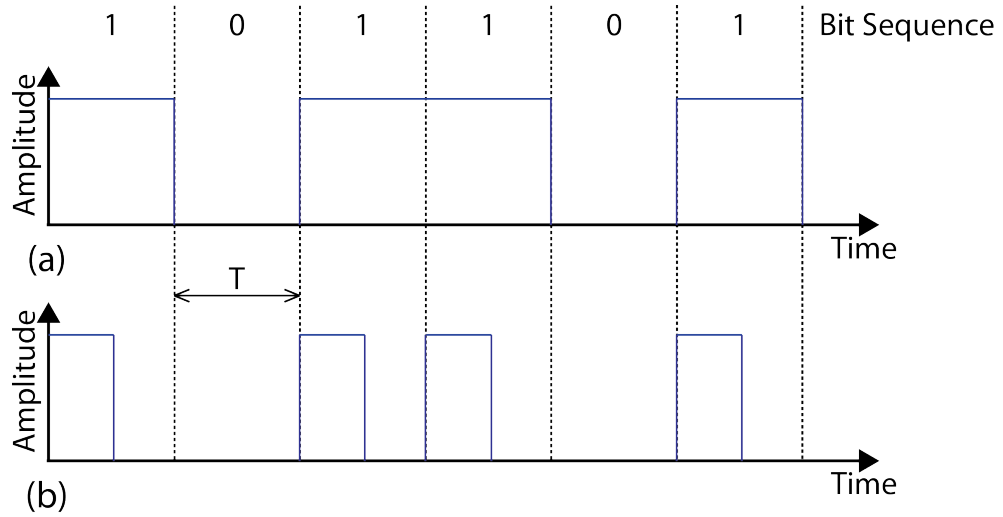


Figure 2.7: Bit sequence encoded in (a) non-return-to-zero and (b) 50% return-to-zero where the amplitude returns to zero for 50% of the bit period,  $T$

The two main ways of encoding using OOK are using a signalling systems know as non-return to zero (NRZ) and return-to-zero (RZ). For NRZ the amplitude of the signal remains high for the entire bit period  $T$ . The amplitude only changes when the encoded signal changes state from one to zero. For RZ signalling the amplitude returns to zero during each bit period. An illustration of the difference between NRZ and RZ can be seen in Figure 2.7. There are three popular duty cycles for RZ signalling, all of which are some duty cycle between zero and  $< 100\%$  of the bit period. The most common are duty cycles of 50%, as shown in Figure 2.7 can be achieved by biasing an MZM at quadrature and driving it with a sinusoidal voltage ( $f = 1/T$ ) between  $\pm V_\pi/2$  (it is also possible to implement intensity modulation using an EAM [57]). In this configuration RZ will use approximately double the bandwidth of a system encoded using NRZ, where the modulator will produce a smooth pulse as opposed to the perfect rectangular pulse illustrated in Figure 2.7. The RZ implementation will use double the bandwidth, as the RZ signal will tend towards a 25% duty cycle compared to an NRZ 50% duty cycle signal. Both formats can be represented in the frequency



domain by a sinc function with NRZ requiring only half the bandwidth compared to RZ, as the bandwidth occupied is related purely to pulse duration. Two other configurations are using duty cycles of 33% and 67% by biasing a MZM at peak and null respectively and driving it with  $\pm V_\pi$ . For 67% RZ the modulator is driven through the null of its transfer function causing a  $\pi$  phase change between neighbouring bits and suppressing the carrier, thus this format is sometimes referred to as carrier suppressed return-to-zero (CS-RZ).

More advanced forms of intensity modulation can be used to encode more complicated symbols. Such as a two bit symbol. To convey a two bit symbol code, the system requires four distinct symbols. This can be done using a format known as four-level amplitude shift keying (4ASK). This is done by having four distinct amplitude levels, each level corresponding to a two bit symbol.

### 2.4.3 Phase Modulation

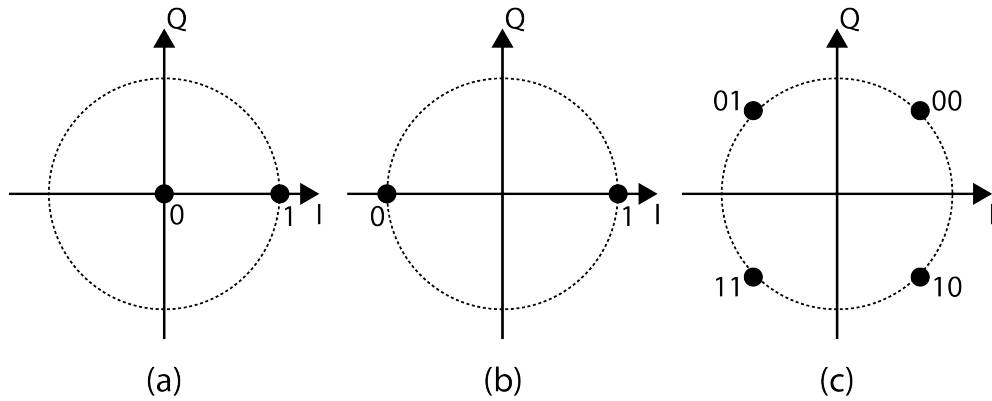


Figure 2.8: Constellation diagrams showing (a) OOK, (b) 2 Phase shift keying and (c) QPSK. The dotted circles represent a region of constant amplitude.

Another signal dimension that is often exploited in optical communications is phase, where a phase shift of the optical carrier is used to represent digitally encoded data. Similar to ASK, there are several forms of phase shift keying (PSK). One of the most commonly used, midway through the last decade, was differential binary phase shift keying (DPSK). This offered the prospect of having a 3dB improvement in optical signal to noise ratio (OSNR) over OOK. Differential phase shift keying can be achieved in several ways [58, 59], one of which uses a MZM biased at null and driven by  $2V_\pi$ . Similar to SC-RZ, by driving the modulator through the null of the transfer function a  $\pi$  phase shift is induced, this creates two distinct symbol points as can be seen on the constellation diagram of Figure 2.8(b). However, by biasing at null it also introduces a drop in amplitude when changing state, this causes a slight amplitude modulation when using a MZM to generate DPSK. This can be eliminated by using a phase modulator at the expense of increased chirp, as an instantaneous phase change is unattain-

able [58]. The format gets its name from the way it is detected by measuring the difference in phase between each successive bit at the receiver. For detection of ASK formats a standard photo-detector converts the optical power into an electrical signal, however photo-detectors do not detect phase directly. In the absence of a coherent receiver a delay interferometer can be used to create constructive and destructive interference to recover the bit sequence (homodyne detection also referred to as differential detection). This can be done by setting the delay interferometer to have a 1-bit delay. This causes the signal to interfere with itself in a constructive or destructive manner leading to the existence or absence of optical power at the output ports of the interferometer, termed the constructive and destructive ports. This differential measurement between successive bits allows for phase changes between bits to be detected with standard direct detection. This can be done on either the constructive or destructive port or by using a balanced receiver where both ports are detected. Alternatively a heterodyne detection technique can be used where a local oscillator at the receiver can be used to recover the phase. Such a technique is referred to as coherent detection and has allowed for a far greater utilisation of the signal space for modulation formats utilising phase modulation.

A resurgent interest in coherent receiver technology has brought with it the widespread use of the phase domain as a region for encoding data. A more advanced form of phase modulation uses four phase states,  $\pi/4$ ,  $3\pi/4$ ,  $5\pi/4$  and  $7\pi/4$ , utilising the in-phase and quadrature dimensions of the carrier signal. This modulation format is known as QPSK and can be generated using a nested MZM as described in Section 2.4.1. The constellation diagram of QPSK is shown in Figure 2.8(c) where the four phase states correspond to symbols that can be mapped using two bits of digital information, thus QPSK has double the spectral efficiency of DPSK or OOK. QPSK can be detected in a similar manner to DPSK using a delay interferometer [60] or, more commonly in current research, using coherent detection where the phase information is fully recovered using heterodyne detection and digital signal processing.

Spectral efficiency is one of the primary metrics that describe how efficient an optical system is and usually corresponds to systems with greater overall capacity. Spectral efficiency relates to the maximum amount of digital information that is conveyed in a certain time interval for a finite bandwidth and is measured in units of bits/s/Hz/pol as will be discussed in greater detail in Chapter 3. Some ways of improving the spectral capacity even further is to increase the number of symbols in the constellation space, as is done using quadrature amplitude modulation (QAM) formats that utilise both amplitude and phase modulation. These techniques require coherent detection to recover in-phase and quadrature information where the digital data is recovered using digital signal processing. Though a vibrant topic for research, this thesis does not go into any depth on the algorithms involved with such processing.

Another technique to increase the amount of information transferred through a fibre is to multiplex two independently modulated signals onto each polarisation. This has been done using a QPSK signal and is called dual polarisation QPSK (DP-QPSK) or polarisation multiplexed QPSK (PM-QPSK), this format has been used as a comparative format in Chapter 3 of this thesis. More recently modulation formats utilising polarisation as a way of directly encoding information has been proposed and Chapter 3 of this thesis examines the implementation of one such format.

## 2.5 Information Theory

The topic of information theory has become vast and multidisciplinary since its introduction by Shannon in 1948 [1]. As this thesis is related to optical communication the basics of Shannon's communication theory are of particular importance. Here, communication theory is briefly reviewed in the context of digital communications. The basic design of a communication system is presented in Figure 2.9.



Figure 2.9: Block diagram of a generic communication system

Every communication system consists of key parts such as a transmitter, channel of communication and receiver. In optical communications the source is typically a message that has been pre-encoded into the electrical domain. For most communications today the signal is represented as a digital message that is passed to the transmitter. The transmitter consists of a laser source which is encoded with the digital information in the transmitter (as discussed in Section 2.4). From here the signal is transferred over the optical fibre channel (discussed in Sections 2.1 to 2.3) and then decoded at the receiver using optical detectors and various detection techniques. The detection technique employed for decoding depends on how the source message was encoded (as mentioned in each case in Section 2.4). Though we are concerned with the transmission of optical signals in optical communications, fundamentally we are concerned with the information carried by these signals. Shannon, along with his contemporaries [61], developed a theory that provides useful insight into the relationship between the transmitted signals and the messages they are entrusted with carrying. This is simplified in the digital domain as the number of possible messages is reduced to binary

decisions, ones and zeros. Therefore, for a binary system the information content is a subset of all transmittable messages, expressed as,

$$I(x_i) = \log_2 \left[ \frac{1}{P(x_i)} \right] \quad (2.42)$$

where  $P(x_i)$  denotes the probability of a given message ( $i = \{0, 1\}$ ) occurring. Therefore the maximum amount of information that can be transmitted is the maximum amount of mutual information. This becomes complicated when noise is introduced into the system. To deal with this, Shannon proposed a term for the average ambiguity of a received signal, now commonly known as information entropy, such that the mutual information is expressed as,

$$I(x|y) = H(x) - H_y(x) \quad (2.43)$$

where entropy is defined as the average information produced at the source, expressed as,

$$H(x) = - \sum_{i=1}^m P(x_i) \log_2 [P(x_i)] \quad (2.44)$$

where several channel effects, such as noise, can contribute to  $P(x_i)$ . Once the basic expressions of information and entropy are understood it is possible to define the maximum capacity of the system in the presence of entropy.

### 2.5.1 Capacity Limits

Fundamentally, the aim of Shannon's work was to calculate the maximum amount of information that can be transferred, without error, given a finite bandwidth. For a discrete channel, with no noise, this can be expressed as,

$$C = \lim_{T \rightarrow \infty} \frac{\log N(T)}{T} \quad (2.45)$$

where  $N(T)$  is the number of allowed signals of duration  $T$ . With the introduction of additive white Gaussian noise the receiver is degraded by information entropy. This reduces the maximum achievable mutual information at the receiver (as  $I(x|y) = H(x) - H_y(x)$ ), where the capacity of a discrete signal is equal to the maximum achievable mutual information ( $C_s = \max I(x|y)$ ). For a binary system with additive white Gaussian noise the maximum mutual information is defined as [62]

$$C_s = \frac{1}{2} \log_2 \left( 1 + \frac{S}{N} \right) \quad (2.46)$$

where  $S$  and  $N$  represent the received signal and noise power respectively. Then for a given capacity where the minimum sample rate is limited to the Nyquist sampling

limit [61, 63] of twice the bandwidth,  $2B$ , the maximum capacity for a communication channel for a given bandwidth is expressed as,

$$C = B \log_2 \left( 1 + \frac{S}{N} \right) \quad (2.47)$$

and is often referred to as the Shannon capacity limit. However, for optical communications where optical fibre is used as the transmission channel the model for capacity breaks down when high powers are present in the fibre, for this there are lower bounding approximations for the capacity limits.

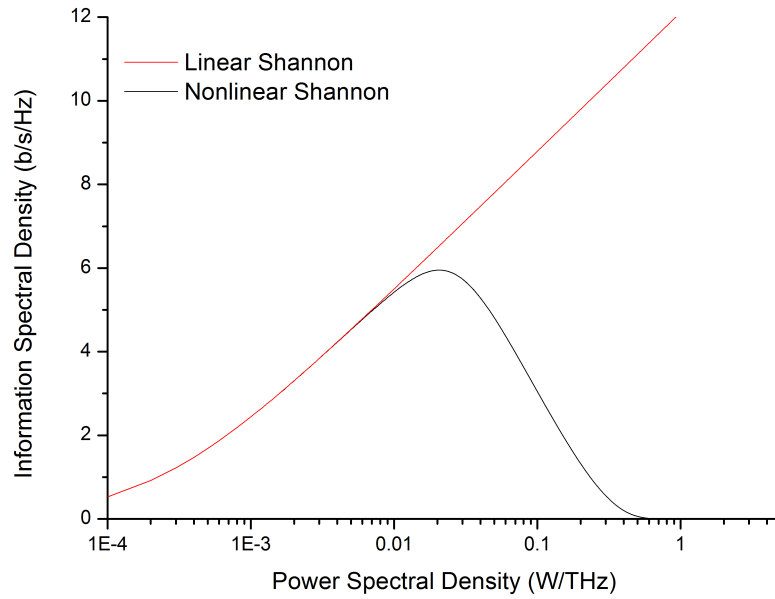


Figure 2.10: Linear and nonlinear Shannon limits shown in red and black traces respectively. The plot shows the relationship between information spectral density and power spectral density for a optical system with characteristics shown in Table 2.2.

**Nonlinear capacity limits:** For high densities of optical powers additional noise effects become dominant in optical fibres. This is due to fibre nonlinearities, as discussed in Section 2.3. These nonlinearities render the standard additive white Gaussian noise model somewhat inept when modelling capacity limits over a fibre channel. An alternative model that takes fibre nonlinearity into account was first proposed by Mitra and Stark [2], where they used the effects of cross phase modulation, XPM, as the dominant nonlinear contribution to noise. From here they derived a closed form analytical

expression for the lower bound of the nonlinear Schrödinger equation

$$\frac{C}{B_{NL}} = \log_2 \left( 1 + \frac{e^{-\left(\frac{P_s}{P_{NL}}\right)^2} P_s}{P_n + \left(1 - e^{-\left(\frac{P_s}{P_{NL}}\right)^2}\right) P_s} \right) \quad (2.48)$$

Where  $S$  in equation 2.47 is related to the numerator in Equation 2.48 where  $P_s$  is signal power. The denominator in Equation 2.48 is the summation of noise terms ( $N = P_n + \left(1 - e^{-\left(\frac{P_s}{P_{NL}}\right)^2}\right) P_s$ ), where the nonlinear noise  $P_{NL}$  is expressed as,

$$P_{NL} \approx \sqrt{\frac{\lambda^2 B D \Delta f}{c \gamma^2 L_{eff} 2 \ln\left(\frac{N_{ch}}{2}\right)}} \quad (2.49)$$

and  $P_n$  is the noise induced by the optical amplifiers

$$P_n = N_a(G - 1)n_{sp} \left(\frac{hc}{\lambda}\right) B \quad (2.50)$$

where  $\gamma = \frac{2\pi n_2}{A_{eff}\lambda}$ ,  $N_a$  is the number of discrete amplifiers and  $n_{sp}$  is the spontaneous emission noise factor related to the noise figure ( $n_{sp} = \frac{10^{\frac{NF}{10}}}{2}$ ). The remaining terms are defined in Table 2.2 where typical system parameters are used as an example for calculating the capacity limits of an optical system.

Table 2.2: Data used to seed nonlinear Shannon models

System Characteristics			
WDM Channel Spacing	$\Delta f$	50	GHz
Local Dispersion (ps/nm km)	$D$	20	ps/nm km
Nonlinear Index Coefficient	$n_2$	$27e - 21$	$m^2/W$
Effective Area	$A_{eff}$	100	$\mu m^2$
Centre Wavelength	$\lambda$	1550	nm
Length		2000	km
Fibre Loss	$\alpha$	0.2	dB/km
Amplifier Spacing		80	km
Amplifier Noise Figure		4.5	
Amplifier Gain	$G$	1000	
Number of WDM Channels	$N_{ch}$	100	
WDM Channel Bandwidth	$B$	50	GHz

The result of these closed form approximations allows for the calculation of lower bound capacity limits for various system configurations. Here, the system configurations in Table 2.2 were used to calculate the linear and nonlinear capacity limits of the system for increasing power spectral density. The result can be seen in Figure

2.10 where the linear Shannon limit (shown in red) is seen to have increasing information spectral density for increasing power spectral densities. However, this growth is limited in the nonlinear model (shown in black) where a clear peak of information spectral density as a function of power spectral density can be seen. Though, this is only a lower bound limit and does not take into account receiver memory or distributed detection, it is still a useful engineering heuristic that has become a regular tool in accessing optical systems [2, 3, 4, 64, 65, 66]. The work of Mitra and Stark investigated XPM as the dominant nonlinear contributor, nonlinear limits can also be derived in cases where four wave mixing is taken to be dominant [51]. This is the approach taken in Chapter 4 of this thesis where a closed form analytical model of FWM in FMF is compared to the XPM nonlinear model.

## 2.6 Chapter Summary

This chapter has introduced a wide range of topics that relate to the technical undertakings of the chapters to follow. Fundamentally, optical fibre propagation is limited by loss. Upon high incident optical powers the electric field interacts with the material of the medium resulting in nonlinear propagation and causing distortions to the signal, the cause and nature of some of these effect, such as self phase modulation and four-wave mixing were discussed. The introduction of nonlinearities has the potential to reduce the overall capacity of an optical communication link where Section 2.5.1 studied the fundamental limits to capacity and the lower bound limit in the presence of nonlinear effects.

The sections introducing the basics of optical fibre and how novel fibres can be used to guide light, in the case of FMF by total internal reflection and in the case of hollow core fibre by use of an optical band gap, will be of particular insight in Chapters 4 and 5 dealing with FMF and hollow core fibres respectively. While topics on modulation are used throughout the thesis, discussions on multidimensional modulation formats will be of particular use in Chapter 3. Finally, the topics of information theory and capacity limits were introduced in this chapter and will be put to use throughout the thesis.

## Chapter 3

# Power Efficient Modulation Formats

*"Between the phone calls and text messages the air must be thick with words"*

My first born for a song, Bell X1

Current trends in optical communication are concerned with broaching the omnipresent capacity limit of current optical systems. If, as outlined in Chapter 1, the current optical fibre infrastructure is used it remains an important task to clearly define the limits of a single strand of single-mode optical fibre. Systems and techniques must then be designed that provide the most spectrally efficient form of transmission over existing and future single mode fibre (SMF) links, leading to a convergence on capacity limits. This push for higher spectral efficiencies will continue to lower the cost per transmitted bit for optical transport. The majority of recent research has focused significant effort on multi-level, multi-dimensional modulation formats to achieve the ultimate capacity in a single fibre. All recent capacity records in SMF have been achieved using formats such as dual-polarisation quadrature phase-shift keying (DP-QPSK) and quadrature amplitude modulation (QAM). However, due to the increased optical signal to noise ratio (OSNR) requirements, the reach of these multi-level, multi-dimensional modulation formats is a concern. Thus, power efficient modulation formats, those having a low required signal-to-noise ratio per bit for a given bit-error-ratio, have also garnered attention recently [67, 68, 69] and are the subject of this chapter. More specifically this chapter is focused on four-dimensional optimized formats where the intensity and phase of both polarisations are taken to be four independent dimensions and is explained in detail in Section 3.1. From this viewpoint of dimensionality it is important to have a form of mental visualisation that will later aid the understanding of the polarisation-switched quadrature phase-shift keying (PS-QPSK) format and how to implement a successful digital signal processing (DSP) recovery algorithm, this is covered in Section 3.2. Power-efficient modulation formats are of fundamental importance in optical communications because they provide the ultimate sensitivity limit for the optical channel (see Section 3.3). They also have practical importance because they enable increased nonlinear tolerance, and



therefore the potential for ultra long-haul transmission, all of which are covered in Section 3.4, where PS-QPSK experimental results for back-to-back and  $10 \times 100\text{km}$  wavelength division multiplexing (WDM) transmission are presented.

### 3.1 Modulation Formats Dimensionality

The formula presented in 3.1 can be used as a general expression of an electromagnetic wave [23] where  $\hat{\mathbf{e}}$  is the polarisation unit vector,  $a$  amplitude,  $\phi$  phase and  $\omega_0$  denotes the carrier frequency at a given time  $t$ . This is more generally represented in phasor notation as  $A = ae^{i\phi}$  for translation onto constellation diagrams where the real and imaginary parts correspond to the in-phase and quadrature coordinates respectively.

$$\mathbf{E}(t) = \hat{\mathbf{e}}\Re[a \exp(i\phi - i\omega_0 t)] \quad (3.1)$$

As can be seen in Equation 3.1 the wave consists of both amplitude and phase (here only the real part is taken for simplicity). These two degrees of freedom are commonly used for the encoding of digital modulation formats such as PSK, ASK and QAM. When using an optical carrier the polarisation of the electromagnetic wave can be used as a third degree of freedom. All polarisation division multiplexed systems take advantage of this third degree of freedom. However, when studying polarisation in more detail (see Chapter 2), it becomes apparent that there are four degrees of freedom when polarisation is included. These are the absolute amplitude and phase of the electromagnetic wave in one polarisation, along with a further two degrees of freedom from the relative amplitude and phase of the wave in an orthogonal polarisation. This is commonly denoted in Jones space [70, 68, 71], where the electric field amplitude of the wave,  $\mathbf{E}$ , is given as

$$\mathbf{E} = \|\mathbf{E}\| \exp(i\phi_a) J = \|\mathbf{E}\| \exp(i\phi_a) \begin{pmatrix} \cos \theta \exp(i\phi_r) \\ \sin \theta \exp(-i\phi_r) \end{pmatrix} \quad (3.2)$$

where  $\phi_a$  and  $\phi_r$  denote the absolute and relative phase, respectively, between the  $x$  and  $y$  polarisations,  $J$  denotes the Jones vector,  $\theta = \sin^{-1}(|E_y|/\|\mathbf{E}\|)$  and  $\|\mathbf{E}\|^2 = |E_x|^2 + |E_y|^2$  where  $x$  and  $y$  denote the polarisation components.

The four dimensions become even more apparent when looking at Figure 3.1 where the four waves are illustrated propagating in a fibre where both the real and imaginary parts of the wave, shown in solid and dotted lines respectively, propagate in two distinct polarisation  $x$ - and  $y$ - shown in red and blue respectively. The amount of power given in one polarisation relative to the other is given by  $\sin(\theta)$  or  $\cos(\theta)$  where  $\theta$  can be thought of as the relative angle between each polarisation in a bimodal fibre. These

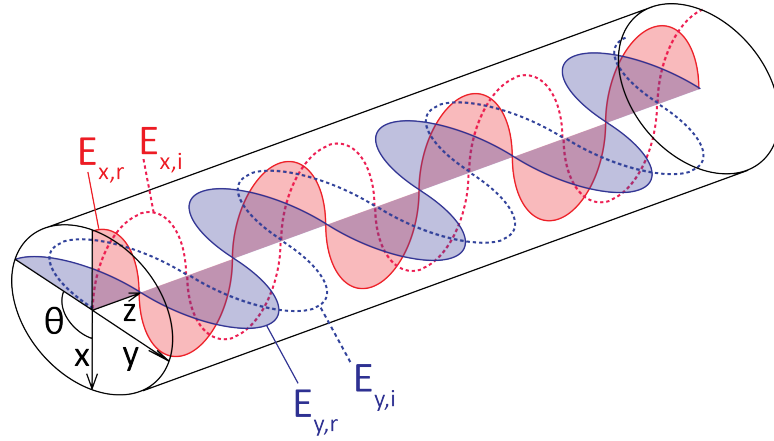


Figure 3.1: Illustration of real (solid line) and imaginary (dotted line) wave-functions propagating in the x- and y-polarisation, shown in red and blue respectively.

four degrees of freedom can then be expressed as a vector

$$\mathbf{s} = \begin{pmatrix} E_{x,r} \\ E_{x,i} \\ E_{y,r} \\ E_{y,i} \end{pmatrix} = \begin{pmatrix} ||\mathbf{E}|| \cos \phi_x \sin \theta \\ ||\mathbf{E}|| \sin \phi_x \sin \theta \\ ||\mathbf{E}|| \cos \phi_y \cos \theta \\ ||\mathbf{E}|| \sin \phi_y \cos \theta \end{pmatrix} \quad (3.3)$$

where  $E_{x,r}$  and  $E_{x,i}$  correspond to the real and imaginary part of the wave-vector in the x-polarisation and  $E_{y,r}$  and  $E_{y,i}$  represents the respective components in the y-polarisation where real components are given on the right hand side of Equation 3.3.

With Equations 3.2 and 3.3 and the knowledge that  $\phi$  must fall between the limits of  $-\pi$  to  $+\pi$  it is possible to calculate the number of allowable phase states for any given format that utilise the four degrees of freedom of an optical wave.

A logical progression in thought might ask, how many more degrees of freedom are possible when designing modulation formats? For example, it is well know that the frequency of the carrier wave can be modulated. Also, future systems may use an increased number of spatial modes, in which case, the spatial domain would represent a further degree of freedom. The reason these additional degrees of freedom have been neglected is owing to the following two reasons.

1. In the case of frequency being considered an additional degree of freedom Shannon's theory poses the problem

How much can a communications channel convey without error if given an available bandwidth with an average signal and noise power (in Watts)?

By this standard the available bandwidth is fixed and the challenge is to maximise transmission provided that the carrier remains fixed. This has been the heuristic that the modern ITU grid is based upon and as a result would make

any format that requires frequency modulation over a wide bandwidth infeasible.

2. The major drawback with considering the spatial domain as an additional degree of freedom is pertaining to the fact that space is not generally denoted as a factor in the composition of an optical wave. As will become clear in Section 3.3, in order for the spatial domain to be considered when deriving possible energy efficient modulation formats, the energy required to place the wave in one spatial domain or another (whether this be mechanical energy or otherwise) must be transmutable with existing notation for amplitude, phase and polarisation. This may be possible, though beyond the scope of this initial investigation.

## 3.2 Visualisation Methods

Now that it has been clearly established that a dual-polarisation optical system has four degrees of freedom, it becomes useful to visualise how modulation formats may look in this new four-dimensional signal space. There are well known visualisation techniques, such as constellation diagrams and the Poincaré sphere that aid our understanding. The constellation diagram is useful for understanding phase and amplitude information of symbol positions in modulation formats that use a single polarisation. The major drawback in this technique is that it fails to convey any information on the state of polarisation and therefore of the relative phase between x- and y-polarisations of a dual polarisation signal. The Poincaré sphere on the other hand does a very good job of conveying the state of polarisation but it does not convey any phase information. Here, stereographic projection is used to give illustrative representations of four-dimensional formats that show all states of phase for any given modulation format. Stereographic projections are sometimes found in photography but are used here to project four dimensional objects onto a two-dimensional surface (in this case a sheet of paper or computer monitor). Commonly used two dimensional projections of three-dimensional objects, such as isometric and perspective projection, can be used effectively to convey information of three dimensional spaces. Stereographic projection is similar to other three-dimensional projection techniques with the major difference being that the points are projected onto an imaginary spherical boundary<sup>1</sup>. As the variable range of phases varies between  $-\pi$  and  $\pi$  using a spherical signal space seems like the logical choice for visual representation. Moving from three dimensions to four dimensions the process of stereographic projection is simply repeated by adding a second spherical boundary outside the first, similar to a bubble inside a bubble. The following sections (Sections 3.2.1 to 3.2.3) study examples, using stereographic projection, to represent four-dimensional signals and how the visualisation method

<sup>1</sup>For more information visit <http://www.math.cmu.edu/~fho/jenn/> (accessed May 26 2014)

is created. It is important to note that these projections do not contain phase values (there are no axes) but future development should enable specific information to be directly read from such a visualisation method.

### 3.2.1 Simplexes

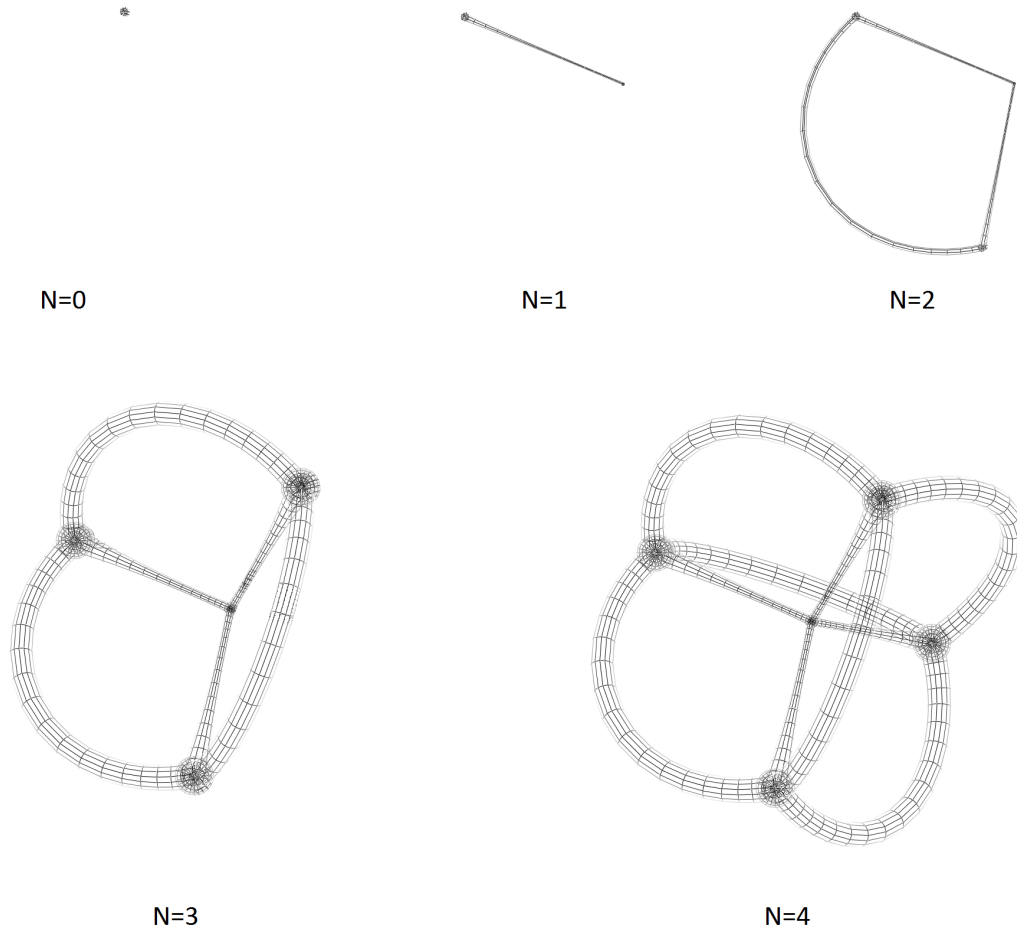


Figure 3.2: Simplexes for increasing number of dimensions  $N$ .

A simplex is the structure with the lowest number of nodes for any given dimension. Take for instance a dot. A dot has zero dimensions and is therefore a zero dimensional simplex. In most cases, as will be explained in Section 3.3, simplexes are generally the most power efficient format in any given number of dimensions. Figure 3.2 shows how a simplex may look moving from zero dimensions ( $N = 0$ ) up to four dimensions ( $N = 4$ ). A simplex, in this case, can be thought of as moving to higher dimensions by adding a point and connecting vertices to it from all existing points. The number of nodes is always one greater than the dimension. The thickness and curvature of the vertices in Figure 3.2, particularly in the case of  $N = 4$ , is due to the stereographic

projection. Reusing the bubble analogy the projection can be thought of as a small bubble encased within a larger bubble. The small bubble in this case is the single point in the centre while the remaining four points (for the  $N = 4$  case) are projected onto the surface of the outer bubble. This projection technique is what gives the image the apparent three-dimensional perception with the vertices having a thickness relating to the distance to the invisible outer spherical boundary.

### 3.2.2 DP-QPSK in Four Dimensions

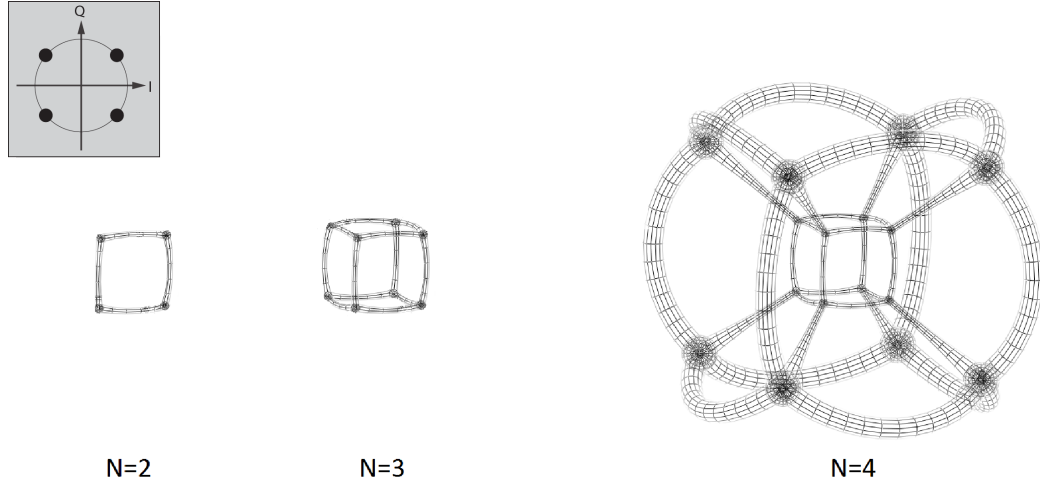


Figure 3.3: Construction of a four dimensional cubic constellation.

Figure 3.3 shows how a cubic constellation is constructed. The plot on the far right of Figure 3.3 shows a four dimensional representation of DP-QPSK. DP-QPSK is a constant intensity modulation format that has eight symbol states, four in each polarisation, where the eight states are  $\phi_{x,y} = 3\pi/4, \pi/4, -\pi/4, -3\pi/4$ . However, from Equation 3.2, DP QPSK also has absolute and relative phases in multiples of  $\pi/4$ . Therefore, DP-QPSK has a total of sixteen possible phase states shared across four states of polarisation (where the four states are positive and negatively linear, right hand circular and left hand circular). With sixteen phase states DP-QPSK is a cubic constellation format when viewed in four dimensions. All sixteen phase locations can be views as the nodes in Figure 3.4 where the vertices are coloured to show changes in polarisation corresponding to relative phase changes, where red a green correspond to positive and negatively polarised states with relative phases of  $\phi = 0$  and  $\phi = \pm\pi/2$  respectively and blue and orange represent right-hand circular ( $\phi = -\pi/4, 3\pi/4$ ) and left-hand circular respectively ( $\phi = \pi/4, -3\pi/4$ ). When viewed on a standard constellation diagram (similar to Figure 3.3 for  $N = 2$ ) in both x- and y-polarisation, the maximum number of distinct phase states is eight, this clearly shows that there is an advantage to using stereographic projection as all states of phase are represented. In

the case of DP-QPSK it becomes clear that there are redundant states of phase that are not encoded with binary information. From this point of view it begins to become obvious that DP-QPSK is not operating at an optimum power efficiency. This will be covered in more depth in Section 3.3.

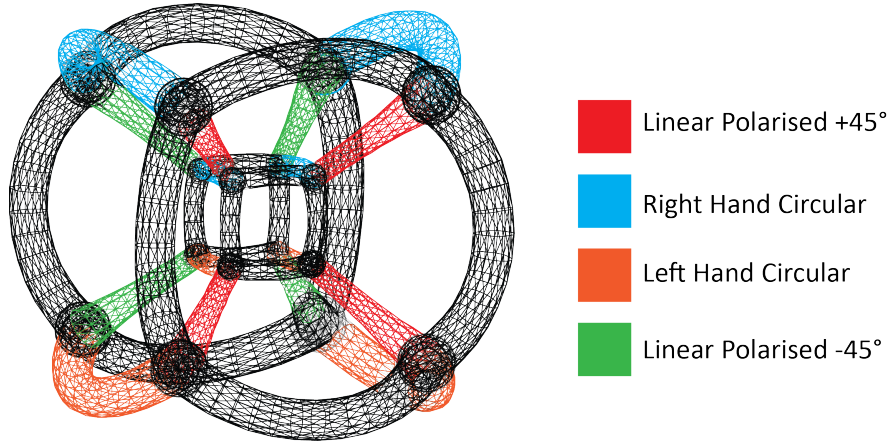


Figure 3.4: DP-QPSK visualised in four dimensions using stereographic projection.

### 3.2.3 PS-QPSK in Four Dimensions

In many ways the representation for PS-QPSK is significantly reduced in complexity from DP-QPSK. In a conventional constellation diagram PS-QPSK is similar to QPSK where a QPSK signal is transmitted on *either* the x- or y- polarisation, in contrast to DP-QPSK where a QPSK signal is transmitted on *both* polarisations. This means that PS-QPSK has the same initial eight phase states ( $\phi_{x,y} = 3\pi/4, \pi/4, -\pi/4, -3\pi/4$ ), however, as the data is transmitted in *either* polarisation at any given bit interval there is no relative phase ( $\phi_r = 0$ ). Therefore there are no additional phase states for PS-QPSK. From this point of view PS-QPSK can be visualised as a subset of DP-QPSK. This sim-

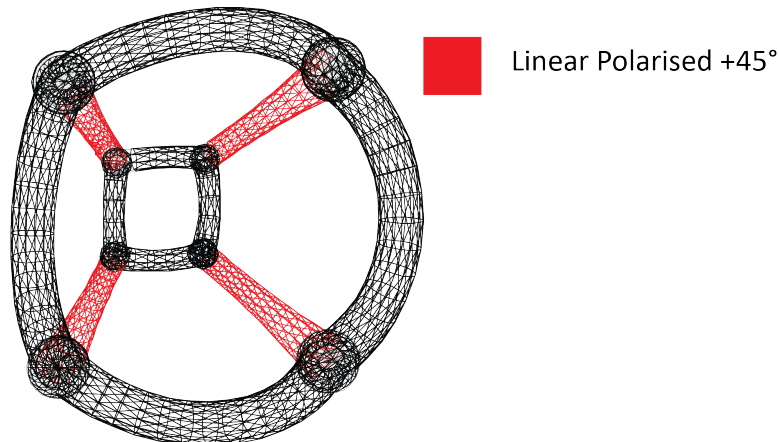


Figure 3.5: PS-QPSK viewed as a subset of DP-QPSK, showing all symbol states relevant to PS-QPSK.

plified visualisation is shown in Figure 3.5 where the amplitude in one polarisation or another will reduce to zero leaving zero relative phase shift and a constellation diagram similar to standard QPSK with a single point in the centre when viewing a single polarisation, indeed this is what was seen during experiments and can be seen in Section 3.4.

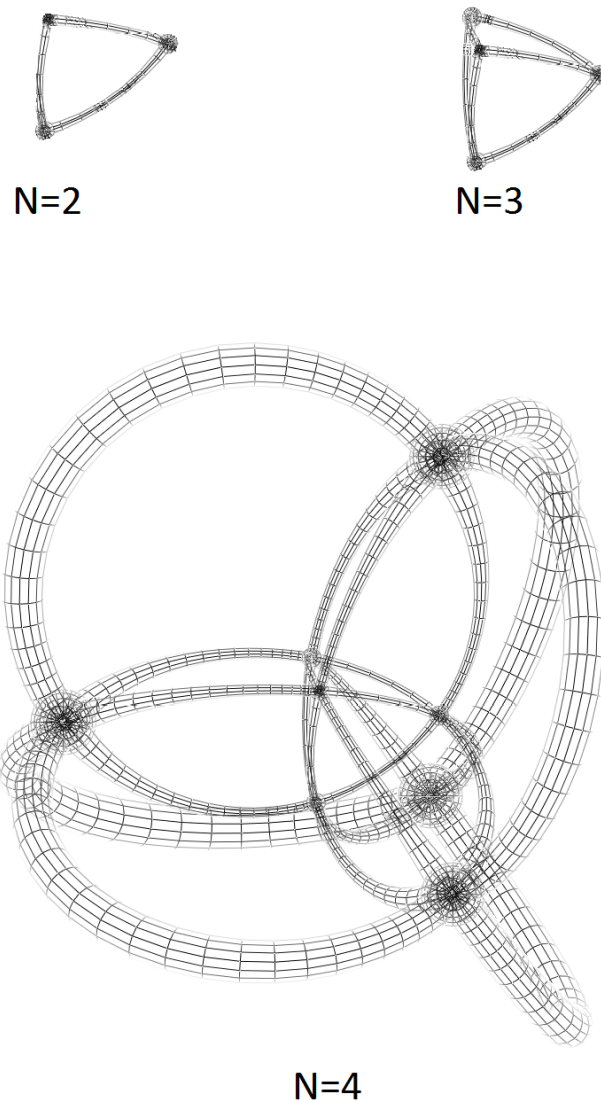


Figure 3.6: Triadic constellation for increasing dimensions

However, investigating PS-QPSK in more detail it can also be taken as a triadic constellation format where all eight phase states are used to construct a four-dimensional

shape without being a subset of DP-QPSK. Figure 3.6 shows how a triadic constellation is constructed moving from  $N = 2$  to  $N = 4$ , where  $N$  denotes dimension. For  $N = 2$  this is similar to 3PSK and is known to be an efficient format but impractical for digital transmission as it does not have an efficient bit-mapping solution.  $N = 3$  is infeasible in a real system as it is impossible neglect amplitude or phase when moving to another polarisation. Therefore,  $N = 4$  is the first triadic constellation that is possible to implement in a real life system. While having eight symbols means that bit-mapping is easy to solve and makes PS-QPSK a candidate for digital transmission.

### 3.3 What is Meant by Power Efficient?

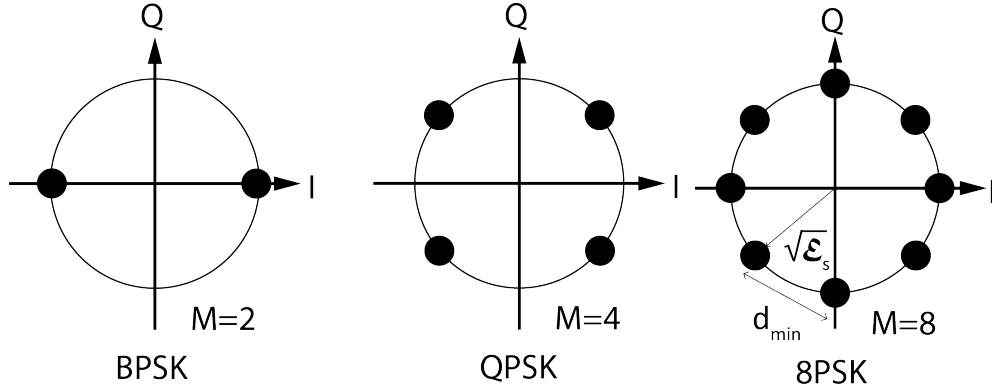


Figure 3.7: Two Dimensional constellations for increasing number of symbol states  $M$ .

#### 3.3.1 Comparing the Efficiency of Modulation Formats

Karlsson and Agrell were first to identify PS-QPSK as a power efficient modulation format [72]. They approached the problem by considering dual-polarisation formats as having four degrees of freedom as explained in Section 3.1. From here the problem of efficiency became a sphere-packing problem in four dimensional hyperspace [72, 73]. The sphere packing problem in optical modulation formats can be thought of as reducing the energy per bit to its lowest value while maintaining equal distance between adjacent symbols in euclidean space. Modulation formats can then be compared by using the *asymptotic power efficiency*, where the number of bits per unit energy is expressed as [72, 74]

$$\gamma_\eta = \frac{d_{min}^2}{4\mathcal{E}_b} \quad (3.4)$$

where  $\mathcal{E}_b$  is defined as the energy per bit

$$\mathcal{E}_b = \frac{\mathcal{E}_s}{\log_2 M} \quad (3.5)$$



where  $d_{min}$  is the minimum distance between adjacent constellation points,  $M$  is the number of symbol points and  $E_s$  denotes the signal energy as illustrated in a simple two dimensional case in Figure 3.7. Studying the two dimensional case (see Figure 3.7) it is possible to infer from the diagrams that the modulation formats can be made more efficient by maintaining signal energy  $E_s$  while increasing the number of symbol points,  $M$ , as is the case moving from BPSK ( $M = 2$ ) to 8PSK ( $M = 8$ ). A further way to increase efficiency is to reduce the signal energy  $E_s$ , this would reduce the overall signal space represented in Figure 3.7. The challenge with this approach is that for real modulation formats the constellation points take up signal space and can increase in size for a number of reasons, such as the introduction of noise due to transmission. For optimum energy performance, all signal points should be an equidistant apart from one another in euclidean space. This is where the four-dimensional visualisation techniques discussed in the previous section become particularly useful. The challenge of reducing the signal energy is a circle packing problem for the example formats shown in Figure 3.7, where the signal energy is reduced to the point just before the symbols overlap. For dual polarisation formats this becomes slightly more complex as the symbol states are considered spheres. Indeed when comparing DP-QPSK to PS-QPSK from Figures 3.4 and 3.6 ( $N = 4$ ) it becomes clear that as the symbols are packed together the PS-QPSK has a more efficient solution. This can also be solved mathematically [75], but is beyond the scope of this thesis.

In the case where all symbols have equal likelihood and equal power (i.e. DP-QPSK and PS-QPSK) the power of the transmitter is defined as

$$P = R\mathcal{E}_b \quad (3.6)$$

where  $R$  is the baud rate [74]. In order to improve capacity of networks it is essential that high baud rates can be utilised, to do this without greatly increasing the power requirement of the system requires the reduction of the signal energy per bit.

One of the ways that energy per bit can be reduced is by increasing spectral efficiency. Spectral efficiency relates to the maximum amount of digital information that is conveyed in a certain time interval for a finite bandwidth and is measured in units of bits/s/Hz/pol. Spectral efficiency can also be expressed as

$$SE = \frac{\log_2 M}{\frac{N}{2}} \quad (3.7)$$

where  $N$  is the number of dimensions. The standard way of comparing modulation formats is to compare spectral efficiency against the sensitivity penalty. The sensitivity penalty is defined as  $1/\gamma_\eta$ . The spectral efficiency can be thought of as the governing factor to reducing the energy per bit while the sensitivity penalty is used as a metric to indicate the likelihood of symbols overlapping and thus require more sensitivity to de-

tect. It becomes clear that simple structures such as the simplexes will have the lowest sensitivity penalty as they have more efficient sphere packing solutions and constellations with a greater number of symbols such as DP-QPSK will have greater spectral efficiencies. The trade off between spectral efficiency versus sensitivity penalty was carried out by [67] for a range of constellations with a varying number of symbols  $M$  and for dimensions up to  $N = 4$ . It was found that simplexes were the most efficient formats for  $N = 2$  and 3. For  $N = 4$  it was found that a triadic constellation (as explained in Section 3.2.3) with eight symbol points ( $M = 8$ ) constituted the most efficient format and was dubbed PS-QPSK due to technique in which the format is implemented by modulating (or switching) between polarisations. The implementation of the PS-QPSK format is covered in Section 3.4.

### 3.3.2 Power Efficient Modulation Formats in the Literature

Karlsson and Agrell [67, 68] first identified PS-QPSK as the most power efficient format. A 1.76dB better asymptotic sensitivity than binary PSK was predicted. However, if the optimal FEC decoding technique that is specially designed for a non-gray-coded system is not employed [76, 77] the sensitivity gains are generally lower. Other groups first simulated PS-QPSK's performance [78, 79, 80] for 100Gb/s WDM transmission and showed higher nonlinear tolerance compared to DP-QPSK. Masalkina et al. [81] demonstrated PS-QPSK sub-carrier modulation with iterative mapping on optical orthogonal-frequency-division-multiplexing. More recently, the Chalmers group reported the first experimental demonstration of PS-QPSK at 30Gb/s on a single-channel over a 300km transmission length [82] and reported a modified constant modulus algorithm for PS-QPSK [83]. The work in this chapter has contributed by performing experimental implementation of the PS-QPSK format and comparison to DP-QPSK in a WDM system [84]. Since these early publication there has been continued interest in power efficient formats [72], with recent interest moving to higher complexity four dimensional formats such as 6PolSK-QPSK [85, 86] where the signal is encoded across six states of polarisation.

## 3.4 PS QPSK and Experiments

This section covers results published as part of an industrial collaboration with AT&T where we reported, to our knowledge, the first experimental demonstration of the PS-QPSK format with coherent reception and digital signal processing (DSP) in a typical terrestrial WDM system and a comparison to DP-QPSK at the same bit rate of 40.5 Gb/s. The low symbol rates of 13.5 Gbaud for PS-QPSK and 10.125 Gbaud for DP-QPSK were chosen so that bandwidth limitations of the transmitter/receiver components did not significantly impact the comparison. The modulation formats' per-

formances were compared for single-channel, back-to-back, assuming hard-decision forward-error-correction, and for  $10 \times 100$  km WDM transmission over standard SMF with 50-GHz-spaced neighbouring channels of the same modulation format. For PS-QPSK, in a parallel effort to that of [87], we developed a novel constrained multi-modulus algorithm, which has improved performance to that reported in [83]. Results indicate a clear performance advantage of PS-QPSK over DP-QPSK, including 0.9dB sensitivity improvement for back-to-back (at  $10^{-3}$  bit-error-ratio) and up to 1.6dB higher launch power tolerance.

### 3.4.1 Constructing a PS-QPSK Transmitter

Two possible transmitter designs were first suggested by Karlson et al. for the implementation of PS-QPSK [72]. One design consisted of a modified DP-QPSK modulator where the input logic of the DP-QPSK modulator was controlled by two XOR gates so as to reduce the number of constellation bits from 16 to 8. The XOR gates are placed so as to force the additional constellation points onto ones that are only permissible states for PS-QPSK. The truth table for this approach is presented in Table 3.1, where D1 to D4 represent the four RF data streams that are connected to the DP-QPSK modulator where an intermediate XOR function between D1 and D2 is referred to as F1.

Table 3.1: Truth Table to achieve PS-QPSK using the four data inputs of a DP-QPSK modulator (D1-D4)

D1	D2	D3	F1=D1 XOR D2	D4=D3 XOR F1
0	0	0	0	0
0	0	1	0	1
0	1	0	1	1
0	1	1	1	0
1	0	0	1	1
1	0	1	1	0
1	1	0	0	0
1	1	1	0	1

The second approach and the one used in the following experiments consisted of a QPSK modulator and polarisation modulator in series, as shown in Figure 3.8 (left). An external cavity laser (ECL) with 100kHz linewidth at 1550nm is followed by a double-nested Mach-Zehnder modulator with a 3dB bandwidth  $>28$ GHz, to which  $2^{15} - 1$  pseudo-random bit sequence (PRBS) are applied. This PRBS was initially chosen and later the PRBS was increased to  $2^{31} - 1$  when taking WDM measurements. The RF signal was generated from a pattern generator and amplified by drivers with 30GHz bandwidth. For PS-QPSK, the QPSK signal passes through a single-drive polarisation modulator (Versawave PL-40G-5) having 40GHz bandwidth, where an applied RF drive voltage switches the polarization between two orthogonal states.

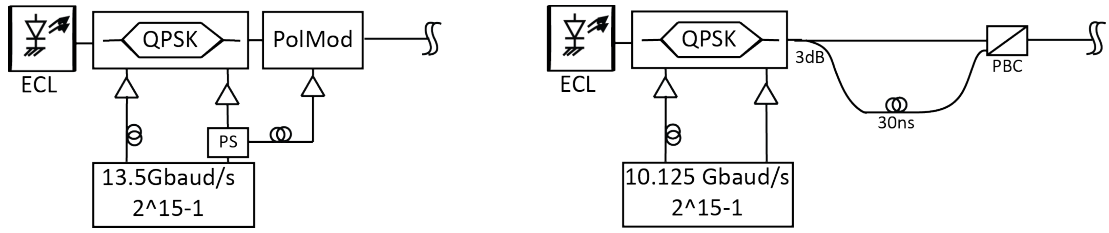


Figure 3.8: PS-QPSK Transmitter (left) and DP-QPSK Transmitter (right)

In order to make a comparison to DP-QPSK a transmitter was constructed by again using a double-nested Mach-Zehnder modulator (Figure 3.8 right), driven with a PRBS at 10.125 Gb/s. This baud rate was chosen to be lower than the PS-QPSK transmitter to have a comparable bit rate. From the Mach-Zehnder modulator the signal passes through a polarisation-multiplexing stage consisting of a 3dB coupler where the signal passed through a 30 ns delay in one arm relative to the other in order to decorrelate between the polarisations after which the signal is recombined in a polarization beam combiner.

### 3.4.2 Back-to-back Sensitivity Comparison

A simple setup was used for the investigation of the back-to-back sensitivities, as shown in Figure 3.9, where the PS-QPSK transmitter shown is swapped with the DP-QPSK transmitter shown in Figure 3.8 (right).

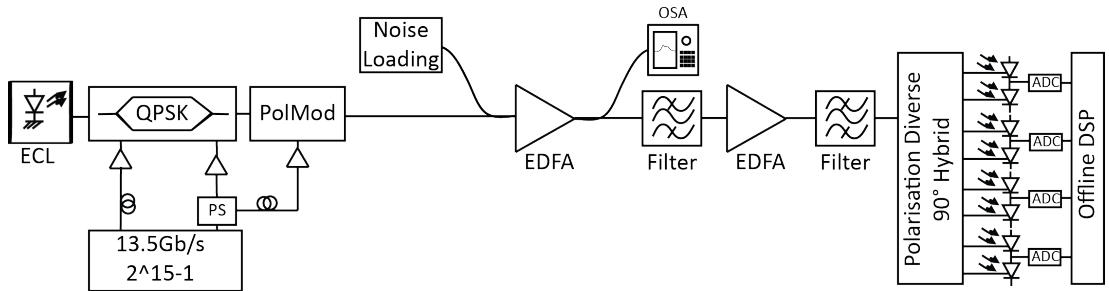


Figure 3.9: Experimental set-up for PS-QPSK back-to-back measurements. For DP-QPSK, a polarization multiplexing stage replaces the polarisation modulator, and 10.125Gb/s data signals are applied to the QPSK modulator.

In order to noise-load the channel, amplified spontaneous emission from an erbium-doped fibre amplifier (EDFA) was used, followed by an attenuator that controlled the amount of noise added to the link. Once the noise was added the signal was amplified through a two stage optical amplifier and filtered via passband filters with 36 GHz bandwidth. A polarization and phase-diverse coherent receiver follows, consisting of a polarization-diverse 90 deg hybrid, a local oscillator (LO) of  $\sim 100$  kHz linewidth, and four balanced 20 GHz photo-detectors. A four-channel real-time sampling oscil-

loscope with 50 GSa/s sample rate and 18 GHz analogue bandwidth performs the sampling and analogue to digital conversion (ADC), and a desktop computer then post-processes the captured data.

Before taking coherent measurements and carrying out offline processing the system was also altered to allow tuning with direct detection. This was done using a direct detector with a polarisation beam splitter and polarisation switch. This allowed each polarisation to be viewed independently and the switch allowed both polarisations to be viewed in quick succession. This allowed the delays in the transmitter to be set correctly where the eye diagrams for both PS-QPSK and QPSK can be seen in Figure 3.10. For the QPSK format (Figure 3.10(right)) the eye diagram was the same in both polarisations where the bit transition is characterised by an amplitude modulation where the amplitude modulation is a characteristic of Mach-Zehnder modulators as a drive signal will cause the Mach-Zehnder to momentarily pass through a null in its transfer function, causing a change in amplitude. The phase encoded bits are encoded between the points of amplitude modulation. For DP-QPSK the eye diagram in each polarisation remains the same in both polarisations with a 30 ps delay between both polarisations. For the PS-QPSK format both x- and y-polarisations have similarly structured eyes with a slight delay between the two. The eye consists of amplitude modulations similar to QPSK and a low rail at zero amplitude. This lower eyelid is due to half the power being transmitted on the opposite polarisation. The bits are transmitted at the points where the eye is open and the delays are set to maximise the opening of the eye.

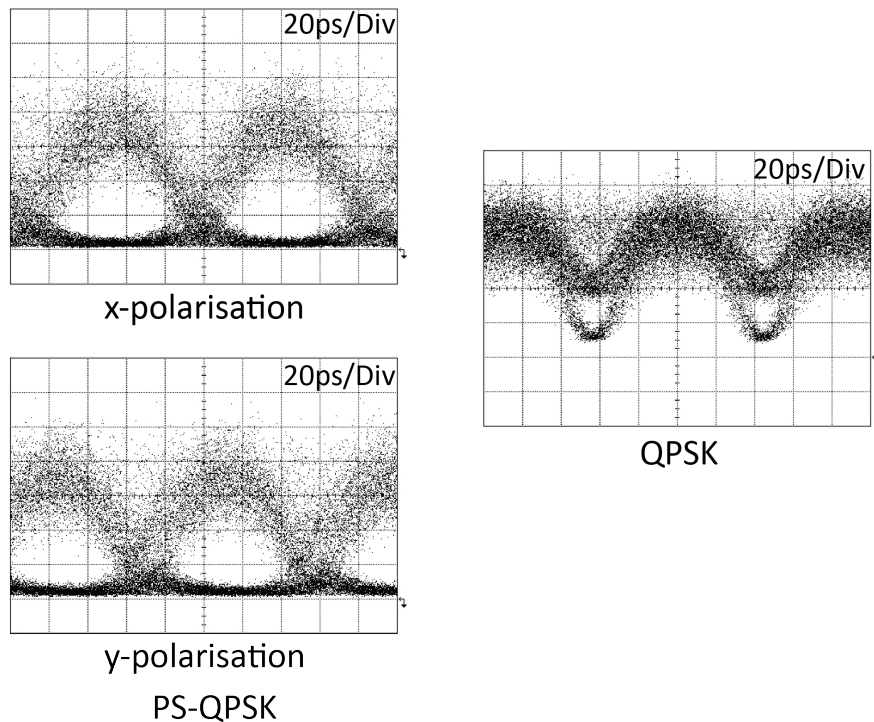


Figure 3.10: Eye diagrams of PS-QPSK in each polarisation (left) and QPSK (right).

Figure 3.11 shows a comparison of the back-to-back sensitivities in terms of signal-to-noise ratio ( $E_b/N_0$ ) using coherent detection and offline signal processing, discussed in Section 3.4.3, where  $N_0$  is the power spectral density of the additive noise. At a BER of  $10^{-3}$ , PS-QPSK shows a 0.9 dB improvement in sensitivity compared to DP-QPSK, assuming hard FEC, agreeing well with the 0.97dB difference according to theory [68] and an independent demonstration of PS-QPSK sub-carrier modulation [82]. The sensitivity difference increases to 1.5dB at  $10^{-5}$  BER, indicating that it is approaching the asymptotic sensitivity difference of 1.76dB first reported by Karlsson [67].

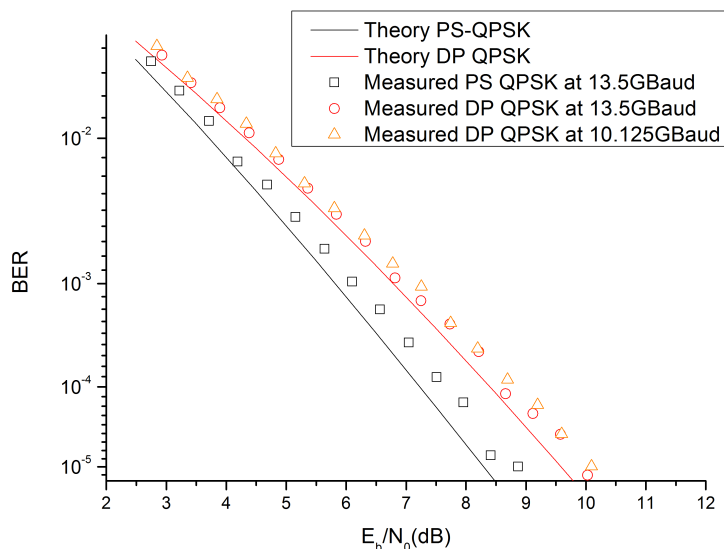


Figure 3.11: Back-to-back measurements for PS-QPSK and DP-QPSK

### 3.4.3 Receiver DSP Algorithms

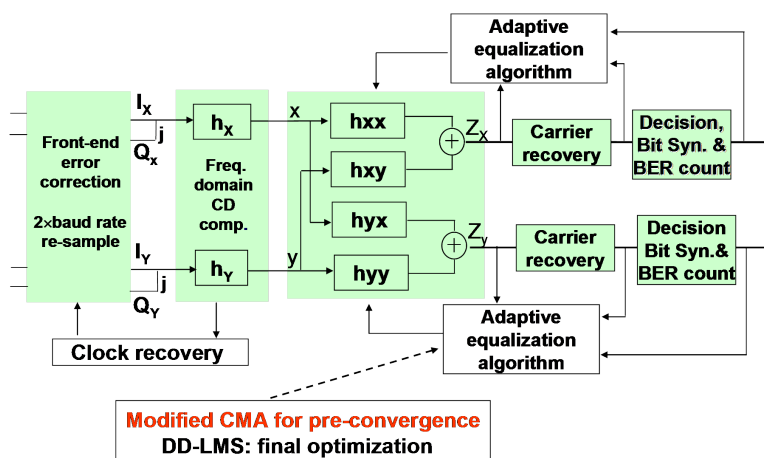


Figure 3.12: Offline digital signal processing flow chart.

The DSP presented here was done as part of an industrial collaboration and was de-

veloped primarily by Dr. Xiang Zhou. The author was in charge of capturing and processing the experimental data using the previously developed algorithms, where the constrained multi-modulus algorithm was developed through discussions with both Dr. Zhou and the author. The flow chart diagram for the offline receiver DSP used in the experiment is shown in Figure 3.12. After digital compensation of optical front errors (sampling skews and hybrid phase errors) and anti-aliasing filtering, the 50 GSa/s signal is first down-sampled to a sample rate (approximately) equal to 2 times baud rate. After that, the bulk chromatic dispersion (CD) is compensated using a frequency-domain based static equaliser. Note that CD compensation is only used for the transmission experiments covered in Section 3.4.4. The clock used to re-sample the signal is extracted by using the classic “square and filter method.” Next, we perform simultaneous polarisation recovery and residual CD compensation by using a 13-tap,  $T/2$ -spaced  $2 \times 2$  adaptive equaliser. This adaptive equaliser is initialised by using decision-independent blind equalisation algorithms (for pre-convergence), where the classic constant modulus algorithm (CMA) is used for DP-QPSK and a new constrained multi-modulus algorithm (MMA), developed by Dr. Xiang Zhou, is used for PS-QPSK. Once convergence is reached, the decision-independent algorithms switch to a decision-directed least-mean-square (DD-LMS) algorithm for stable-state operation. Note that the traditional CMA [88] or multiple modulus algorithm (MMA) such as the cascaded MMA [89] cannot be used for polarisation de-multiplexing of a PS-QPSK signal, because the signal components in the two orthogonal polarisation states are correlated and the equaliser may converge to any combination of two phase-shifted QPSK signals. The proposed constrained MMA exploits the signal correlation between the two orthogonal polarisations and de-multiplexes the PS-QPSK signal in each of the two orthogonal polarisations as a five-point constellation  $(1, j, -1, -j, 0)$ , as can be seen in Figure 3.13b. Let  $Z_x(n)$  and  $Z_y(n)$  represent the equalised signals and  $R_x(n)$  and  $R_y(n)$  denote the expected square values of the radius/modulus of the constellation in the  $x$  and  $y$  polarisations, respectively. The constrained MMA calculates the feedback errors from

$$\begin{aligned}\mathfrak{E}_x(n) &= |Z_x(n)|^2 - R_x(n) \\ \mathfrak{E}_y(n) &= |Z_y(n)|^2 - R_y(n)\end{aligned}\tag{3.8}$$

where

$$\begin{aligned}R_x(n) &= E\left\{|Z_x(n)|^2 + |Z_y(n)|^2\right\} \text{ and } R_y(n) = 0, \text{ if } |Z_x(n)|^2 > |Z_y(n)|^2 \\ R_x(n) &= 0 \text{ and } R_y(n) = E\left\{|Z_x(n)|^2 + |Z_y(n)|^2\right\}, \text{ if } |Z_x(n)|^2 < |Z_y(n)|^2\end{aligned}\tag{3.9}$$

For the case when  $|Z_x(n)| = |Z_y(n)|$ , we let  $\mathfrak{E}_x = \mathfrak{E}_y = 0$ . Our experimental results have shown that the constrained MMA has very robust convergence performance and

therefore can be used as either an independent blind equalisation algorithm for PS-QPSK or as a pre-equalisation algorithm. Because this algorithm inherently minimises the cross correlation between the two orthogonal polarizations, the singularity problem is much less likely to occur as compared to the CMA for DP-QPSK. In Figure 3.13 (a) and (b) we show the recovered constellation diagrams for 40.5 Gb/s DP-QPSK and 40.5 Gb/s PS-QPSK, respectively, for back-to-back measurements without additional loading noise. The five point constellation shown for PS-QPSK is comparable to Figure 3.5 where four of the points collapse due to there being a signal on only a single polarisation at any given sampling interval.

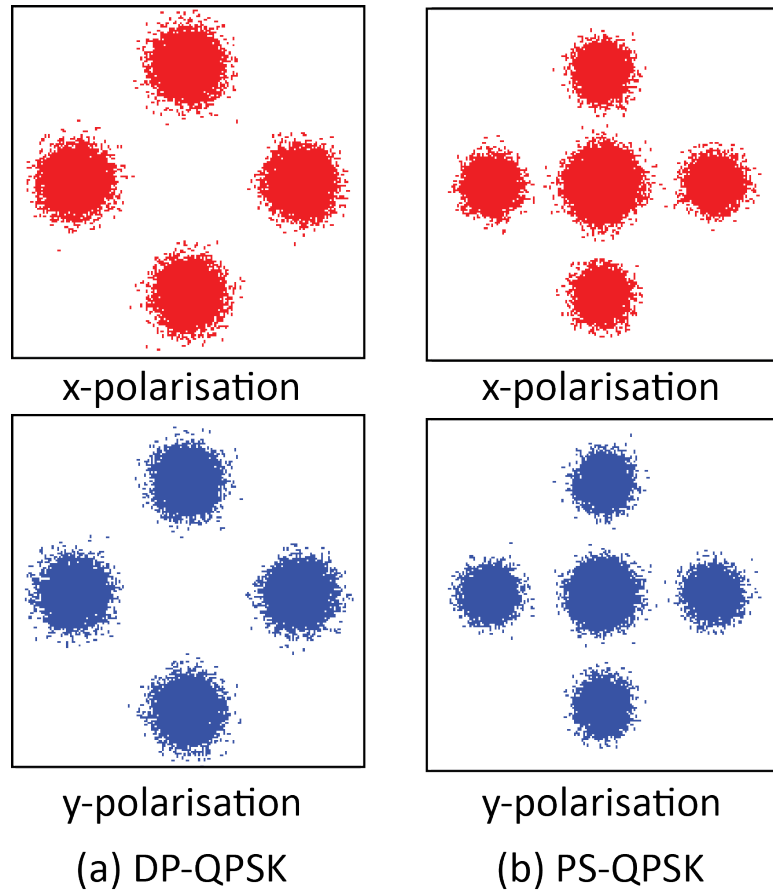


Figure 3.13: Recovered constellation diagrams for back-to-back measurement of (a) 40.5Gb/s DP-QPSK and (b) 40.5Gb/s PS-QPSK.

Carrier frequency and phase recovery are implemented after the initial equalisation stage. The frequency offset between the LO and the signal is estimated by using a constellation-assisted two-stage blind frequency search method [90]: the frequency offset is first scanned at a step size of 10 MHz and then at a step size of 1 MHz, and the optimal frequency offset is the one that gives the minimum mean-square error. For each trial frequency, the carrier phase is first recovered (with best effort) by using a proposed two-stage phase estimation algorithm [91], and decisions made following this phase estimation are then used as reference signals for mean-square error cal-



culation. Note that this frequency recovery method is applicable for any modulation format and can reliably recover carrier frequency by using only tens of symbols (64 are used in this experiment). The carrier phase is estimated by using a two-stage method: the carrier phase recovered from the previous symbol is first fed back and used as an initial test phase angle. The “decided” signal made following this initial test phase angle is then used as a reference signal for a more accurate maximum-likelihood (ML) based phase recovery through a feed-forward configuration [91]. To reduce the probability of cycle slipping (no differential coding/encoding is applied in this experiment), sliding-window based symbol-by-symbol phase estimation is employed, and the window size is optimized for each case. For PS-QPSK only half of the symbols can be used for phase estimation for each polarisation, while for DP-QPSK all the symbols are used for the phase estimation, for fair comparison, joint x- and y-polarisation phase estimation is only applied to PS-QPSK. For symbol-to-bit mapping, the principle described in [67] has been used for PS-QPSK. For bit-error-ratio (BER) calculation, errors are counted over more than  $1.2 \times 10^6$  bits of information.

#### 3.4.4 Transmission Experiment

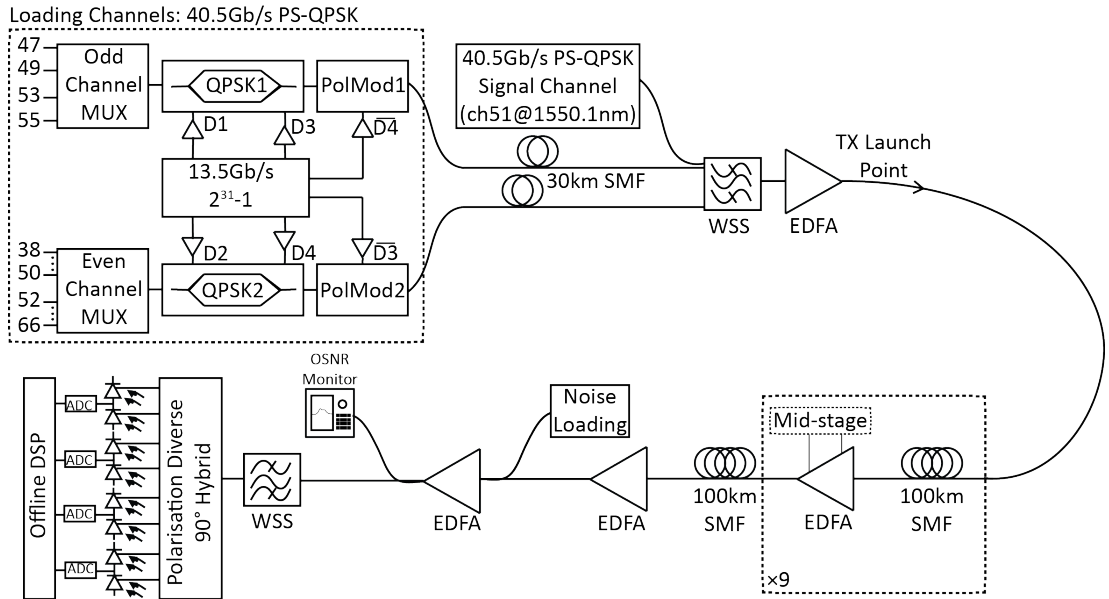


Figure 3.14: Experimental set-up for WDM transmission experiments over  $10 \times 100$  km of standard SMF.

A full transmission system set-up, as shown in Figure 3.14, was used to investigate the performance of PS-QPSK compared to that of DP-QPSK in a WDM transmission system. The transmitters for the channel-under-test at 1550.14 nm were the same as those used for the back-to-back sensitivity measurements for PS-QPSK and DP-QPSK. As shown in Figure 3.14, an additional 19 C-band loading channels were combined

with the signal channel in a 50 GHz wavelength selective switch (WSS), such that there were five 50 GHz-spaced channels on both sides of the channel-under-test as well as nine additional channels at 100 GHz spacing to load the EDFAs. The resulting WDM spectrum can be seen in Figure 3.15 where all channels are shown with their respective power and spacing. The spectrum was measured at the output of the final EDFA after 1000 km of transmission for an output power of 17 dBm where the power axis in Figure 3.15 was adjusted to account for the loss of the coupler.

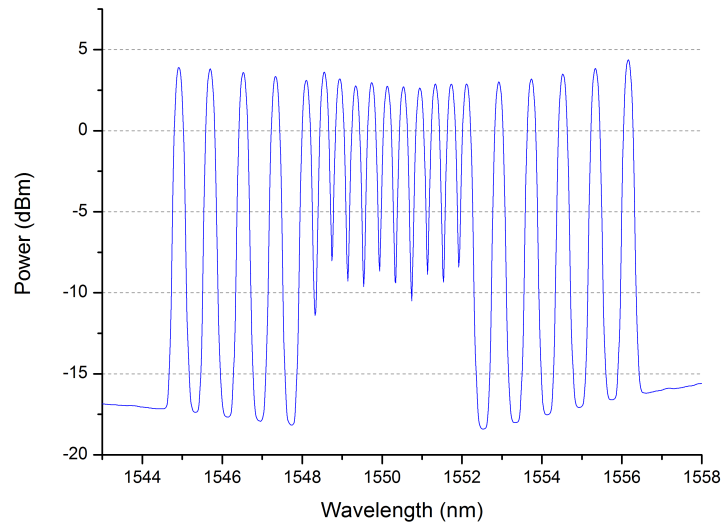


Figure 3.15: WDM spectrum of PS-QPSK after transmission over 1000 km of fibre.

At the transmitter, the sets of odd and even loading channels were independently modulated with the same modulation format and bit-rate as the channel-under-test and were transmitted through 30 km spools of standard SMF for decorrelation. The transmission line consisted of ten 100 km spans of standard SMF (average 20.5 dB loss) and two-stage erbium-doped fibre amplifiers (EDFA) that were set to launch a flat spectrum into the fibre spans for output powers ranging from 10 to 19 dBm ( $-3$  to  $+6$  dBm/ch). No optical dispersion compensation was used. A wavelength blocker and WSS at the mid-stage of the EDFAs after spans 3 and 6, respectively, allowed for individual channel power equalisation to compensate the accumulated EDFA gain ripple. After the tenth SMF span, the signals were noise-loaded and the channel-under-test was selected with a WSS and sent to the previously described polarisation- and phase-diverse coherent receiver.

For both modulation formats and a 9 dB range of launch powers into the SMF spans, we recorded the sampled and digitised data sets after the 1000 km transmission for different levels of noise-loading of the channel-under-test. The received OSNRs, without additional noise loading after 1000 km transmission, ranged from 16.3 dB to 25.0 dB

for  $-3$  dBm/ch to  $+6$  dBm/ch launch power, respectively. The DSP algorithms described in Section 3.4.3 were then used to calculate curves of bit-error-ratio (BER) versus received OSNR, as shown in Figure 3.16 for PS-QPSK. These results were in agreement with the WDM simulations of [76, 77] and show a noise floor as power per channel increase due to the onset of nonlinearities. As shown in Figure 3.16, at 4 dBm per channel launch power, PS-QPSK had less than 2 dB OSNR penalty relative to its back-to-back (at  $\text{BER} = 10^{-3}$ ), whereas DP-QPSK had more than 4 dB OSNR penalty relative to its back-to-back at the same  $10^{-3}$  BER, indicating that PS-QPSK has higher nonlinear tolerance.

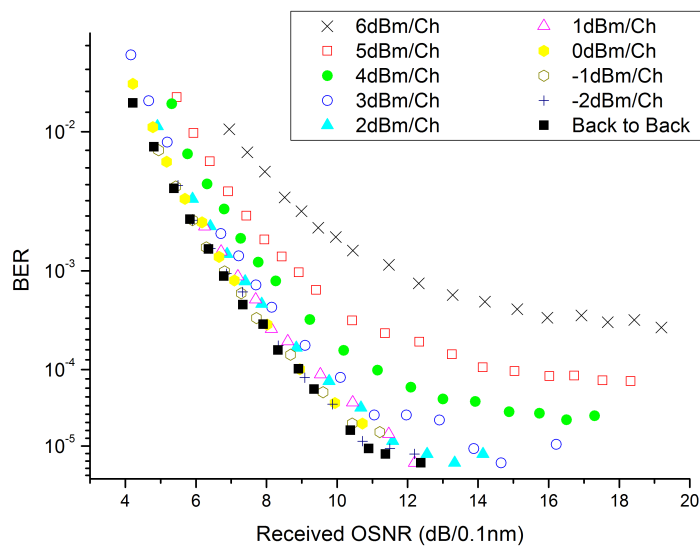


Figure 3.16: BER versus received OSNR for PS-QPSK after WDM transmission over  $10 \times 100$  km SSMF.

The curves of BER versus received OSNR for both modulation formats were then used to calculate the required OSNRs for  $10^{-3}$  and  $3.8 \times 10^{-3}$  BER by using standard quadratic curve fitting with the results plotted in Figure 3.17. Note that the required OSNR for back-to-back in the WDM system setup is shown by the points furthest to the left with the origin of the x-axis referring to the back-to-back configuration. Allowing 1 dB required OSNR penalty relative to each modulation format's own back-to-back sensitivity at  $10^{-3}$  BER, PS-QPSK could tolerate approximately 1.6dB/ch higher launch power than DP-QPSK for the  $10 \times 100$  km transmission. Adding the 0.9dB improvement in back-to-back sensitivity for PS-QPSK to its higher nonlinear tolerance gives it a 2.5dB overall advantage in terms of OSNR margin compared to DP-QPSK. Of course, the sensitivity and nonlinear tolerance could be utilised to obtain significantly longer reach for PS-QPSK systems. This has been experimentally verified where PS-QPSK was found to have a 30 % greater reach than DP-QPSK for 7-channel WDM transmission over 13640 km [92].

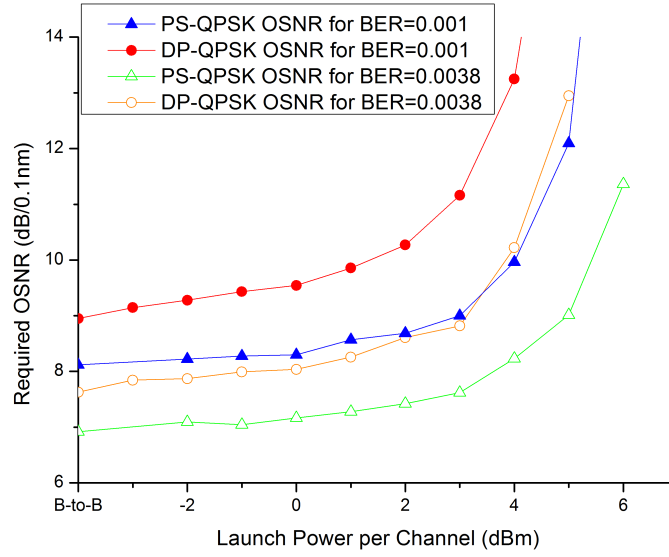


Figure 3.17: Required OSNR for PS-QPSK and DP-QPSK (both at 40.5Gb/s) after WDM transmission over  $10 \times 100$  km SMF for a range of launch powers into the spans.

**PS-QPSK tolerance to nonlinearities:** Nonlinearities can be reduced in a number of ways, the most obvious of which is by reducing the amount of power in the optical fibre. By reducing the energy per bit it is possible to increase the number of bits in the fibre without increasing the overall power density, and concurrently the nonlinearity, in the fibre. The back-to-back results presented here indicate that PS-QPSK has a 0.9dB sensitivity improvement over DP-QPSK indicating that PS-QPSK uses less energy per bit.

In the experiments presented here dispersion is compensated digitally in the receiver for both PS-QPSK and DP-QPSK. The WDM results showed DP-QPSK to have a required OSNR of  $\sim 13.1$  dB/0.1nm at  $10^{-3}$  BER, over 4 dB higher the back-to-back requirement. This compares to a  $\sim 10$  dB/0.1nm required OSNR of PS-QPSK at  $10^{-3}$  BER, indicating that PS-QPSK has bulk OSNR tolerance of 2 dB greater. When investigating optimal launch powers it was found that this bulk improvement can be increased to 2.5 dB. This improvement indicates that PS-QPSK has a greater nonlinear tolerance of over 1 dB given by the power efficiency per bit alone. This has been an area of great interest with many groups studying the benefits of PS-QPSK under such conditions [76, 77, 92]. It has recently been suggested that the benefits of PS-QPSK are purely a result of a trade off between information spectral density versus launch power [93]. This is indeed accurate when studying PS-QPSK as a pure subset of DP-QPSK, as shown in Figure 3.5 and would be similar to the coded implementation of PS-QPSK shown in Table 3.1 where PS-QPSK can be thought of as DP-QPSK with added redundancy. However, polarisation modulation such as PS-QPSK may still have efficiencies over standard multiplexing when considered in the multi-

dimensional visualisation given at the start of this chapter. As mentioned at the time the format is only optimised in phase amplitude and polarisation and does not take frequency into account. It is possible to create new transceivers that switch between multiple polarisations, such as 6PolSk-QPSK [85] that utilise the full signal space as presented in Figure 3.4. A similar approach could be used to design transmitters that modulate in an even greater number of dimensions, such as the frequency or spatial domain to find the most efficient format in all real dimensions.

### 3.5 Chapter Summary

The chapter began by addressing the dimensionality of waves propagating in a fibre where PS-QPSK was found to be a likely candidate as the most efficient modulation format in four dimensions, those being phase and amplitude in two polarisations. A visualisation technique known as stereographic projection was introduced and applied to modulation formats for the first time, to the authors knowledge. It is hoped that such visualisation techniques will be incorporated into detection DSP of future experiments to give added information of relative phases between polarisations when using dual polarisation formats.

An experimental demonstration of the PS-QPSK format in a typical terrestrial WDM system was then presented and compared with the performance of polarisation-multiplexed QPSK at the same bit rate of 40.5 Gb/s. The low symbol rates of 13.5 Gbaud for PS-QPSK and 10.125 Gbaud for DP-QPSK were chosen to avoid bandwidth limitations of the transmitter and receiver components. PS-QPSK and DP-QPSK were compared for a single-channel, back-to-back configuration, and for  $10 \times 100$ km WDM transmission over standard SMF with 50 GHz-spaced neighbour channels of the same modulation format. A novel constrained multi-modulus algorithm for PS-QPSK was also discussed and was developed concurrently to that of [87]. The results demonstrate compelling advantages of PS-QPSK over DP-QPSK, including 0.9dB sensitivity improvement for back-to-back (at  $10^{-3}$  BER) assuming conventional hard-decision forward-error-correction and up to 1.6 dB higher launch power tolerance for a 1 dB penalty in required OSNR relative to back-to-back. Thus, PS-QPSK may be considered a candidate for ultra-long haul transmission while other candidates with higher spectral efficiencies are currently an topic of interest to achieve greater overall capacity [86].

## Chapter 4

# Benefits and Limits of Multi Mode Fibres

*"All of old. Nothing else ever. Ever tried. Ever failed. No matter. Try again. Fail again. Fail better."*  
Samuel Beckett

In order to supply vast amounts of information over optical networks research is constantly trying to improve current networks and imagine optical networks of the future. Chapter 3 of this thesis investigated one possible improvement for current networks. This chapter, along with Chapter 5, investigates some of the more radical approaches that research in the area is currently focused on. Specifically, this chapter investigates the potential for new fibre designs to outstrip the capacity of current SMF. Currently multi-mode fibres and few mode fibres are under intensive study. Though such fibres have potential to deliver greater capacity compared to traditional fibres, and this potential will be discussed in Section 4.1, the design of such fibres leads to significantly complex propagation characteristics. The impact of nonlinear effects in MMF, particularly nonlinear effects between co-propagating modes, is of particular interest in assessing the benefits and limits of such fibres.

This chapter discusses, in Section 4.1, some of the major benefits that can be achieved by using radical new fibres. In order to define the limits of such fibres a series of experiments were carried out in order to understand the propagation characteristics of multi-mode fibres, this work is presented in Sections 4.2 to 4.4. This experimental work focuses on the nonlinear propagation characteristics of multi-mode fibre. Section 4.5 then uses the information garnered from the experimental work to calculate the

limits of multi-mode fibre and ultimately define capacity limits of multi-mode fibres.

## 4.1 Multi-mode and Few Mode Fibres

Multi-mode fibre, as covered in Chapter 2, can support several higher order modes at a particular wavelength by adjusting the core and cladding refractive indices and by increasing the core diameter. As outlined in the chapter introduction, the subject of multi-mode is currently a topic of intense study [94, 95, 96, 97]. Continued growth and demand on optical communication systems has served to ignite an interest in the design and manufacturing of new types of multi-mode fibres. Recently there has been particular interest shown in the area of few mode fibres [98]. These new fibres, along with mode multiplexing, have enabled the demonstration of higher capacities in optical networks [99].

Multi-mode propagation is not new, with much of the prior work showing that cross-mode effects may degrade the signal [100, 101]. It was these inter-mode effects, in some cases between hundreds of modes, made the complexity of multi-mode fibres overwhelming. However, FMFs accommodate only 4 to 6 LP modes, significantly reducing some of the cross-mode effects, whilst still providing for higher capacity.

Another advantage of FMF is the larger effective area, enabling higher optical power densities to be launched into the fibre, without causing a power dependant refractive index change and in so doing reduce nonlinear effects such as self phase modulation and four wave mixing. Given the differential group delay between modes of a FMF, it has been assumed that, unlike multi-mode fibres [102], the nonlinear behaviour of each excited mode would be similar to a single mode fibre with intra-mode effects prevalent [103]. Taking this assumption into account it is possible to calculate the nonlinear Shannon limit for each mode of a FMF, in a similar manner to the material covered in Chapter 2. As can be seen in Figure 4.1, FMF can be used to achieve higher spectral densities compared to single mode fibre. This improvement is largely dependent on the larger effective area of each of the LP modes, the parameters are shown in Table 4.1 were used to model the fibre performance over 2000 km. Further analysis on the nonlinear Shannon limit is covered in greater detail in Section 4.5 but is presented here for clarity.

This simplified approach to FMFs, along with the promise of greater capacity, has lead the community to broadly adopt such fibres. However, as this work will show, some of the assumptions made regarding FMFs are over-simplistic and based on numerical models without a significant amount of experimental verification. To this end experimental measurements were conducted, as part of this thesis, to verify the models in use and measure directly both intra- and inter-mode characteristics. The results of these experiments along with the methods used to acquire them are presented in the following section (Sections 4.2 to 4.4).

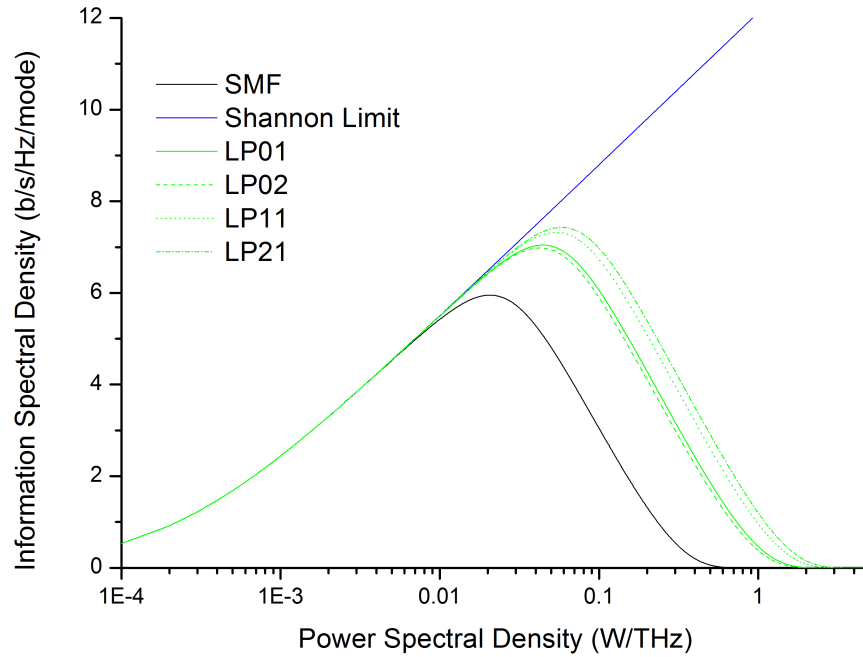


Figure 4.1: Depiction of improved nonlinear performance and greater total capacity of FMFs (green) compared to standard SMF (black). The solid, dashed, dotted and dot-dashed lines correspond to the  $LP_{01}$ ,  $LP_{02}$ ,  $LP_{11}$  and  $LP_{21}$  respectively. The linear Shannon limit is depicted by the blue curve

#### 4.1.1 Fibre in Use

For these experiments, several types of FMF were used. Each fibre was selected specifically for certain characteristics, in order to fully investigate multi-mode propagation. All fibre used was provided by OFS along with useful fabrication and design data. A summary of important parameters, for each fibre, are included in Table 4.1. The parameters for each individual mode were calculated by the refractive index profile of each fibre. Unfortunately, it was not possible to verify these calculations due to the proprietary nature of the refractive index profile. However, experimental measurements carried out on the fibre matched the calculations closely and are discussed in more detail, as required, throughout this chapter. Three different fibre types were used, a four mode fibre, two mode fibre and a four mode fibre designed to have low DGD. It is important that the nonlinear performance of these fibres are understood as each of these fibres has the potential to be deployed in first generation, high capacity, FMF systems [104, 38, 98].

The four mode fibre supported four LP modes at the standard  $1.5 \mu\text{m}$  operating wavelength. The fibre was a step index fibre and was used for all experiments investigating



Table 4.1: Data for OFS few mode fibres. Values for dispersion, dispersion slope and effective area, at 1550nm, are calculated from the index profile for all fibres.

Fibre I: Four Mode Fibre Data				
Lengths (m)	20000	8000		
Core diameter ( $\mu\text{m}$ )	24.8			
Fibre Diameter ( $\mu\text{m}$ )	124.9			
Coating diameter ( $\mu\text{m}$ )	241			
Mode	$LP_{01}$	$LP_{11}$	$LP_{21}$	$LP_{02}$
Dispersion (ps/nm km)	21.1	22.02	21.39	17.54
Dispersion slope (ps/nm km)	0.06559	0.063669	0.05644	0.042717
Effective area ( $\mu\text{m}^2$ )	313.4	420.05	471.23	294.38
Calculated DGD Relative to $LP_{01}$ (ps/m)		2.038	3.89	2.9386
Fibre II: Two Mode Graded Index Fibre Data				
Length (m)	10000			
Core diameter ( $\mu\text{m}$ )	$\approx 25$			
Fibre Diameter ( $\mu\text{m}$ )	125			
Coating diameter ( $\mu\text{m}$ )	240			
Mode	$LP_{01}$	$LP_{11}$		
Dispersion (ps/nm km)	29.93	20.095		
Dispersion slope (ps/nm km)	0.0666	0.06532		
Effective area ( $\mu\text{m}^2$ )	96.17	190.87		
Calculated DGD Relative to $LP_{01}$ (ps/m)		0.144		
Fibre III: Low DGD FMF Data				
Length (m)	29980			
Core diameter ( $\mu\text{m}$ )	$\approx 24.8$			
Fibre Diameter ( $\mu\text{m}$ )	125.1			
Coating diameter ( $\mu\text{m}$ )	240			
Mode	$LP_{01}$	$LP_{11}$	$LP_{21}$	$LP_{02}$
Dispersion (ps/nm km)	18.7	19	18.6	17.9
Dispersion slope (ps/nm km)	0.068	0.068	0.065	0.063
Effective area ( $\mu\text{m}^2$ )	91	91	122	183
Measured DGD Relative to $LP_{01}$ (ps/m)				
Inner End		0.25	0.27	0.3
Outer End		0.47	0.66	0.5

FMF nonlinearity, with the exception of investigations into four wave mixing effects. Two separate lengths of the fibre were used, 20 km and 8 km. This was done in order to discriminate pulses of separate modes in the temporal domain by using the fibre's own DGD. The 8km fibre was used as it was approximately one soliton length of the primary  $LP_{01}$  mode (see Section 4.3 for more details).

The two mode fibre supported two LP modes at the standard  $1.5\mu\text{m}$  operating wavelength. The fibre has a graded index profile, which helps minimise modal dispersion. It was used in conjunction with the four mode fibre to carry out measurements of self

phase modulation, the results of which are presented in Section 4.3.

Finally, a low differential group delay fibre, supporting four LP modes at the standard  $1.5\mu\text{m}$  operating wavelength, was used. A 30km length of this fibre was used for experiments investigating four wave mixing effects in FMF. Results of these tests can be found in Section 4.4.

## 4.2 Investigations into Stimulated Brillouin Scattering in FMF

The first of the prevalent nonlinear propagation effects investigated in few mode fibre was the Stimulated Brillouin Scattering (SBS) effect. SBS is an inelastic scattering process, meaning that there is a direct transfer of optical energy into the material dielectric causing a nonlinear response. For SBS this results in the generation of an acoustic wave through a phenomenon known as electrostriction [105, 106], causing a periodic modulation of the refractive index of the material. The scattering occurs between the light wave and the induced acoustic phonon. In order to investigate SBS in FMF the setup in Figure 4.2 was constructed. The set-up consists of several key parts.

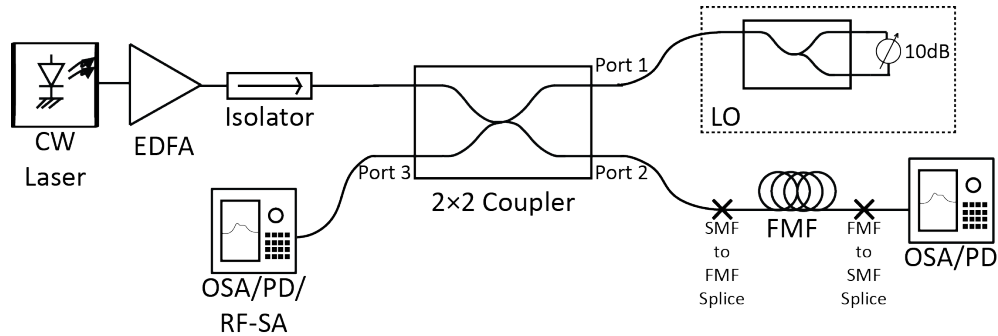


Figure 4.2: Experimental setup for experimental investigations into SBS in FMF. LO is used as a local oscillator for a heterodyne technique explained in the text while port 3 of the  $2 \times 2$  coupler allows back-reflected power to be measured.

**Source:** A standard DFB laser was used to produce a continuous wave at 1555 nm, with a maximum output power of  $\sim 5\text{dBm}$ . The laser was used as the input source for an EDFA with a total gain of 27dBm with an optical isolator at its output to prevent unwanted reflections from the remainder of the system. This section of the experiment made up the optical source and was connected to the input of the optical coupler, as can be seen from Figure 4.2. The optical coupler used in the experiment was a standard  $2 \times 2$  fused coupler with 50% of the optical power going to each of the two output ports (labelled "Port 1" and "Port 2" in Figure 4.2), with an excess loss  $\sim 1\text{dB}$ . When measured at low power ( $<0\text{dBm}$ ), it was found that the extinction ratio between the output ports one and two had  $>50\text{dB}$  extinction with Port 3.

**Port 1:** At the output of port 1 a second coupler was used, where the two output ports

were connected to each other with a 10dB attenuator. This formed a loop mirror where the original signal is reflected, providing a local oscillator (labelled LO in Figure 4.2) for heterodyne detection at the PD of port 3. This LO forms a heterodyne method used to directly obtain the Brillouin gain spectral shape and is a derivative method of [107, 108].

**Port 2:** Consisted of a 20 km length of FMF (Fibre I in Table 4.1). This fibre was spliced on both ends to standard SMF leading to a SMF to FMF splice at the input to the 20 km and a FMF to SMF splice at the output. The alignment of the splice was adjusted for minimum loss through the splice using a 1550nm source that was connecterised with a single mode fibre and the power at the output of the FMF was monitored using a wide area detector while butt-coupling alignment of the input was made in the fusion splicer. Once spliced the fibre output was connected to a power monitor to recorded optical power after transmission through the fibre.

**Port 3:** Was used as the monitor port to measure reflected power through the  $2 \times 2$  coupler. The port was monitored with a variety of measurement equipment, including, an OSA, RF spectrum analyser and optical power meter.

#### 4.2.1 Results of SBS Investigations

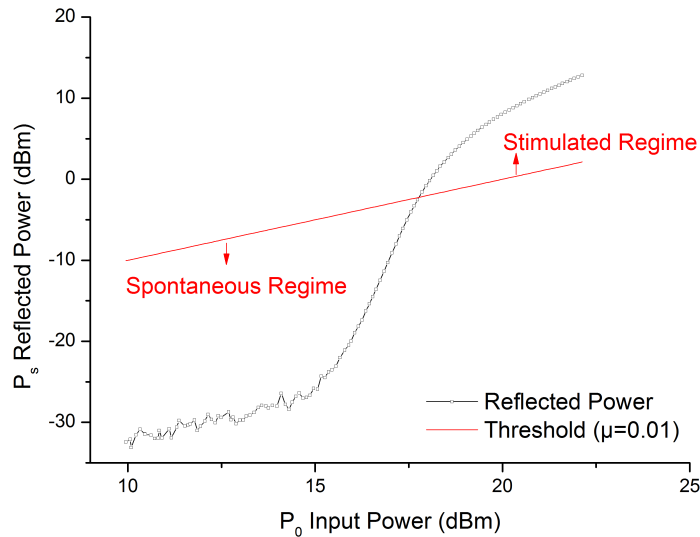


Figure 4.3: Result of SBS threshold measurement with experimental data measuring back-reflected power is shown in black while the condition for stimulated Brillouin scattering is shown in red for a value of  $\mu = 0.01$  based on Equation 4.1.

**SBS Threshold Measurements:** SBS threshold, the critical point where the Brillouin scattering noise becomes stimulated, is one of the main characterisation metrics used to quantify the effects of SBS. SBS power measurements are the simplest way to mea-

sure the SBS threshold. This is done by measuring the back-reflected power at the fibre input. The experimental result, of reflected power, is shown in Figure 4.3. This was done using the experimental setup shown in Figure 4.2 with the exclusion of the LO on port 1. Reflected power was measured using an optical detector placed at port 3. There are various definitions for SBS threshold, all with the common theme of reflected power, or Stokes power, being considered a fraction  $\mu$  of the total input power. At this point the process becomes "stimulated" as there is efficient conversion of energy between the input wave and the reflected Stokes wave. The SBS threshold can be expressed as:

$$P_s(0) = \mu P_0 \quad (4.1)$$

where  $P_s$  is the Stokes power as a fraction,  $\mu$ , of the input power,  $P_0$ . The measured data shown in Figure 4.3 shows a threshold at 17.8 dBm of input power for a 20 km length of FMF. The traditional formula to analytically estimate the threshold power of SBS in SMF is given in Equation 4.2 where  $x = 21$  and is the traditional approximation for SBS power threshold [23, 42, 108, 109, 110].

$$P_{th} = x \frac{A_{eff} \alpha}{g_B} \quad (4.2)$$

There are several distinctions that must be made before using such an approximate solution. First of all, when Smith [109] originally derived Equation 4.2 in 1972, fibre loss was considerably higher, leading to an assumption for the fibre loss ( $\alpha$ ) being 20 dB/km. This has lead to suggestions that these inaccuracies using Equation 4.2 can be compensated by adjusting the numerical factor ( $x = 21$ ) to a lower number [111, 112]. Secondly, the factor for effective mode area ( $A_{eff}$ ) refers to the acousto-optic effective area, even though values for optical effective area are commonly interchanged. Acousto-optic effective area can be calculated in a similar manor to optical effective area, where the acoustic guiding of the core region can be expressed in the form of the Helmholtz equation with a squared relationship with radius [113]. Furthermore Equation 4.2 only takes into account contributions from the fundamental acousto-optic mode. However the acousto-optic modes are more strongly guided and as a result contributions from a greater number of modes should be expected as the radius of the fibre is increased [113]. Here, to account for differences between the SBS threshold of SMF versus the new FMF that has been measured, a higher numerical correction factor of 4500 ( $x = 4500$ ) is suggested to further extend the use of Equation 4.2. The numerical factor is used to balance several aspects of the equation. Primarily, it is used here to account for the difference between the optical effective area and the acousto-optic effective area of several acoustic modes. The numerical factor ( $x = 4500$ ) serves a secondary role of accounting for a reduced loss ( $\alpha = 0.2$  dB/km) and any inaccuracy for the peak Brillouin gain factor  $g_B$ , which is assumed to be approximately that of standard SMF ( $g_B = 3 \times 10^{-9}$  cm/W). This assumption, that peak Brillouin gain

( $g_B$ ) will remain the same for SMF and FMF, is based on the fact that  $g_B$  is defined by material characteristics of the fibre such as refractive index and material density that are similar for both SMF and FMF <sup>1</sup>. This numerical factor may be adjusted slightly in the future to account for improvements in SMF to FMF coupling. One of the drawbacks of the experimental setup in Figure 4.2 is the SMF to FMF splice at the output of port 2, future systems without this drawback may require a revised numerical factor to account for the improved coupling.

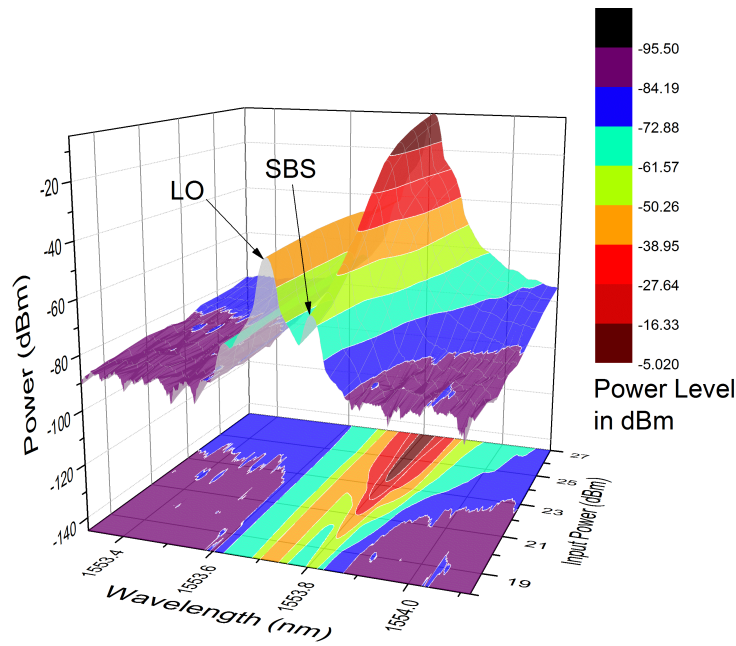


Figure 4.4: Surface plot showing all optical spectra of measured back-reflected power. Both the local oscillator (LO) seed pump and the SBS gain peak are labelled.

**SBS Gain Measurements:** To complement the threshold measurements, a series of SBS gain measurements were taken. An experiment to measure the SBS gain was carried out using the same experimental setup that was used for taking the SBS power measurements except with the inclusion of a local oscillator (see Figure 4.2) to allow the use of a heterodyne technique to directly measure the Brillouin gain spectrum. The input power was adjusted between 18 to 28 dBm (to remain above SBS threshold of 17.8 dBm) and the reflected power was measured on port 3 using an optical spectrum analyser. The results of this can be seen in Figure 4.4 where the LO and SBS gain peak can be clearly seen separated by 10.9 GHz. The 10.9 GHz separation corresponds to the Brillouin frequency shift and is  $\approx 11$  GHz in standard SMF [23]. Figure 4.4 also shows that as the input power increases so too does the gain of the SBS signal.

The gain of the SBS is more accurately represented in Figure 4.5 where the experi-

<sup>1</sup>  $g_B$  should not be confused with  $g_m$ , defined in Chapter 2, that refers to the Brillouin gain of the  $m^{th}$  mode and  $g_B$  refers to the peak of the total gain spectrum

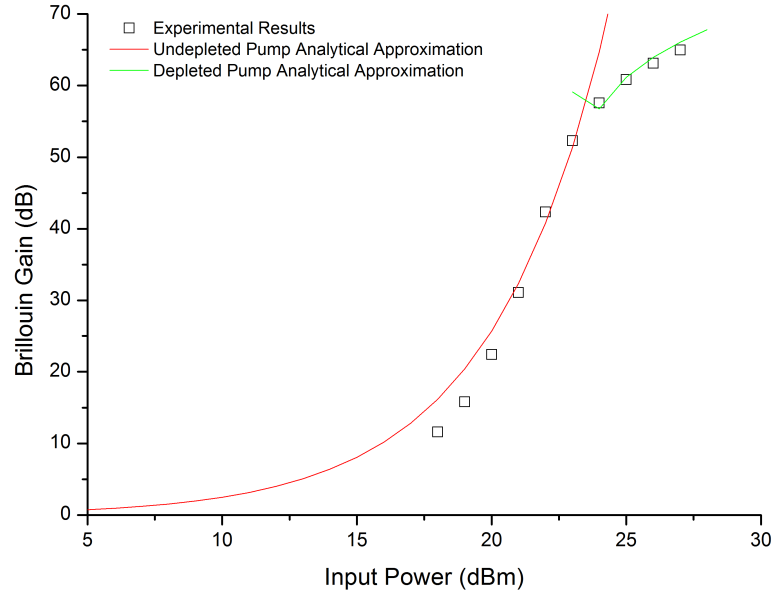


Figure 4.5: Measured SBS gain (black squares) compared against two analytical models for SBS in both the depleted (green) and undepleted (red) pump regime.

mentally measured Brillouin gain is plotted against an analytical model. By using the setup shown in Figure 4.2 the back-reflected power from the FMF to SMF splice acted as a Stokes seed power and was directly linked to the input power, this accounted for a slight increase for Stokes seed power as the input was increased, it is known that as this seed power is increased the gain saturates earlier, leading to a decrease in gain compared to cases with smaller seed power. This association with the seed power accounts for the slight deviation from the analytical models plotted in Figure 4.5. The two models plotted in Figure 4.5 account for SBS gain in the undepleted (red trace) and depleted (green trace) pump regimes respectively. The undepleted pump approximation (UPA) is given by the analytical expression [42]

$$G_{amp}^{UPA} = \exp \left[ -\alpha L + u \frac{1 - e^{-\alpha L}}{\alpha L} \right] \quad (4.3)$$

where  $L$  is the fibre length in meters and  $\alpha$  is the fibre loss in watts per meter and  $u$  is a simplification to express

$$u = \gamma_B P_0 L \quad (4.4)$$

where  $\gamma_B = g_B / A_{eff}$  and  $g_B$  and  $A_{eff}$  are the *acoustic* mode peak Brillouin gain and effective area respectively.

In the case of the depleted pump, a closed-form approximate analytical expression for

Brillouin gain in the depleted pump region is taken from [42]

$$G_{amp}^{DPA} = \frac{P_0}{P_{seed}} \left( 1 - \frac{\Lambda + \ln[\Lambda(1 - \Lambda/u)]}{u} \right) e^{-\alpha L} \quad (4.5)$$

where  $u$  is defined in Equation 4.4,  $\Lambda = -\ln[\gamma_B P_{seed} L]$  and  $P_{seed}$  is the Stokes seed power.

These analytical expressions are useful tools to compare measured results to what one might expect and to avoid laborious numerical calculations to derive the result from coupled ordinary differential equations describing SBS. The match to numerical data was achieved for both the depleted and undepleted pump approximations with a Stokes seed power of  $P_{seed} = -42$  dBm (corresponding to less than 0.001% reflected power from the splice to SMF at the output of the FMF) and a value for  $\gamma_B = 0.003 \text{ m}^{-1} \text{ W}^{-1}$ . This value for  $\gamma_B$  is considerably smaller than values for standard SMF ( $\approx 0.14 \text{ m}^{-1} \text{ W}^{-1}$ ), this is due to relationship of the acousto-optic effective area with  $\gamma_B$ . The acousto-optic effective area for FMF appears to be much larger than that of SMF, as one might expect with FMF having a larger optical effective area allowing it to support a greater number of both optical and acoustic modes. The gain measurements shown here indicate that standard analytical approaches of assessing SBS gain in SMF can be used for modelling the behaviour of FMF once the effect of having a larger acousto-optic effective area is taken into consideration.

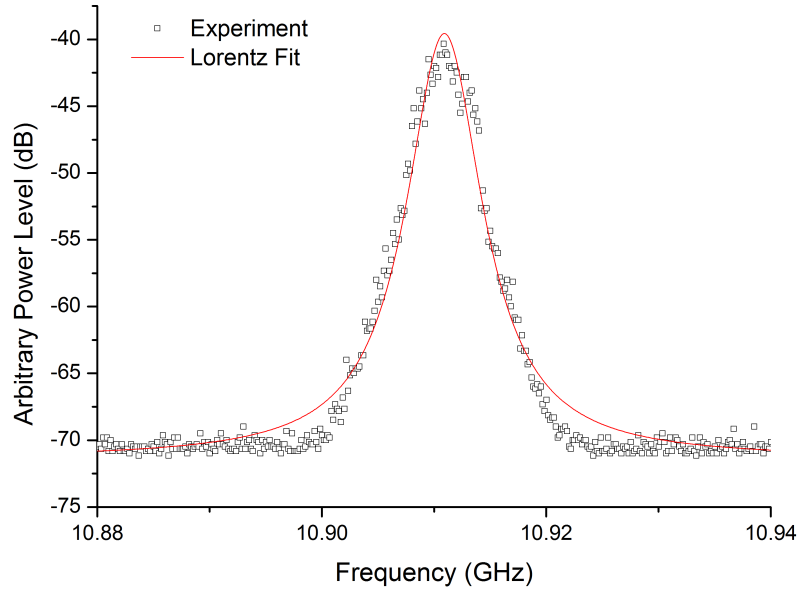


Figure 4.6: Measured RF spectrum of SBS gain (squares) with Lorentzian fit (red).

Finally, Figure 4.6 shows the RF spectrum of the SBS signal when measured on at port 3 using an RF spectrum analyser. The results are similar to that of standard SMF

with the SBS spectrum fitting a Lorentzian profile. From Figure 4.6 the spectral shift is 10.91 GHz and the gain bandwidth is  $\approx 30$  MHz both results are comparable to the expected value for standard SMF and this is due to the frequency shift being dependant on the material being used to propagate the signal as given in Equation 4.6.

$$\nu_B = \frac{2n\nu_A}{\lambda_p} \quad (4.6)$$

where  $n$  is the refractive index,  $\nu_B$  and  $\nu_A$  are the Brillouin frequency shift and the acoustic velocity in the medium respectively and  $\lambda_p$  is the pump wavelength. As SMF and FMF are made of silica and operate in the C-band, one would expect that the Brillouin frequency shift would be similar for both.

Though these experiments show that SBS can be generated in FMF and the threshold is higher than SMF, as one might expect, due to the higher effective area. The effect of SBS itself is largely the same in few-mode and single mode fibre due to the fibres having the same material composition. However, the assumption made for SMF where acoustic and optical effective are taken to be equal is no longer a valid assumption when dealing with FMF and further experimental work is required to investigate the relationship between the acoustic effective areas and the SBS threshold.

### 4.3 Investigations into SPM Effects

*"Only single-mode fibres can be used for long distance communications. Multimode fibres carry many modes of different phase and group velocities. The difference in group velocities of the different modes causes spreading of the temporal envelopes of the individual pulse-excited modes and thus cannot maintain high bit-rate pulse streams (short pulses) over large distances (several kilometres)."*

Hermann A. Haus

The above quote encapsulates the challenges that face any new fibre system that utilises multi-mode fibres. What Hermann Haus is referring to [114] are the effects of dispersion and self-phase modulation (SPM). These effects are detrimental to high bit-rate, long distance systems due to their degrading effect on the shape of the optical pulses travelling through a length of optical fibre. However, they are effects that affect both SMF and multi-mode fibres. As a high intensity pulse propagates down a fibre the intensity of the pulse will induce a nonlinear refractive index. In turn, the phase of the propagating signal becomes modulated due to the nonlinear refractive index and this effect is known as self-phase modulation. As the phase modulation of the signal is a result of the signals own intensity the phase change can be explained by the expression,

$$\phi_{SPM} = \gamma \int_0^L P_0 dz \quad (4.7)$$

where  $\gamma$  is the nonlinear coefficient,  $L$  is the fibre length and  $P_0$  is the signal power.



When other fibre characteristics such as loss and dispersion are considered then pulse distortions in the temporal domain can occur. In a positive dispersion regime this can lead to detrimental pulse spreading. This has the potential to be complicated further by each mode in a multi mode fibre having different group delays and thus SPM will affect temporal pulses to varying degrees, along with other contributing effects such as mode coupling. Though the complexity of multiple modes exhibiting such effects has hampered interest in characterising such fibres (especially compared with the complexity of characterising SMF), FMF offers a tantalising midway point where characterising nonlinear effects in multiple modes is feasible to establish the viability of multi-mode fibre systems. The experiments here aim to do just that. Several experimental procedures were carried out to investigate the effect of SPM in FMF, the results are compared against multi-mode models to show where such models can be used as design aids and where such models should be avoided. The results are presented in chronological order to show how various techniques were improved and perfected.

#### 4.3.1 Initial Experimental Setup

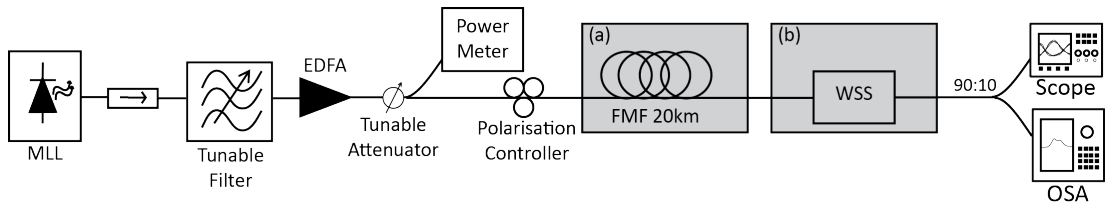


Figure 4.7: Experimental setup for investigating SPM using a SMF to FMF splice (a) where a frequency discriminator method is implemented using a WSS (b).

Figure 4.7 shows the optical setup that was used to assess the nonlinear pulse propagation in a 20 km length of FMF. The fibre in use (Fibre I in Table 4.1) had a 25  $\mu\text{m}$ -core diameter which supported four LP mode groups, with a maximum differential mode delay (DMD) of 2.95 ns/km, chromatic dispersion between 17.5 and 21.1 ps/nm/km, and a net loss of less than 10 dB including launch splice losses. To avoid pulse collisions due to the modal dispersion within the fibre, an actively mode locked laser (MLL) at 1551nm wavelength was used to launch  $\approx 23$  ps pulses at a 10 MHz repetition rate into the FMF. This was done by first isolating the MLL using an optical isolator to avoid any unwanted reflections. A tunable filter was used to spectrally limit the pulses generated by the MLL, this was done by setting the tunable bandwidth filter to 29 GHz (measured 3 dB bandwidth). An EDFA was then used in constant current mode (set to 0.64 A pump current) to amplify the signal before passing through a tunable attenuator. The tunable attenuator was used to control the power being launched into the fibre. At this point the launched pulses were characterised to include any additional distortions from the EDFA. This was done using the second-harmonic generation frequency-resolved optical gating (SHG-FROG) technique [115], where the

pulse duration after the EDFA was measured to have a temporal FWHM of 23.5 ps.

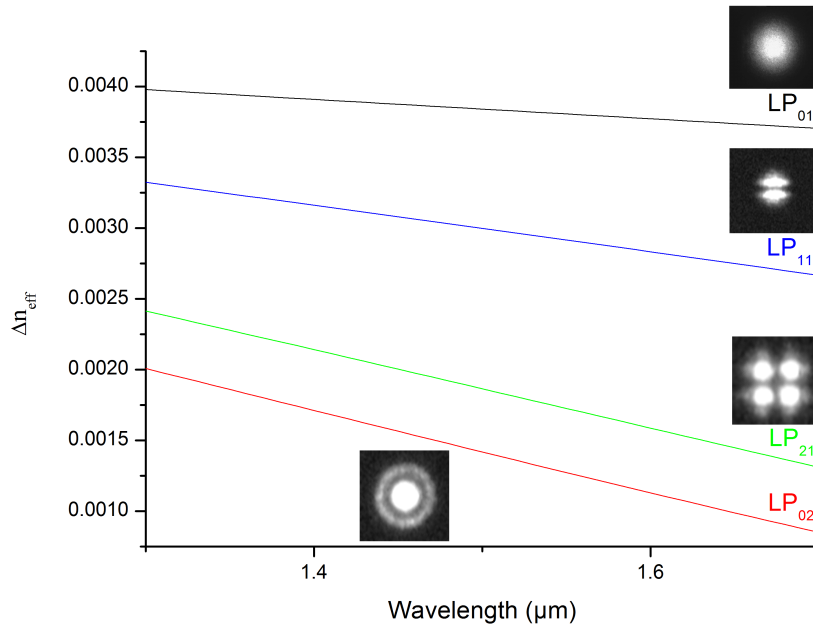


Figure 4.8: Effective index of four mode fibre in use including typical intensity profiles for each mode (insets), with fibre  $\Delta n_{eff}$  profiles provided by OFS [104].

Figure 4.8 shows the Effective Index Difference for each of the modes. This shows that the  $LP_{01}$  mode propagates in relative isolation from the other modes while (for example) the  $LP_{21}$  and  $LP_{02}$  have similar effective indexes indicating that one might expect these modes to have greater mode coupling between them. As can be seen from the inserts in Figure 4.8 the  $LP_{01}$  and  $LP_{02}$  modes both have a similar mode profile with an expected common excitation region close to centre launch. This was done by making a SMF to FMF fusion splice at both ends (this was done at point (a) in Figure 4.7), which aligned the claddings of both fibres. This launch, close to centre, ensured that excitation of  $LP_{11}$  and  $LP_{21}$  was negligible. Though this arrangement was effective for exciting only two modes at the input, it also contributed to the high insertion loss and resulted in an uncertainty over the relative input power ratio between the two modes.

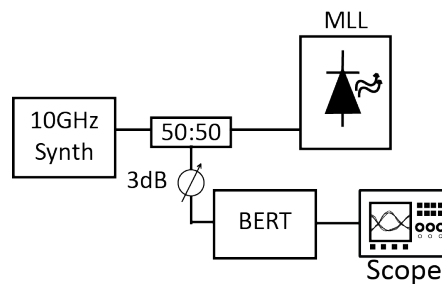


Figure 4.9: Electrical setup for synchronisation between the MLL and receiver oscilloscope.

The output of the FMF was monitored with an oscilloscope via a 50 GHz bandwidth photodetector. In order to synchronise the receiver with the MLL the electrical setup in Figure 4.9 was used. This was done using a 10 GHz frequency synthesiser that had output electrical power divided in two using a standard electrical splitter. Half the electrical power ( $\approx 8\text{dB}$ ) was used to lock the MLL, the second half of the electrical signal was fed to a bit error rate test-set (BERT). The BERT was used as a clock divider to divide the clock down to 10 MHz. This gave the scope at the receiver a trigger at 10 MHz that was synchronised to the 10 GHz source. Finally, in order to recover the temporal phase information, a wavelength selective switch (WSS, Figure 4.7(b)) was used as a frequency discriminator.

### 4.3.2 Phase Measurements Using a Frequency Discriminator Technique

There are several different ways to implement a frequency discriminator [116, 117, 118, 119]. In this case it was employed to measure the chirp of the optical pulses both before and after propagating through the FMF. The chirp of the pulse is the instantaneous frequency expressed as

$$\Delta\nu(t) = \frac{1}{2\pi} \frac{d}{dt} \phi(t) \quad (4.8)$$

where  $\phi(t)$  is related to the optical field of a modulated light source through the well known expression [23, 117]

$$E(t) = \sqrt{I(t)} e^{i[\omega_0 t + \phi(t)]} \quad (4.9)$$

where  $I(t)$  is the intensity,  $i$  denotes the complex number  $\sqrt{-1}$  and  $\nu_0$  the central frequency. Utilising the Fourier transform relationship

$$\omega E(\omega) \longleftrightarrow i \frac{dE(t)}{dt} \quad (4.10)$$

and assuming that the filter transfer function is linear to the frequency ( $\omega_p$ ) around the carrier frequency  $\omega_0$  it is possible to give the transform function. This was done by K. Sato et al [119] where they give the filter transfer function as

$$H(\omega_p) = T_0 [1 + c_1 (\omega_p - \omega_0)] \quad (4.11)$$

where  $T_0$  is the amplitude transmission and  $c_1$  is the differential coefficient.

The WSS was programmed to give a linear variation in attenuation as a function of frequency. This was done for both positive and negative frequency slopes,  $+c_1$  and  $-c_1$ . Then by carrying out a Fourier analysis it was possible to essentially differentiate

the temporal field where

$$\begin{aligned} P_+ &\cong T_0^2 P_0 \left(1 + 2c_1 \frac{d\phi}{dt}\right) \\ P_- &\cong T_0^2 P_0 \left(1 - 2c_1 \frac{d\phi}{dt}\right) \end{aligned} \quad (4.12)$$

as derived in [119] where  $P_+$  and  $P_-$  represent the optical power waveforms for the filtered pulses with positive and negative frequency filters as applied by the WSS. These optical waveforms were measured using a 50 GHz scope. From here it was possible to recover the chirp of the pulse by using the two useful parameters

$$\begin{aligned} P_A &= \frac{P_+ + P_-}{2} = T_0^2 P_0 \\ P_F &= \frac{P_+ - P_-}{2} = 2T_0^2 P_0 c_1 \frac{d\phi}{dt} \end{aligned} \quad (4.13)$$

where

$$\Delta\nu = \frac{1}{4\pi c_1} \frac{P_F}{P_A} \quad (4.14)$$

This enabled the amplitude and phase information of the pulse to be extracted in a similar way to that as shown by [118] and these measurements were taken with the help of Dr. Regan Watts [48]. Selected measurements were cross-calibrated using SHG-FROG technique and measurements were found to have good agreement with those that were taken using the frequency discriminator.

### 4.3.3 Initial Results

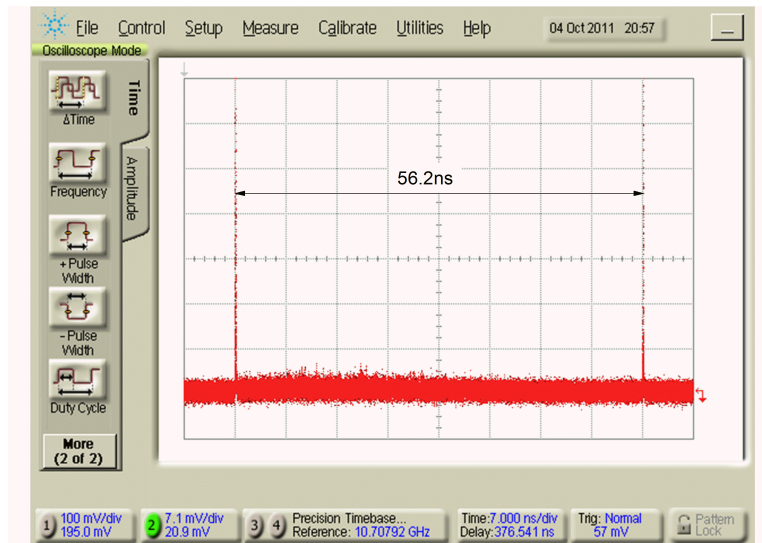


Figure 4.10: Screen capture showing temporally separated pulses corresponding to  $LP_{01}$ (left) and  $LP_{02}$ (right) modes after 20 km transmission

**Mode Excitation:** At low launch powers, two pulses were observed at the fibre output separated by 56.2 ns, in agreement with the calculated DMD between the  $LP_{01}$  and  $LP_{02}$ , taking into account a minimal mode coupling of  $\approx 5\%$ . The two pulses can be seen in Figure 4.10, where this pattern repeated every 100 ns coinciding with the pulse repetition rate of 10 MHz.

Full electric field information was reconstructed using the frequency discriminator technique for the input signal and for both modes at the output of the 20 km length of FMF as a function of the launched signal power. The results can be seen in Figures 4.11-4.13 for input and  $LP_{01}$  and  $LP_{02}$  modes respectively.

Note that the input polarisation was adjusted at the highest launch power to give the shortest observable pulse width and that no attempt was made to establish the ratio of launched powers between modes.

Figure 4.11 shows that the input pulse had negligible distortions as the launch power was increased. The pulse remained at  $\approx 23$  ps as the power was increased, while the phase across the width of the pulse remained close to zero, showing no distinguishable signs of chirp.

For the  $LP_{01}$  mode Figure 4.12(a) shows an interesting evolution of the temporal pulse shape as the power is increased. To begin the pulse is slightly broadened compared to the input pulse, as one would expect due to 20 km of dispersion. As the power is increased the pulse begins to narrow before the pulse splits at about 8.4 dBm average launch power ( $\approx 44.8$  dBm peak power) before narrowing at very high power to  $< 20$  ps. In the phase domain the shape across the pulse is largely quadratic at low powers, consistent with propagation being dominated by dispersion. As the temporal pulses split at high powers, the phase begins to depart from the quadratic distribution, due likely to SPM from the individual pulse peaks generated in the pulse splitting.

For the  $LP_{02}$  mode the pulse undergoes considerable distortion, as can be seen in Figure 4.13(a). Even at low powers the pulse begins to break-up, this can be due to several reasons but is likely due to a higher proportion of the input power being launch into the  $LP_{02}$  and will be discussed in greater detail in the sections to follow. While the phase plots show that the distribution is similar to the quadratic phase seen in the  $LP_{01}$  mode for the initial low power condition, at high powers the phase changes considerably. This change is again attributable to SPM from individual pulse peaks after the temporal pulse begins to split.

**Propagation Model:** In order to compare the experimental work to existing models that have been proposed for use with multi-mode fibres [120, 121, 122] a standard simulated model was coded as part of these investigations by Dr. Stylianos Sygletos. The model was based on the nonlinear Schrödinger equation for a propagating optical

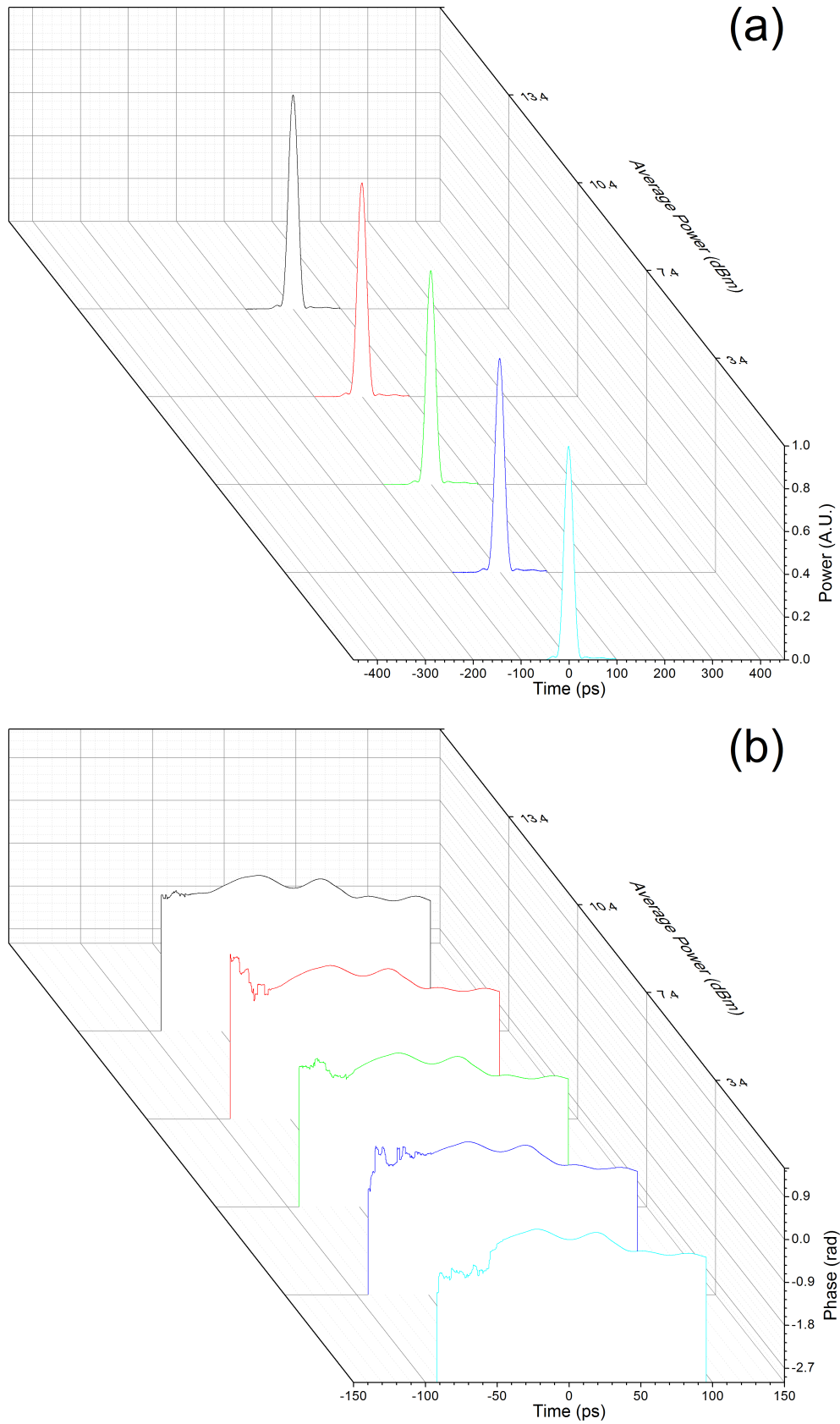


Figure 4.11: Measured (a) temporal and (b) phase information for optical pulse before propagating through fibre for increasing powers. The zero time corresponds to the central intensity of the pulse.

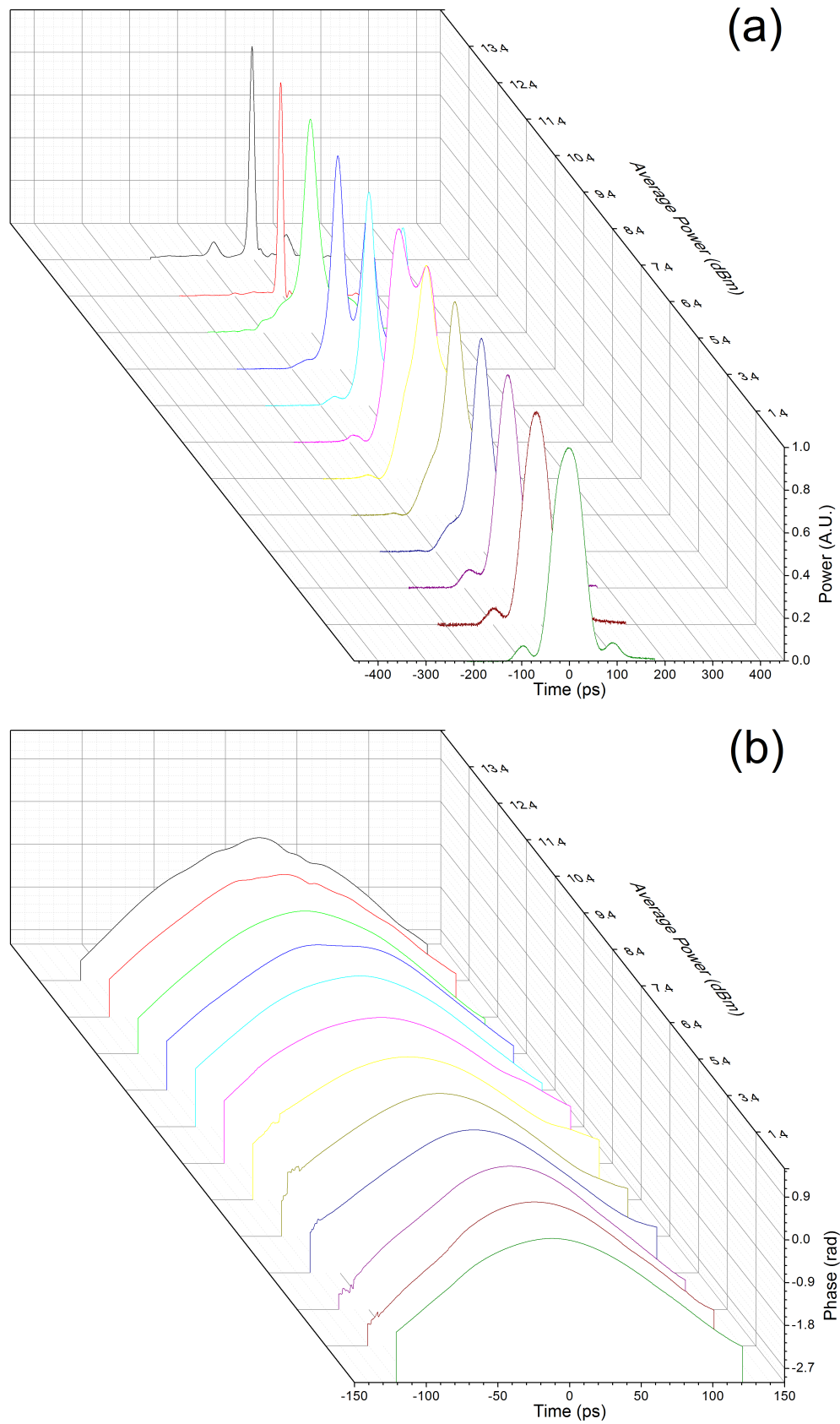


Figure 4.12: Measured (a) temporal and (b) phase information for optical pulse corresponding to the  $LP_{01}$  mode after 20 km transmission for increasing powers. The zero time corresponds to the central intensity of the pulse.

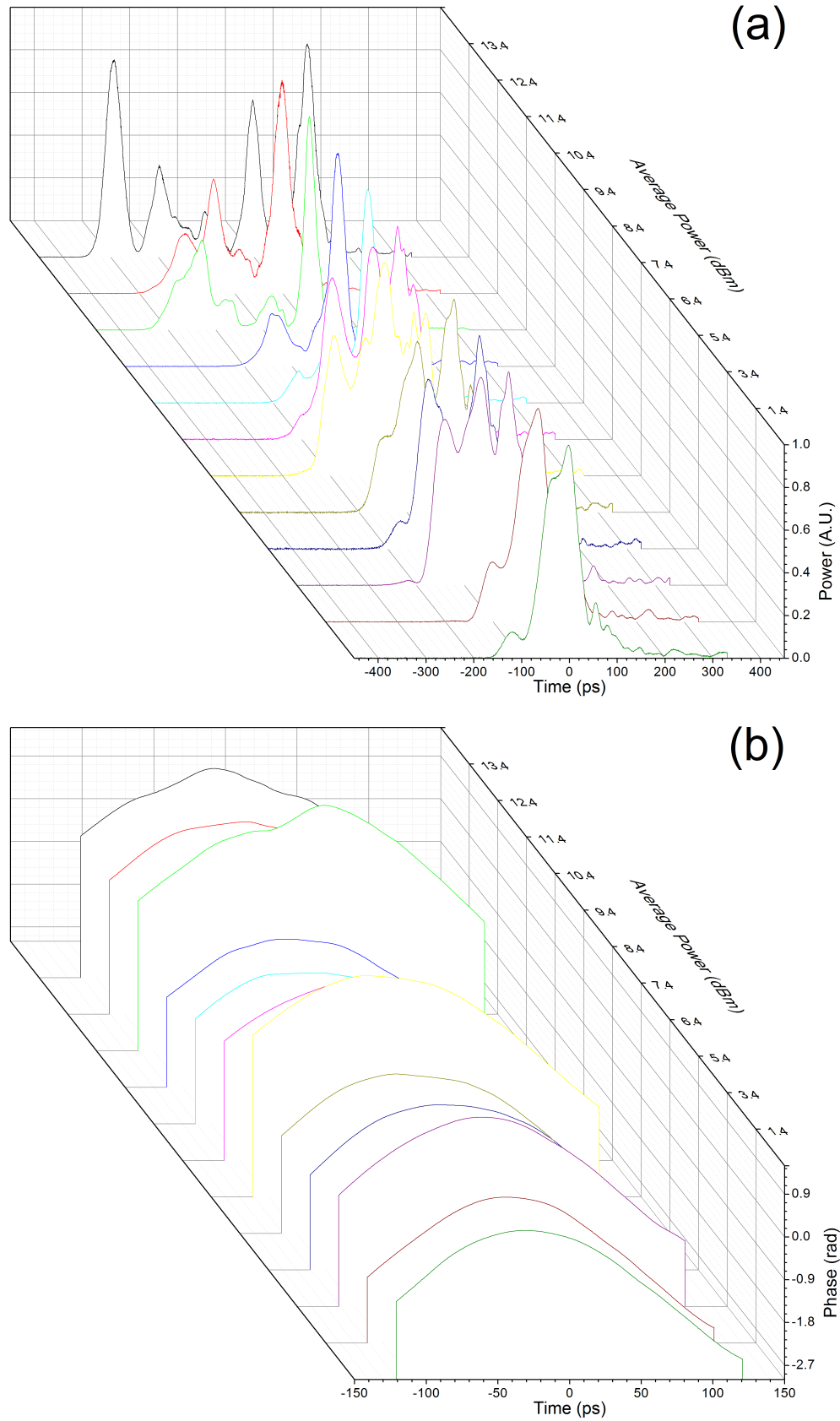


Figure 4.13: Measured (a) temporal and (b) phase information for optical pulse corresponding to the  $LP_{02}$  mode after 20 km transmission for increasing powers. The zero time corresponds to the central intensity of the pulse.



pulse

$$\frac{\delta E}{\delta z} = \underbrace{-\frac{\alpha}{2}E}_{\text{loss}} - \underbrace{\frac{i\beta''}{2}\frac{\delta^2 E}{\delta t^2}}_{\text{Dispersion}} + \underbrace{i\gamma E|E|^2}_{\chi''' \text{ nonlinearities}} \quad (4.15)$$

where the three terms to the right of Equation 4.15 refer the the loss, dispersion and nonlinearity respectively.  $E$  is the pulse amplitude and  $|E|^2$  the optical power,  $\gamma$  the nonlinear parameter,  $\alpha$  fibre loss and  $\beta''$  the GVD parameter. Equation 4.15 was solved using a split-step Fourier method where the FMF is modelled with SPM followed by dispersion, as it would be in an SMF case [47, 123], with the addition of linear mode coupling, where bandwidth limitations of the experimental components were considered and equal power in each mode was assumed. The model was then seeded with the experimentally measured input pulse data and the simulated output pulses for both LP<sub>01</sub> and LP<sub>02</sub> modes, shown by the red dotted line in Figure 4.14.

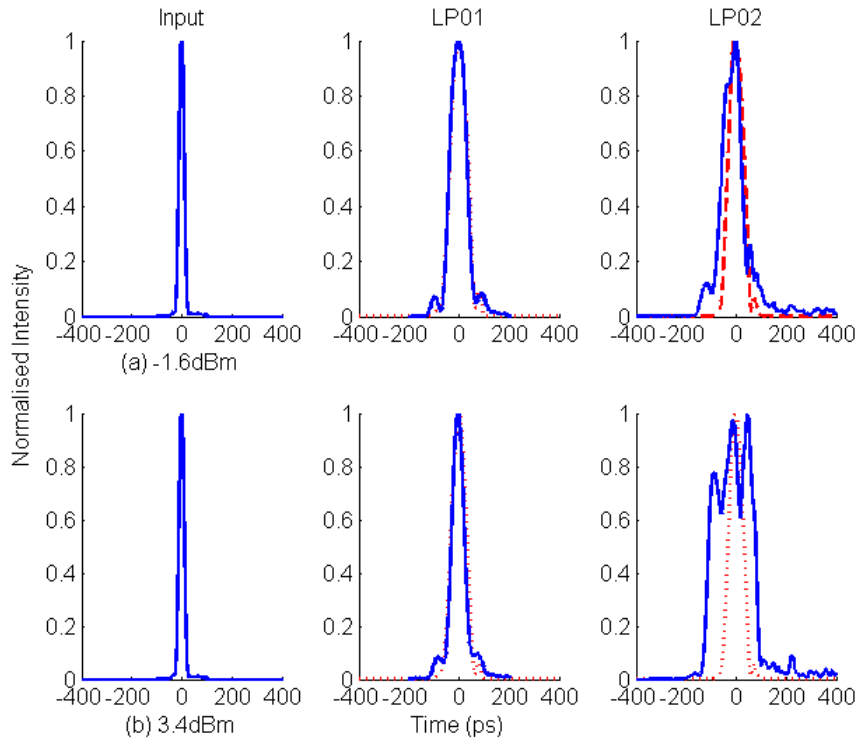


Figure 4.14: Temporal pulse profiles for experimental (blue) and model simulations (red) assuming equal power coupled between modes. Each column refers to input, LP<sub>01</sub> and LP<sub>02</sub> outputs with each row corresponding to low power and high power launch conditions.

Figure 4.14 shows examples of pulse temporal profiles for two different powers, the top row corresponds to low power case and the bottom row for high power. Each column in the figure corresponds to the input, LP<sub>01</sub> and LP<sub>02</sub> pulse respectively. As can be seen from Figure 4.14, the LP<sub>01</sub> closely matches the model at both (a) low and

(b) high powers, consistent with the validity of the approximations. The numerical model was used to predict the behaviour of the  $LP_{02}$  mode and was found to differ considerably from the experiments. This is likely due to an unbalanced ratio of powers between  $LP_{01}$  and  $LP_{02}$ .

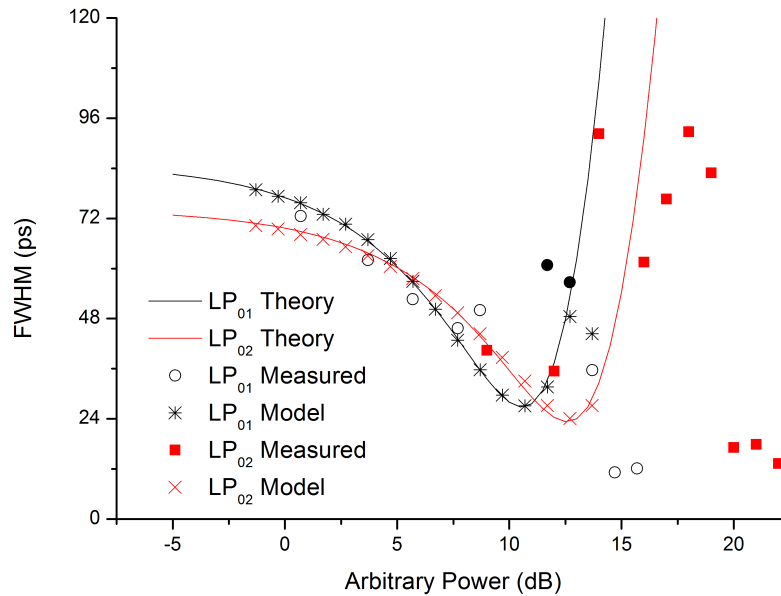


Figure 4.15: FWHM measurements for  $LP_{01}$  (black) and  $LP_{02}$  (red) modes. The measured results (circles and squares) are compared to a basic simulation model (asterisks and crosses) and a single-step split-step Fourier method (solid lines).

In order to understand this behaviour, the full-width at half-maximum (FWHM) of the output pulses were extracted and plotted in Figure 4.15 against the relative input powers per mode for each of the excited modes to estimate the ratio of power in each mode. The FWHM measurement was taken in favour of root mean squared (RMS) values in order to eliminate any effects due to random mode coupling. Random mode coupling would increase the amplitude between temporally separated pulses and artificially increase the RMS values, FWHM values avoid this at the cost of reduced accuracy at very high power when the pulses have undergone significant break-up. In Figure 4.15 the experimental measurements of  $LP_{01}$  (circles) and  $LP_{02}$  (squares) are compared with FMF model simulations (crosses and asterisks respectively), and also with a one step split-step analysis [47] (solid black and red lines respectively). Here, the mode coupling gives dips in the output pulse width, and the position and amplitude of the dips are power dependent (see Figure 4.15). Whether this is a result of nonlinear mode coupling, or due to changes in the signal spectrum (wavelength dependent mode coupling) requires improved experimental technique to control the power in each mode.

In Figure 4.15, for  $LP_{01}$ , SPM clearly plays a role by narrowing the pulses as the power increases. As the power is increased further (over 10 dB), the nonlinearities induce pulse splitting, and the FWHM measurements begin to increase dramatically. Note that the two solid circle symbols in Figure 4.15 corresponds to pulse splitting for  $LP_{01}$ , and the FWHM shown in these two cases were obtained by measuring the FWHM of the overall pulse by measuring the sum of the two split pulses, considering an even power split. At very high powers, however, the pulse narrowing observed is possibly due to soliton-like effects.

The  $LP_{02}$  mode, in turn, also undergoes a similar pulse distortion as  $LP_{01}$ , with pulse splitting and broadening being much more pronounced in the experimental results (Figures 4.13, 4.14 and 4.15). This is likely due to a greater power coupling into the  $LP_{02}$  mode, which was estimated to be  $\approx 8$  dB higher than the  $LP_{01}$  mode. This mode coupling ratio is taken into account in Figure 4.15, the numerical predictions closely match the experiments with the pulses strongly affected by SPM. For arbitrary powers above 14 dB, the pulses were highly distorted, generating very scattered results around the predictions. This scattering is likely to be because of additional cross-mode coupling effects. For very high powers, however, where the experimental results are very far from the predictions, it is possible that other effects, such as solitons or interference between different degenerate modes, may be playing a role, especially as the measurements were particularly sensitive to polarisation.

#### 4.3.4 Improvements to the Experimental Setup for SPM Measurements

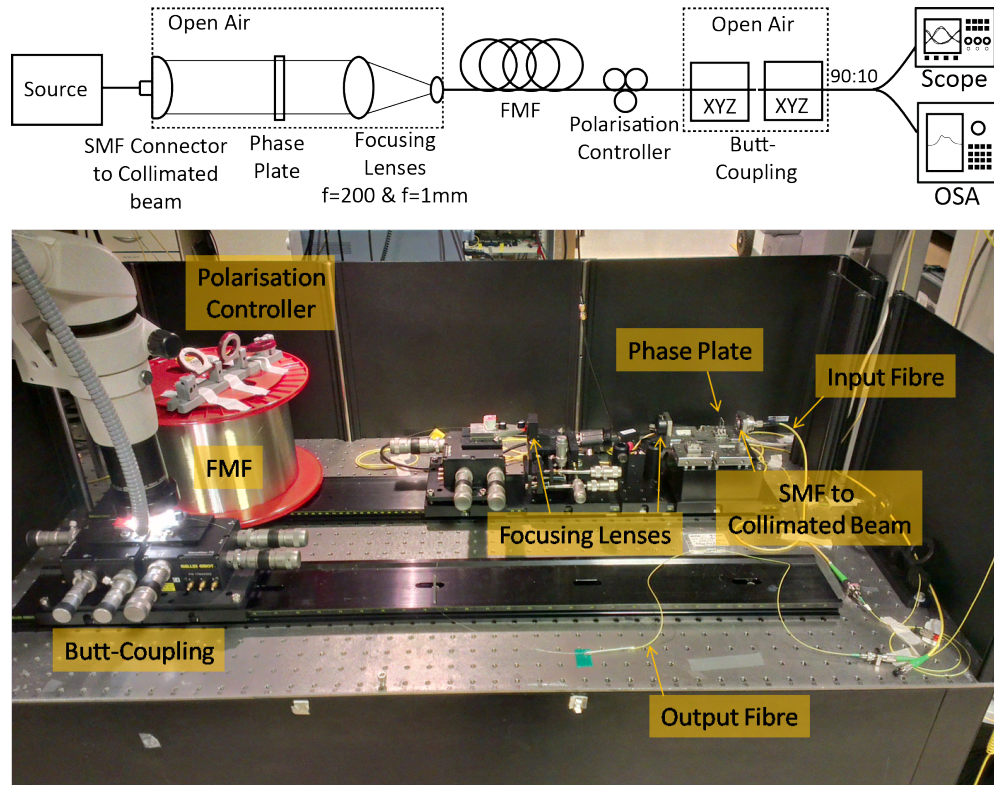


Figure 4.16: Schematic diagram (upper) and picture (lower) of improved experimental setup with mode interrogator.

Though the setup used in the previous section was useful in producing initial results on pulse distortions in FMF it was limited in several ways. When it came to designing the second generation experimental setup it was necessary to remove as many of the original limitations as possible. To that end the setup shown in Figure 4.16 was constructed. The basic principle is similar to the experimental setup used previously (see Figure 4.7) with the source consisting of the same MLL with 10 MHz repetition rate with the same filter and amplifier setup. The major improvement in this setup is the mode interrogator that allows pulses to be launched into individual modes by using free-space optics and an optical phase plate to couple the required mode into the fibre. The fibre in use was also changed to a 10 km long FMF that supports two LP modes with low DGD (Fibre II in Table 4.1). This fibre was selected as it reduces the complexity of isolating any nonlinear inter-mode effects by supporting just two LP modes, while the low DGD causes a greater interaction length that may increase crosstalk between modes so inter-mode effects may be studied.

Coupling into the fibre was achieved by using a series of free-space optics similar to that used to do mode multiplexing [97], where a standard polished flat connector is placed into an adapter that increases the beam waist to  $\approx 8$  mm before the beam is col-

limited. The collimated beam then passes through a phase plate (loss  $\approx 0.5$  dB), made by etching quartz with a pattern, to produce the mode of interest. In this case that was the  $LP_{11}$  mode, but several different plates could be fabricated for higher order modes. The  $LP_{01}$  mode can be produced by removing the phase plate and coupling directly into the fibre. At this point the beam is focused down using two lenses to couple into the FMF that has been cleaved to have flat interface perpendicular to the direction of the input signal. The entire input coupling optics had a loss  $\approx 2.6$  dB when launching the  $LP_{01}$  and a slightly higher loss of  $\approx 3$  dB when launching the  $LP_{11}$  mode, this was due to the added loss of the phase plate.

At the output the signal was coupled back into SMF by butt-coupling with the FMF using XYZ stages tuned to allow for maximum average power. This method had minimal loss ( $\approx 1$  dB) and enabled the observation of all the modes (temporally separated due to DGD) under linear conditions where the extinction ratio of the phase plate could be observed and under nonlinear conditions where nonlinear mode coupling and other inter-mode effects may be prevalent.

#### 4.3.5 Results Using Mode Interrogator Technique

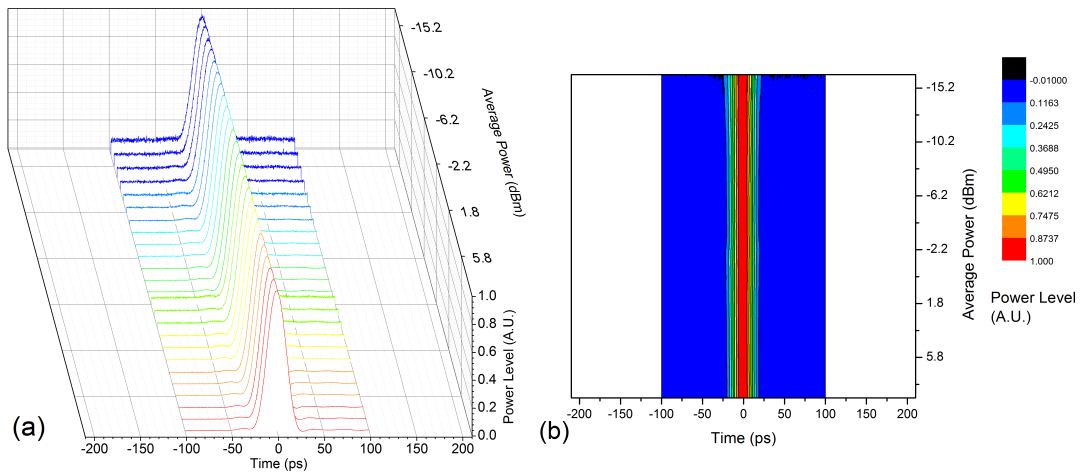


Figure 4.17: Experimentally measured pulse input data. (a) Waterfall plot and (b) contour plot of pulse evolution with increasing average launch power

The input pulse was measured directly at the fibre connector that connected into the open air system at the input. It had a maximum average power of  $\approx 8.8$  dBm and was measured for a range of powers between  $-15.2$  and  $8.8$  dBm in  $1$  dB steps. This was used as the power axis for each set of the following results (Figure 4.17 to 4.19). As can be seen from Figure 4.17 the pulse remained undistorted as power was increased and had the same pulse width as before ( $\approx 23$  ps).

The  $LP_{01}$  mode is the fundamental mode in the fibre and as a result has the lowest

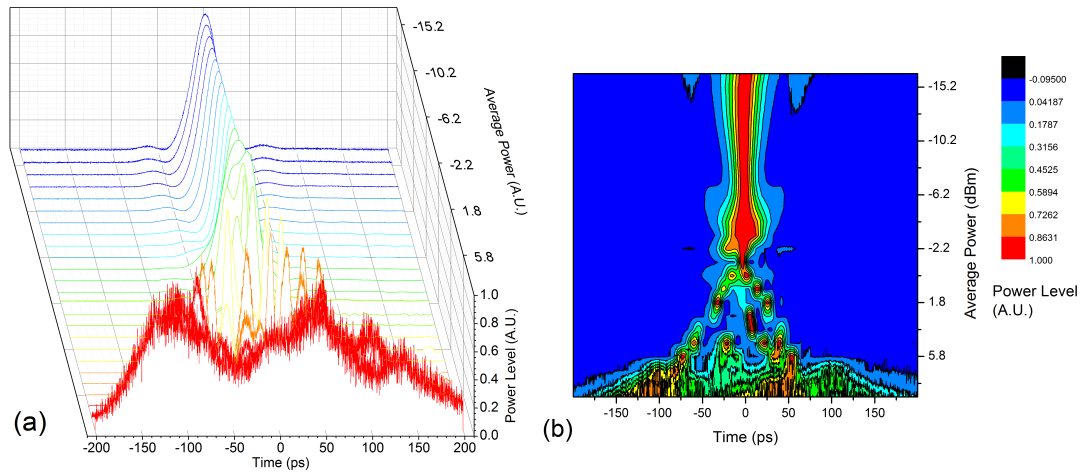


Figure 4.18: Experimentally measured pulse data for LP<sub>01</sub>. (a) Waterfall plot and (b) contour plot of pulse evolution with increasing average launch power

propagation loss. In this case, LP<sub>01</sub> had all of the signal power with negligible power on the LP<sub>11</sub> mode. The coupling lenses had  $\approx 2.6$  dB loss and thus the input range of powers was between 6.2 dBm and  $-17.8$  dBm. As can be seen from Figure 4.18 the pulse is relatively undistorted at low launch powers but as power increases the pulse narrows, splits and recombines in a similar way to the LP<sub>01</sub> mode of the four mode fibre. As the power is increased even further the pulse is destroyed. This is very similar to dispersion and SPM effects that are observed in SMF [23, 124, 125, 126].

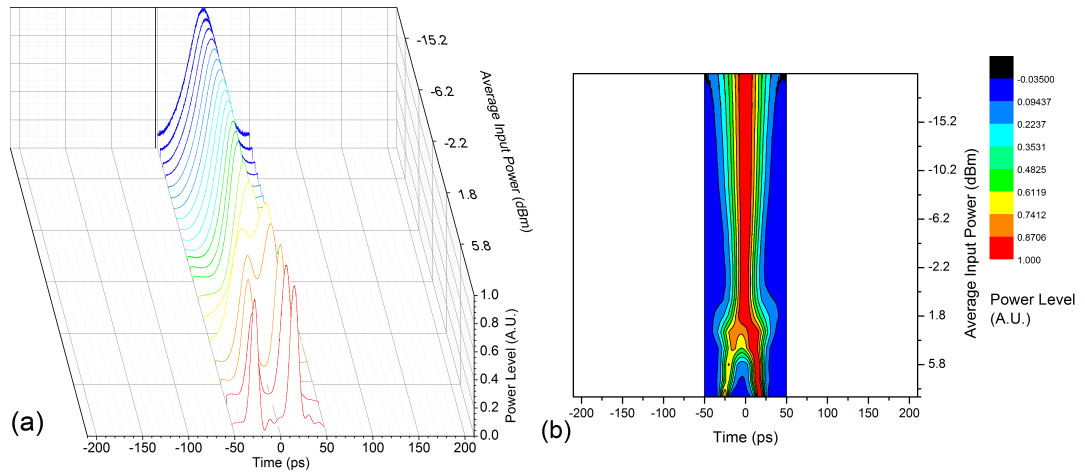


Figure 4.19: Experimentally measured pulse data for LP<sub>11</sub>. (a) Waterfall plot and (b) contour plot of pulse evolution with increasing average launch power.

In order to launch the LP<sub>11</sub> mode a phase plate was placed in the launch optics. The phase plate itself had very little loss ( $\approx 0.5$  dB) but the average power at the output of the system, after tuning to maximum average power, had an extra loss of  $\approx 10$  dB, this excess loss is due, in part to the higher loss of the LP<sub>11</sub> mode and excess loss due to



coupling back into SMF before the pulse is measured in the scope. Due to the added loss of the phase plate the range of powers was between 5.7 dBm and  $-18.3$  dBm. The input pulse was recovered and again was undistorted at low power. At high powers the pulse did split and became highly distorted. The pulse did not become as distorted as the  $LP_{01}$  pulse and this is likely due to the higher attenuation of the  $LP_{11}$  mode.

**Comparison to model:** The input model was again used to seed the simulated model of the fibre. The model remained exactly the same as before but the accurate launch power information from the experiment allowed a greater accuracy when attempting to model the experimental results. The model simulated the  $LP_{01}$  and  $LP_{11}$  modes for the same range of powers and the results are plotted in Figure 4.20. The results match quite closely the experimental measurements.

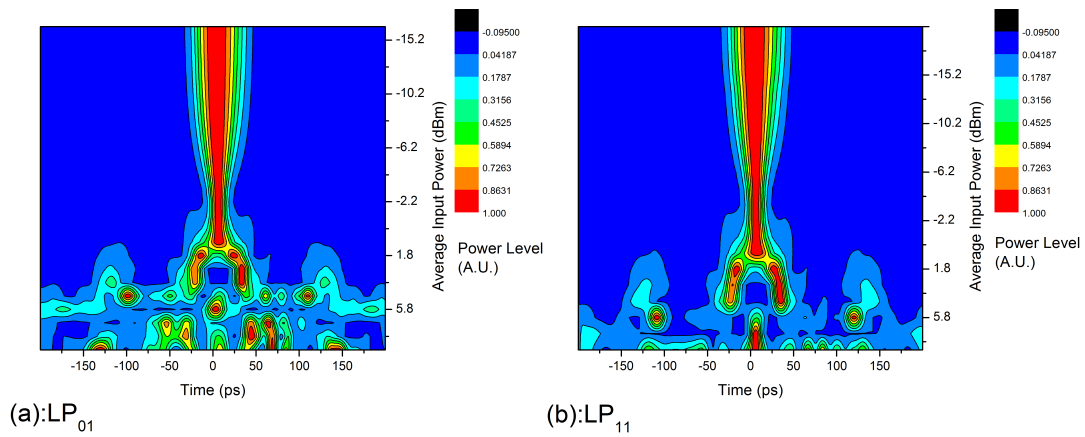


Figure 4.20: Simulated model data. (a) Contour plot of  $LP_{01}$  (b)  $LP_{11}$  pulse evolution with increasing average launch power.

In order to compare the results more accurately with the experimental data the FWHM of both measured and modelled data is shown in Figure 4.21. In this case, both modes show an overall trend that is reflected in both the experimental and modelled data. At low powers there is a slight offset between measured and modelled, this is likely due to a slightly lower dispersion value in the fibre compared to the quoted values from the manufacturer. This is supported by the measured DGD between  $LP_{01}$  and  $LP_{11}$  after 10 km being 1.6 ns, 20 ps (0.02 ps/km) less than the fibres supporting documentation. Another, less likely but possible, cause of the discrepancy could be due to the fibre being less than the 10 km quoted length.

At higher powers the deviations between simulated and measured are likely due to inaccuracies in the measuring of the FWHM where a slight difference in pulse amplitude may result in it being excluded from the measurement. At higher powers this leads the FWHM values to vary greatly as the pulse begins to rapidly spread in the temporal domain. However, both the modelled and experimental data show the same trend towards larger and larger pulse durations.

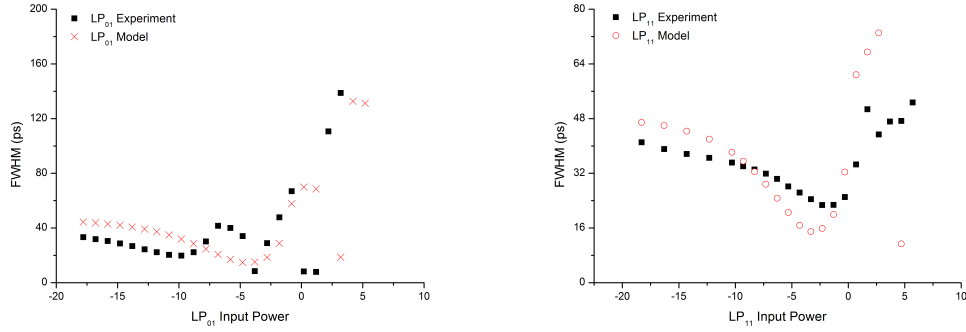


Figure 4.21: FWHM comparison of LP<sub>11</sub> (left) and LP<sub>11</sub> (right) for both experimentally measured (black squares) and simulated model data (red circles and crosses).

From these investigations it is clear that the effects of dispersion and SPM are present in individual modes of a FME. However, it has also been confirmed, experimentally, that current numerical models that are being used under the assumption that inter-mode effects are negligible when modelling SPM effects are indeed useful tools to show the general trend of performance, though for greater accuracy further terms (e.g. birefringence) should be included in numerical models.

## 4.4 Investigations into FWM Effects

Another important nonlinear effect is that of FWM. Similar to SPM the effect is a parametric process resulting from the nonlinear refractive index. FWM, as mentioned in Chapter 2, is due to optical signals at two or three separate frequencies beating together to produce a new frequency component. The relative strength of these beat signals is determined by the amount of velocity matching between all signals that are now present. Another way of viewing this transfer of energy is to think of the optical signal all travelling down paths in the fibre, if the group velocity of one signal is matched with that of another signal then there is a higher likelihood that energy transfer will take place. This condition is expressed mathematically, for SMF, as

$$\frac{2\pi\Delta\nu^2 D\lambda_p^2 L}{c} \ll 1 \quad (4.16)$$

where  $\Delta\nu$  is the frequency spacing between co-propagating signals,  $D$  the dispersion,  $\lambda_p$  is the centre wavelength and  $L$  is the length of the fibre.

We consider a moving frame of reference where the effect from the first term (phase velocity, denoted as  $\beta'$ ) of the Taylor expansion series for  $\beta$  (as covered in Chapter 2) cancels at the frequency about which the expansion is performed ( $\omega_0$ ) and the main contributing terms are  $\beta'$  and  $\beta''$  (where for single mode fibre the main contributor is



from  $\beta''$  (group velocity dispersion) and thus Equation 4.16 is accurate for the SMF case). For multi mode fibres the  $\beta'$  (group velocity) terms are different for each mode and thus the  $\beta'$  and  $\beta''$  terms contribute. Therefore, as fibre length increases the likelihood of velocity matching increases where you will get velocity matching between modes where the conservation of momentum is satisfied by matching  $\beta' + \omega\beta''$  for two modes. Inter-mode FWM can be avoided by having GVD that is locally high in each length of fibre. However, multi-mode fibre systems employ advanced MIMO DSP to recover transmitted data from separate modes. In mode multiplexed systems this requires the DSP buffer to be large enough to handle the delay for signals arriving from separate modes. This means that to reduce DSP complexity the dispersion, particularly the dispersion between modes (DMD), must be kept to a minimum. This raises interesting concerns over the likelihood of velocity matching, now with the added complexity of additional velocity matching between modes. Here new techniques are discussed that present a simple way to experimentally measure the effect of inter- and intra-mode FWM. This is then compared to current numerical tools for approximating FWM. Combining experimental and numerical approaches together should then allow for an accurate appraisal of FWM affecting total capacity limits, which will be discussed in Section 4.5.

#### 4.4.1 Experimental Technique for Measuring FWM in FMF

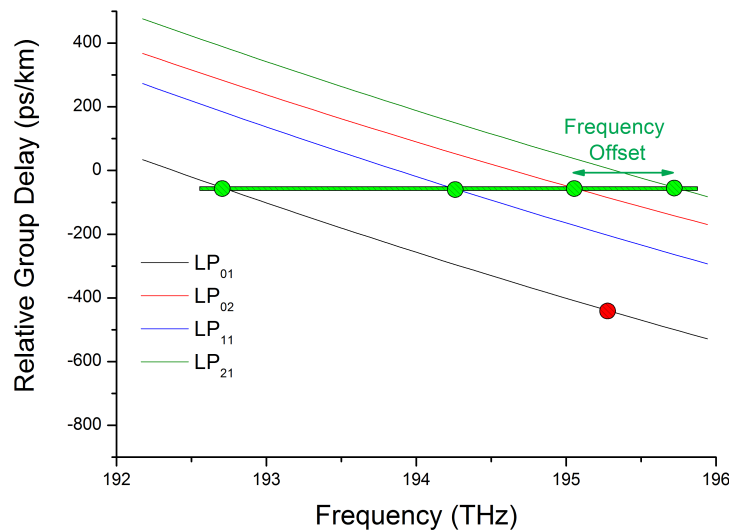


Figure 4.22: Relative group delay as a function of frequency for four modes in a FMF showing matched velocity between four modes (green circles) associated with higher inter-mode FWM effects, red circle indicates a condition where intra-mode FWM would dominate.

The major challenge to any measurement technique, that aims to measure FWM in

FMF, is to ensure that both intra- and inter-mode effects can be measured. It has been largely assumed [94, 97] that the effects of inter-mode FWM are negligible in FMF. However as Figure 4.22 illustrates, for four modes in a FMF, intra-mode FWM is possible under the same conditions as SMF but there is an added complexity of inter-mode FWM. Due to the relative delay between modes velocity matching between several modes is possible. In some cases this can be extreme, as shown in Figure 4.22, where the green circles illustrate areas where all modes are velocity matched. For matching two modes, this is equivalent to  $\beta' + \omega\beta''$ , where  $\beta'$  corresponds to the propagation constant of one mode and  $\omega\beta''$  corresponds to the GVD of a second mode at a particular frequency offset. Group velocities require matching as shown in Figure 4.22 and this is consistent with experimental observations in the thesis and of several groups, including the work of [127, 128]. Conservation of energy is satisfied by the constraint ( $\omega_4 = \omega_1 + \omega_2 - \omega_3$ ) on the frequency of the generated FWM product. The effects of intra-mode FWM are still present in areas where inter-mode FWM is weak, this is highlighted by the red circle in Figure 4.22.

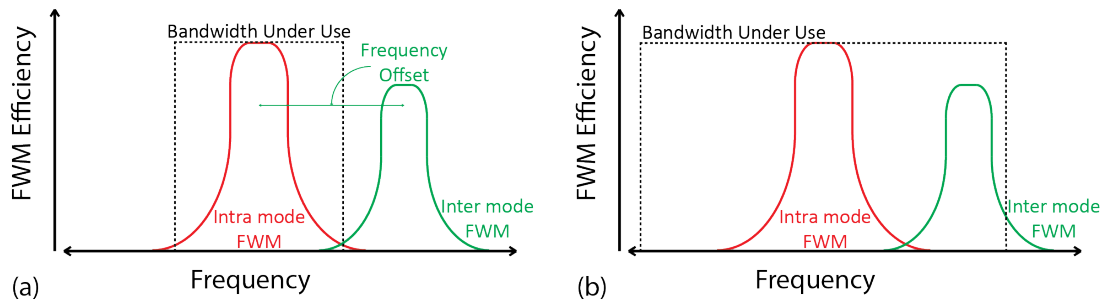


Figure 4.23: Conceptual illustration showing (a) the logarithmic bandwidth dependence with intra-mode (red) FWM effects and (b) the contribution of inter-mode FWM as bandwidth is increased, breaking the logarithmic bandwidth dependence.

The goal for FMF systems is to fill the available spectrum to increase the overall information capacity. This means that any FMF solution will have to be able to support broadband and highly dense WDM channels. For sufficiently broadband WDM systems, inter-mode phase matching is possible [129] and is illustrated conceptually in Figure 4.23 showing how the effect of inter-mode FWM is increased with wider bandwidth signals. This has been observed experimentally for both cross phase modulation using isolated pulses [127] and four wave mixing using continuous wave signals [128]. However, whereas these experiments confirm the presence of the inter-mode phenomena, quantification of their impact is still lacking.

The measurement technique used here confirms the logarithmic bandwidth dependence of FWM in a FMF and enables the relative magnitude of intra- and inter-mode FWM to be measured through a simple setup based on FWM between blocks of amplified spontaneous emission (ASE), which resemble closely spaced WDM signals after a few dispersion lengths [130].

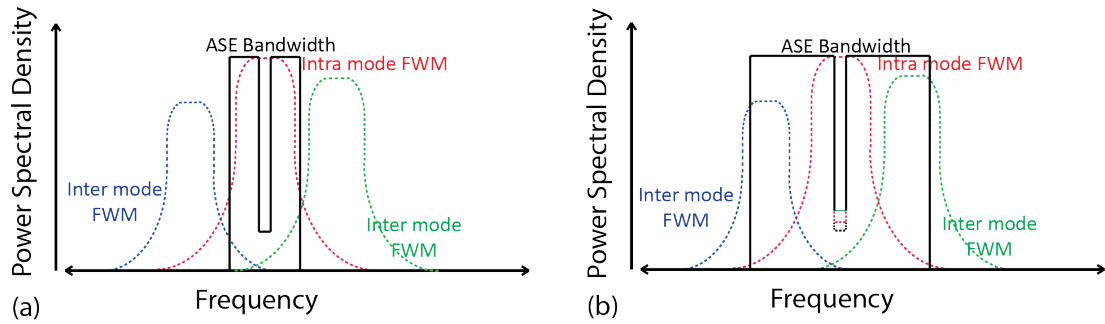


Figure 4.24: Conceptual representation of measurement technique using filtered ASE (dashed black line) showing (a) intra-channel FWM (red) reducing central notch extinction ratio while for wider bandwidths (b) inter-mode FWM (dashed green) reduces the central notch extinction ratio even further.

Figure 4.24 conceptually illustrates how the measurement technique aims to measure the relative strength of intra- and inter-mode FWM by simple filter profiling of an amplified ASE source where the centre frequency is notched with a narrow bandstop filter. The notch is kept at a fixed bandwidth while the total ASE bandwidth is increased (moving from Figure 4.24(a) to (b)). As the bandwidth is increased the extinction ratio of the central notch will begin to reduce due to a rising noise floor due to FWM from random phase matching in the ASE spectrum. This reduction in extinction ratio is a measure of the FWM efficiency which will increase logarithmically for intra-mode FWM as bandwidth is increased. However, as the bandwidth is increased even further (Figure 4.24(b)) inter-mode phase matching will cause a sudden step in the logarithmic dependence. This sudden increase in inter-mode FWM is manifested in a sudden decrease in the central notch extinction ratio.

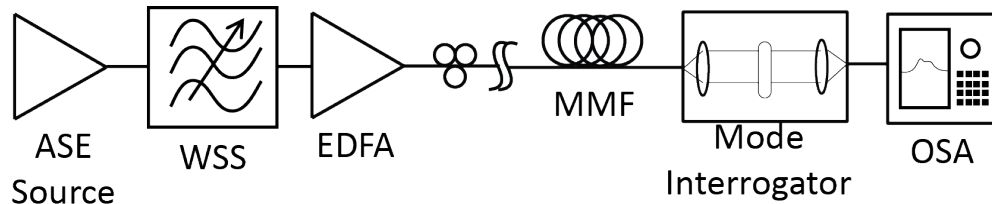


Figure 4.25: Schematic diagram of experimental set up (lenses and positioning stages at the ends of few mode fibre are omitted for clarity and are similar to that shown in Figure 4.16).

The experimental setup to carry out the experiment is shown in Figure 4.25. A 30 dB gain, gain-flattened erbium doped fibre amplifier was used as an ASE source, which was shaped into various rectangular blocks to represent specific wavelength bands of highly dispersed communications signals using a wavelength selective switch (WSS) programmed to have a central notch and tunable overall bandwidth (as discussed above). These blocks were amplified by a 38 dBm gain-flattened power amplifier. The output of the power amplifier was monitored using the OSA, while the WSS was

iteratively adjusted to ensure equal power spectral densities across the blocks of ASE. The amplifier current was adjusted, where necessary, to maintain constant spectral power. The centre of the ASE spectrum was attenuated using the WSS to leave a notch of 50 GHz bandwidth.

The high power ASE was launched into a few mode fibre designed to support four LP modes and to have a low differential mode delay at 1550 nm (fibre III in Table 4.1). Launch loss was estimated to be approximately 1.5 dB using an offset launch, adjusted to maximise mixing between the LP<sub>01</sub> and LP<sub>11</sub> modes. This was done by first maximising the average power through the system and then adjusting the offset launch while monitoring the OSA and tuning the coupling offset to the point where the extinction ratio of the central 50 GHz notch was at its minimum while ASE passband power remained high.

At the output the mode interrogator, consisting of coupling lenses, collimator and phase plate, had an excess loss of  $\approx 5$  dB. Outputs from each fibre mode were selected using a phase plate and the output spectrum was recorded using the same OSA, enabling the output power spectral density and the FWM power generated in the central notch to be established. This setup allowed the experiment to be performed in the manner conveyed in Figure 4.24 by using a broadband signal with a 50 GHz central notch where the total passband bandwidth of the ASE block was varied using the WSS. The FWM signal was monitored by observing the signal generated in the notch. This technique was used to show the logarithmic scaling with signal bandwidth and the relative impact of inter- and intra- mode FWM. In order to understand how FWM was related to how much the central notch filled required the use of a clear closed form expression for multi-mode FWM.

#### 4.4.2 FWM Numerical Model for FMF

In a parallel effort to the experimental work a novel analytical theory was developed by Prof. Andrew Ellis. The work builds on the work of [23, 51], and others to derive a closed form expression for the nonlinear noise power spectral density which would be generated in a FMF. Here that expression is discussed to allow an accurate comparison to the experimentally measured data.

For a signal with a rectangular spectrum (OFDM or Nyquist WDM super channel) in each interacting mode the integral of each FWM efficiency sums to an overall efficiency parameter  $\eta_{ijkn}$  (nonlinear power scale) of:

$$\eta_{ijkn} = \frac{\xi_{ijkn} \omega_0^2 n_2^2 N_s}{A_{ijkn}^2 c^2 \pi \alpha |\beta''|} \left[ \ln \left( \frac{B^2 + 2B\Delta f_{ijkn}}{2f_w^2} \right) + s \ln \left( s \frac{B^2 - 2B\Delta f_{ijkn}}{2f_w^2} \right) \right]$$

$$s = \text{Sign}(B - |2\Delta f_{ijkn}|) \quad f_w = \sqrt{\frac{\alpha}{4\pi^2 \beta''}} \quad (4.17)$$

where  $\Delta f_{ijkn}$  represents the velocity matched frequency offset,  $A_{ijkn}$  the effective area overlap of the interaction,  $\alpha$  is fibre loss,  $\beta''$  is group velocity dispersion,  $\omega_0$  carrier frequency,  $n_2$  the nonlinear refractive index,  $N_s$  number of spans in the link,  $c$  is the speed of light,  $B$  signal bandwidth and  $\xi_{ijkn} < 1$  the impact of mode averaging [47, 131]. In all the work presented here it is assumed that  $\xi_{ijkn} = 2/3$  for degenerate modes. This closed form analytical expression allows the FWM power generated in mode  $i$  originating from signals propagating in modes  $j, k$  and  $l$  to be calculated by taking the product of this nonlinear efficiency  $\eta_{ijkn}$  and the signal power spectral density, of each mode. Direct comparison of Equation 4.17 with [51] will reveal that the parameter  $h_e$  has been dropped since its value is approximately unity for all practical few-mode fibres. To simplify analysis the summed nonlinear efficiency for the  $i^{th}$  mode,  $a_i$ , is expressed as:

$$a_n = \sum_{i,j,k} \eta_{ijkn} \quad (4.18)$$

such that the total nonlinear power generated in the  $n^{th}$  mode is given by  $a_n P_i P_j P_k$  where  $P_i, j, k$  is the signal power spectral density in the appropriate mode.

The implications of Equation 4.17 are illustrated in Figure 4.26 for four different FMF designs with varying DMDs. Contours in Figure 4.26 represent potential values of  $\eta_{ijkn}$  as a function of readily calculated fibre parameters. The contour plots are plotted using  $10 \log_{10} \eta_{ijkn}$  and normalising to an effective area of  $50 \mu\text{m}^2$ . They show the impact of velocity matching induces a rapid drop in  $\eta_{ijkn}$  for a frequency offset of  $\pm 2.5$  THz (signified by the closely spaced contour lines). The frequency offset at which this rapid decay occurs is determined primarily by the signal bandwidth (5 THz in this case). Contour values also show the impact of the fibre effective area, and the weak FWM contributions arising from interactions which remain poorly velocity matched. The points on the contour plot correspond to actual calculated values for a given fibre (where a different fibre is presented in each case from (a) to (d) in Figure 4.26), the different colour points on each graph correspond to the nonlinear noise generated in each mode where the respective modes are described in the legend.

To calculate the total nonlinear noise power influencing a given mode, the amplitudes of the appropriate interactions must be summed (Equation 4.18). This is illustrated in Figure 4.27 for four separate fibre designs. The figure shows the nonlinear noise power generated at the centre of the WDM signal versus the WDM bandwidth for the four multi-mode fibres. In addition to the logarithmically increasing background

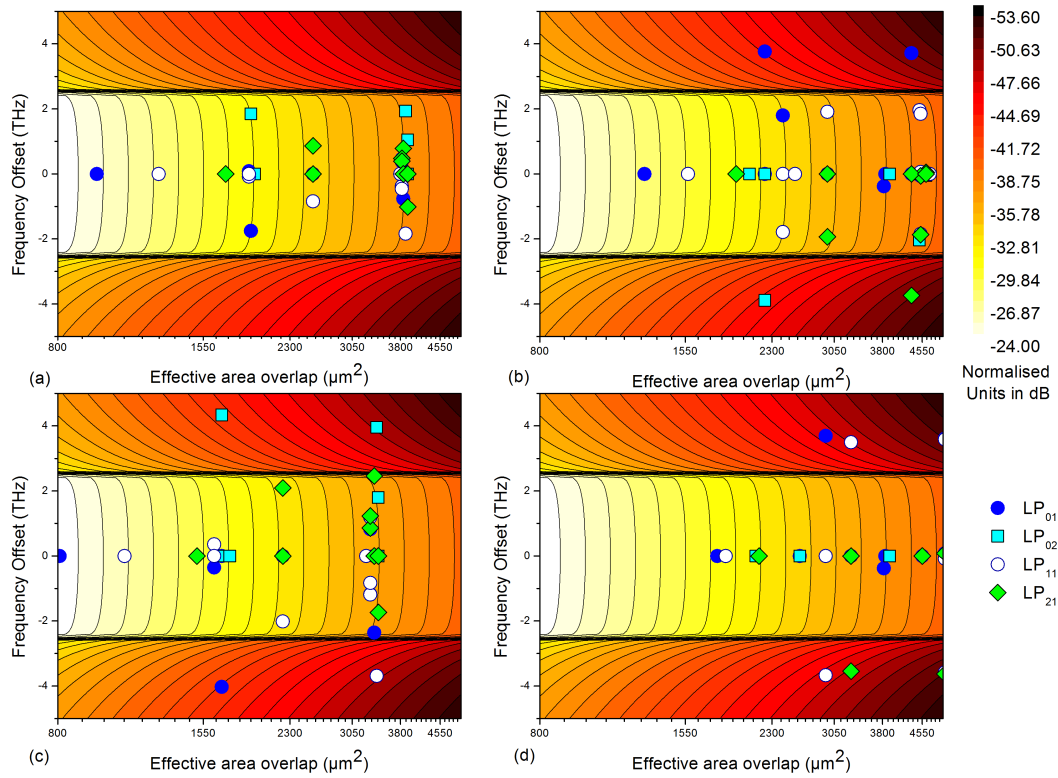


Figure 4.26: Contour plots of  $\eta_{ijkn}$  on a log scale as a function of effective area and frequency offset for a 5 THz WDM signal for four separate fibre designs with DGDs of (a) 102 ps/km (b) 210.8 ps/km (c) 223.2 ps/km and (d) 406.3 ps/km with the points on each graph corresponding to conditions where nonlinear noise is present for the various fibres.

expected for a SMF [132], a number of discontinuities, or steps, are apparent. With a larger number of discontinuities observed for the fibre with the lowest DMD giving a significant increase in the overall nonlinear power spectral density. With this model it should be possible to make a direct correlation between experimental measurements and theoretical predictions.

#### 4.4.3 Experimental Results Comparison with Multi-mode FWM Model

The input and output spectrum were recorded for a range of filter bandwidths reducing the total bandwidth from 3 THz in 50 GHz steps. This was done in two separate data sets,  $3 \rightarrow 1.5$  THz and  $2 \rightarrow 1$  THz. This was done to ensure a high power spectral density. By doing the measurements in a single step the power spectral density of the gain flattened EDFA signal would increase dramatically for narrow filter bandwidths, by taking the data in two separate sets this was avoided while allowing the opportunity to maximise power spectral density. The two sets overlapped for a range of 500 GHz and allowed the data to be stitched together accurately. The central 50 GHz notch was accurately measured on the OSA over a 200 GHz span. A typical measure-

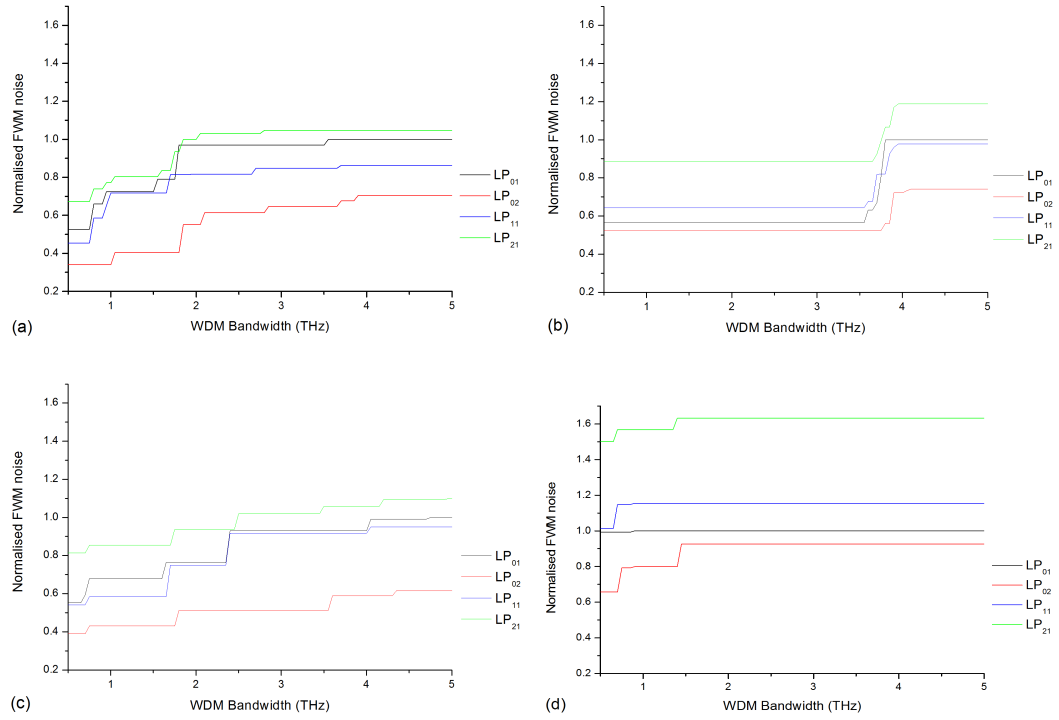
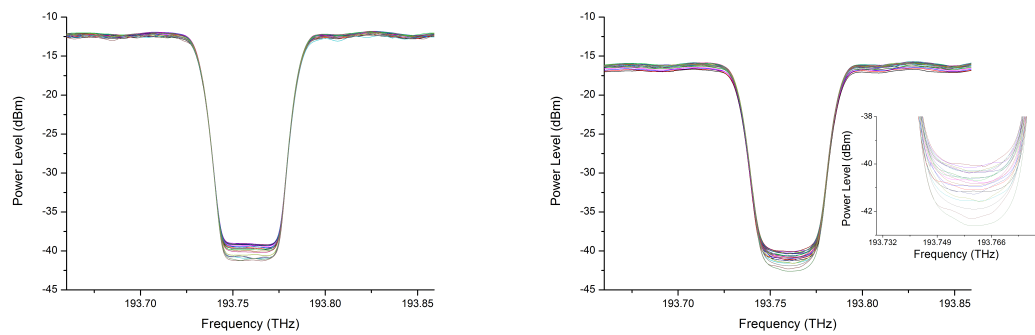


Figure 4.27: Summed FWM noise as a function of WDM bandwidth, normalised to the LP<sub>01</sub> mode, for four separate fibre designs with DGDs of (a) 102 ps/km (b) 210.8 ps/km (c) 223.2 ps/km and (d) 406.3 ps/km

ment at the input and output of the fibre, showing the change in extinction ratio, is plotted in Figure 4.28. The passband ripple on either side of the notch was measured at the fibre input and output and normalised so as not to affect measurements on the extinction ratio of the central notch.



with inset showing central notch with a higher scaling

Figure 4.28: Typical Spectrum measurement on central 50 GHz notch for a range of total bandwidths at (a) fibre input and (b) output of the fibre interrogating LP<sub>01</sub> mode

Figure 4.29 shows the measured FWM efficiency, calculated by dividing the output PSD cubed, measured in the central 50 GHz notch using an OSA (and induced by

FWM), by the cube of the input PSD calculated from the output PSD measured in the 200 GHz regions either side of the central 50 GHz notch and corrected for the fibre loss. The measurement was performed for both the  $LP_{01}$  and  $LP_{11}$  modes. Each mode was filtered at the output by using the mode interrogator. For the  $LP_{01}$  mode this was done by using SMF that was tightly wound. For the  $LP_{11}$  mode this was done using a phase plate (etched quartz) and a full set of measurements were taken in a single vertical orientation.

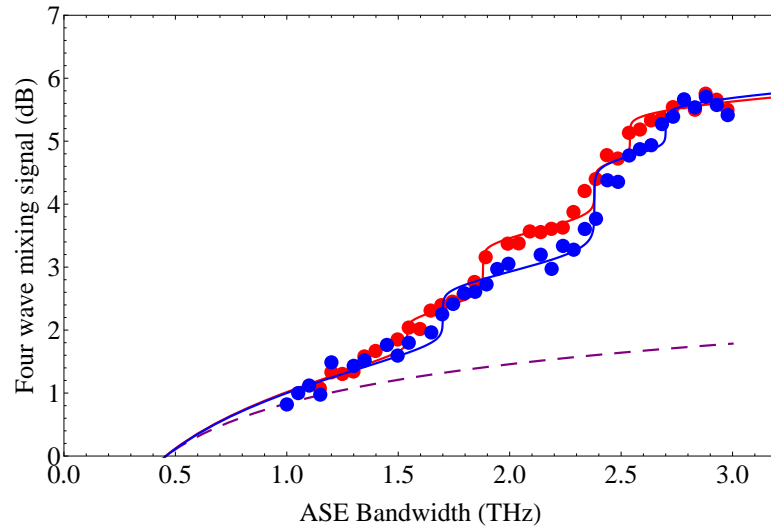


Figure 4.29: Comparison of experimental data (dots) to FWM model (lines) for  $LP_{01}$  (blue) and  $LP_{11}$  (red) modes. The dotted line indicates expected FWM signal neglecting inter-mode effects.

The resultant data was normalised to the efficiency obtained for a 1 GHz ASE bandwidth. The results show the expected logarithmic growth trend, punctuated by discrete steps corresponding to the onset of individual inter-mode interactions, in excellent agreement with theoretical predictions based on summing Equation 4.17 over all mode combinations. The fit shown was achieved for frequency matched offsets of 0.8, 0.9 and  $1.2 \pm 0.1$  THz ( $LP_{01}$ ) and 0.85, 1.2 and  $1.35 \pm 0.1$  THz ( $LP_{11}$ ). The fitting parameters suggest inter-mode interaction strengths of around 15 % of the intra-mode strength, representing effective areas around 2.5 times greater than the  $LP_{01}$  intra-mode effective area, which is consistent with the overlap integrals for a typical four mode fibre. Of particular significance to the analysis of communication systems, the total FWM signal is approximately 3 dB greater than expected from intra-mode nonlinearity alone (purple dotted line). This would be expected to reduce the total capacity of a fibre link. Therefore, it is possible to use the experimentally confirmed model to derive an expression for the overall capacity limit of FMF.



## 4.5 New Capacity Limits

Developing on the work presented on capacity limits presented in Chapter 2 and briefly at the start of this chapter (see Section 4.1) and having established the accuracy of Equation 4.17 experimentally in Section 4.4, it may be shown that the relative nonlinear capacity per unit bandwidth ( $C/B$ ) of an M mode fibre can be expressed as,

$$\frac{C}{B} = \sum_{n=1}^m \log \left( 1 + \frac{P_s}{P_N + \sum_{i,j,k} \eta_{ijkn} P^3} \right) \quad (4.19)$$

where  $P_s$  is the signal power,  $P_N$  the accumulated noise power and  $\eta_{ijk}$  has been defined in Equation 4.17.

This reveals the expected M-fold increase in capacity but with a small reduction due to the relative strength of inter-mode FWM. Figure 4.30 shows predictions of Equations 4.17 and 4.19 for the four mode fibre used in the FWM measurements. The capacity limits were calculated using the data provided in Table 4.1 (Fibre III) and a  $\approx 3$  dB increase in FWM signal which was measured experimentally, other parameters included in the models are presented in Table 4.2.

Table 4.2: Data used to seed nonlinear Shannon models

System Characteristics		
WDM Channel Spacing	50	GHz
Local Dispersion (ps/nm km)	20	ps/nm km
Nonlinear Index Coefficient	$27 \times 10^{-21}$	$m^2/W$
Centre Wavelength	1550	nm
Length	3200	km
Fibre Loss	0.2	dB/km
Amplifier Spacing	80	km
Amplifier Noise Figure	4.5	
Number of WDM Channels	100	

The two models are graphed in Figure 4.30, one showing the capacity limit of each mode assuming negligible inter-mode FWM (black lines). The second set (red lines) are the capacity limits predicted using the model presented here with the additional inter-mode FWM signal which was quantified experimentally. For any given mode, the difference in performance is small. However, summed over the fibre the overall fibre capacity is reduced by  $\approx 2.5$  b/s/Hz.

The work presented here has developed valuable tools to asses the capabilities of FMF both numerically and experimentally. This work indicates that inter-mode FWM can reduce overall capacity in fibres that show velocity matching between modes. This ve-

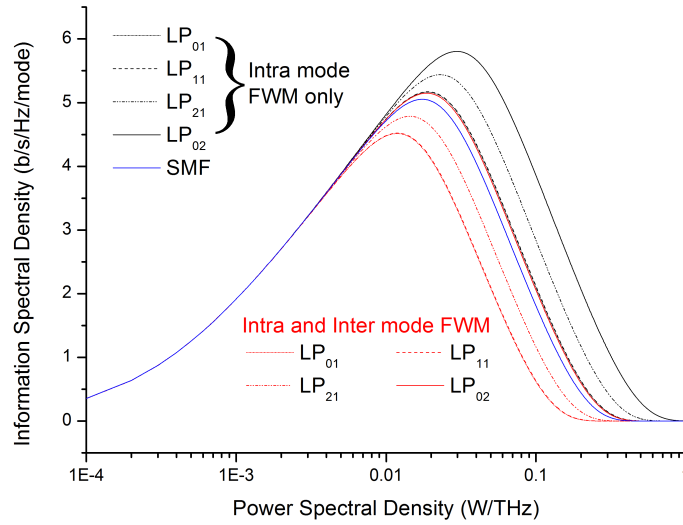


Figure 4.30: Calculated nonlinear Shannon limit for modes of a FMF neglecting inter-mode FWM (black) and including inter-mode FWM (red). The blue trace shows the nonlinear limit of SMF for comparison.

locity matching can be reduced by increasing the relative DMD between modes. However, as previously stated this increases DSP overhead. Hence, the ability to calculate the optimum fibre, where all trade-offs are quantified, is paramount to the successful deployment of any future FMF system.

#### 4.5.1 Choosing a Radically New Fibre

Figure 4.30 shows how, with a lack of careful fibre design, it is possible for FMF to only give a linear growth of capacity, where each mode only has a capacity comparable to SMF. The capacity of each mode is reduced even further by the addition of modes with DMD values between the fastest and slowest modes due to additional inter-mode FWM. This will fundamentally limit the potential capacity growth possible with FMF. Such a growth could be achieved with further deployment of SMF (blue line Figure 4.30). Though this is an extreme example, it does raise concerns over FMF. It has been shown that larger effective areas do reduce nonlinear effects such as SBS and SPM and that models can accurately predict their behaviour. However, the question remains, is there sufficient capacity increase using FMF over SMF to warrant a complete overhaul of transmitter, optical amplifier, receiver and the optical channel itself? If such a radical overhaul is to take place there is another type of fibre that has the potential to radically expand the capacity of a single fibre; hollow core photonic band-gap fibre.

Figure 4.31 shows the high capacity potential of HC-PBGF over FMF (red) and

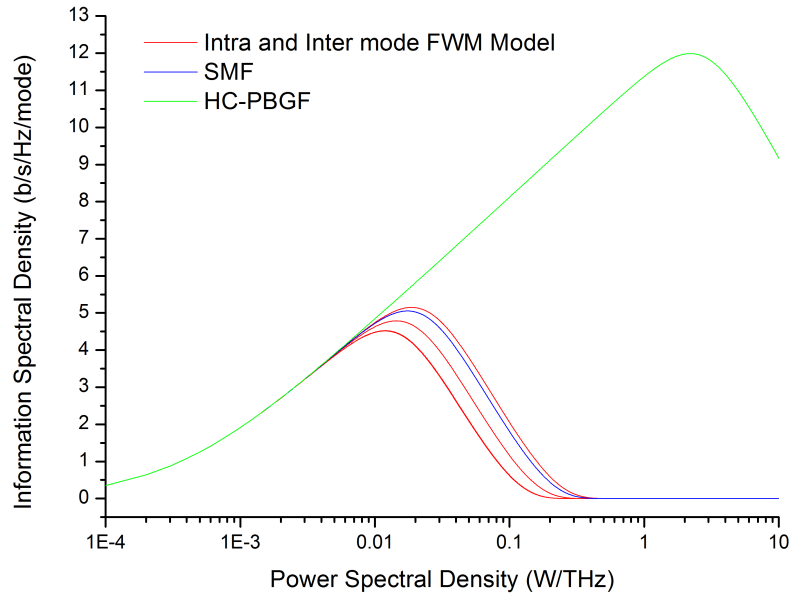


Figure 4.31: Nonlinear Shannon limit for each mode of a FMF (red) based on new numerical model. Blue trace shows nonlinear limit for SMF and green trace the limit for HC-PBGF operating at 1550 nm with 0.2 dB loss.

SMF (blue). This increase is due to the reduced nonlinearity (here assumed to be 0.001W/km) due to light propagating in the hollow core and reduced interaction with silica interface. HC-PBGF also has the potential of ultra-low-latency and low-loss transmission, but this requires operating outside standard wavelengths. Thus, there are several challenges with developing new subsystems based on HC-PBGF. These new subsystems are the subject of the next chapter.

## Chapter 5

# Transmission Over Hollow Core Photonic Bandgap Fibre at 2 $\mu$ m

*"If I had asked my customers what they wanted they would have said a faster horse."*

Henry Ford

The nonlinear Shannon limit is within touching distance [1, 4]. From the Shannon view point it is our "channel" that has become the bottle-neck. The community has started to investigate solutions to improve the shortcomings of the optical channel. The most radical of these solutions is the introduction of new types of fibres, such as few mode fibre and hollow core fibre. As we've seen in Chapter 4 the issue of nonlinearity still exists in FME, though there is an improvement over SMF. However, due to the structure of HC-PBGFs the issue of nonlinearities is assumed to become far more remote when compared to both SMF and FME. Experimental results have shown transmission nearing 99.7% of the speed of light in a vacuum, indicating a reduced interaction with the glass and thus lower nonlinearity resulting from  $\chi'''$  effects in the glass [25]. This chapter will explain some of the major advantages of using HC-PBGF, including its potential for ultra low-loss transmission (Section 5.1). From there, the chapter will outline the required technologies and requirements to build a system at 2  $\mu$ m (see Section 5.2). Finally, the chapter will conclude, in Section 5.3, with the first ever direct implementation of an optical transmission system at 2  $\mu$ m with details on the construction of the subsystem, culminating in the world's first demonstration of WDM transmission over a HC-PBGF at the predicted low-loss region of 2  $\mu$ m. A total capacity of 16 Gbit/s is achieved using  $1 \times 8.5$  Gbit/s and  $3 \times 2.5$  Gbit/s channels modulated using NRZ OOK over 290 meters of hollow core fibre. Further results indicate that the system is fully scalable and promising for future integration with more advanced modulation formats.

## 5.1 Moving to 2 $\mu$ m

### 5.1.1 Transmission Windows and Loss Reduction

Table 5.1: Comparison of fibres since the 1960s with noteworthy achievements in solid core and hollow core fibre fabrication.

Solid Core Fibres			
Year	Loss (dB/km)	Comment	Reference
1966	1000	Silica glass at 0.8 $\mu$ m with assumed window bandwidth of 100 nm	[133]
1970	20	Doped-silica fibre with assumed window bandwidth of 100 nm	[134]
1973	4	Outside vapour deposition at 0.8 to 0.85 $\mu$ m window bandwidth $\approx$ 100nm	[135]
1974	2	Modified chemical vapour deposition process at 1.06 $\mu$ m window bandwidth $\approx$ 100 nm	[136]
1976	0.5	Multi Mode germania doped silica fibre at 1.3 and 1.5 $\mu$ m window bandwidth $\approx$ 100nm	[137]
1979	0.2	Standard SMF at 1.55 $\mu$ m $\approx$ 100nm window bandwidth	[30]
2013	0.15	Recent SMF record at 1.5 $\mu$ m $\approx$ 200 nm window bandwidth	[34]
Hollow Core Fibres at 1.5 $\mu$ m			
2003	25	silica/air photonic bandgap $\approx$ 120nm window at 1.5 $\mu$ m	[138]
2004	1.7	silica/air photonic bandgap $\approx$ 25nm window at 1.56 $\mu$ m	[139]
2013	3.5	silica/air photonic bandgap $\approx$ 160nm window at 1.5 $\mu$ m	[25]
Predicted	0.2	assumed 160nm window at 1.5 $\mu$ m	[140]
Hollow Core Fibres at 2 $\mu$ m			
2009	15	7-cell core $\approx$ 190nm window	[141]
2012	4.5	19-cell core $\approx$ 152nm window at 2 $\mu$ m	[142, 143]
Predicted	0.1	assumed 300nm window at 2 $\mu$ m	[140]

Historically optical communications has been carried out in three transmission "windows". "Windows" refer to a particular bandwidth of the spectrum where the loss of the fibre is at a local minimum. Each "window" was typically used due to some technical development that made a particular bandwidth usable; such as the development of opto-electronic devices (e.g. lasers). In the following sections the bandwidth of the

low-loss transmission region was taken to be the frequency range where a fibre maintains a continuous loss value within 3 dB of its minimum value. In the early 1960s, the lowest loss where there were usable subsystems, such as lasers and detectors, could be found in silica fibres at the 0.8 $\mu$ m wavelength [133] with a typical loss of 1 dB/m, and became the first "window". In 1966 K. C. Kao and C. A. Hockham [144] outlined how the loss of the fibre was a result of impurities in the fibre and predicted that these impurities could be removed so that the fibre loss could be reduced to 20 dB/km. It was at this point that optical fibre became a viable alternative to traditional coaxial cable and was referred to as the "threshold of usefulness" [145]. This is a somewhat arbitrary threshold, defined by Li, that corresponds to loss <20dB/km when SMF became largely adopted. Once the initial drop in loss was achieved it was followed by rapid progress in the area and, before long, loss was reduced even further. The progress during this time is summarised in Figure 5.1 by the red data points. This further loss reduction, along with continued subsystem development, lead to the opening of the second and third windows at 1.3 $\mu$ m and 1.55 $\mu$ m respectively.

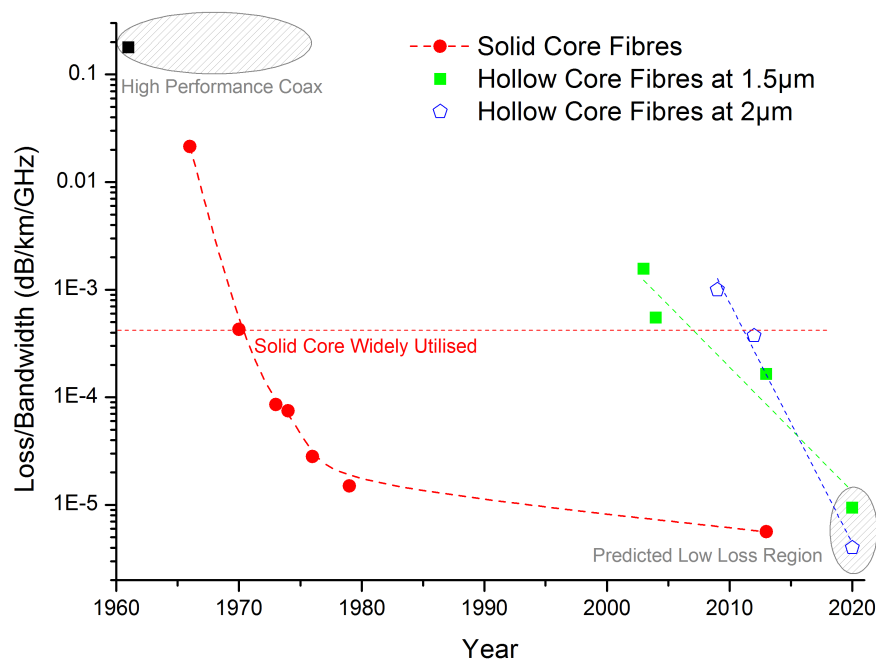


Figure 5.1: Historical progress of loss reduction in solid core fibres (red), Hollow Core Photonic Bandgap fibres at 1.5 $\mu$ m (green) and Hollow Core Photonic Bandgap fibres at 2 $\mu$ m (blue). Loss divided by the fibre low-loss bandwidth ("window" bandwidth) is used to compare fibres operating in different wavelengths and provides a figure of merit to compare fibres with varying low-loss bandwidths. (Source material in Table 5.1 where data for high performance Coax was taken from [146]).

All the major loss reductions in the 1970s were made in solid core fibres and had dif-

ferent "windows" of low-loss. In order to compare these fibres with varying window bandwidths and centre wavelengths, the figure of merit of *loss per window bandwidth*, measured in dB/km/GHz, is used. Indeed this figure of merit can be used to compare all types of wave-guides. This figure of merit is particularly useful when comparing hollow core fibres as the low-loss bandwidth varies greatly from fibre to fibre. Further details on the comparison of these fibres can be found in Table 5.1. What is particularly interesting in Figure 5.1 is the comparison to the more modern hollow core fibres. Only since 2012 has hollow core fibre crossed the point in performance where SMF was adopted. This was the point where the performance of fibre was said to outstrip the performance of coax cable. However, looking at the shaded region to the left of Figure 5.1 it can be seen that fibres were capable of out performing coaxial cable long before this "threshold" point. In the 1950s and 60s coax cables reported to have loss in the region of  $\sim 2$  dB/km [146] with typical values being closer to 2 dB/m [147]. In all cases coax cables have less bandwidth (typically  $< 10$  GHz) than the alternative fibre solution. This points to a lag between when SMF became a high performing alternative to coax cable and the actual point when it was widely adopted. Possible reasons for this include (i) commercial viability and cost (ii) industrial inertia to new technologies and (iii) subsystem bottlenecks. Though (i) and (ii) are beyond the scope of an engineering PhD (iii) falls in the realm of engineering. It is possible that subsystem bottlenecks such as transmitters and receivers being limited to less than 10 GHz and lacking WDM technology meant that the added bandwidth benefit of SMF was difficult to exploit and thus reducing the loss became the dominant factor in fibres being adopted. When moving to a new wavelength it is likely that similar challenges will be faced where possible technology bottlenecks are discussed in Section 5.2. This being said, the primary enabling factor for hollow-core fibre transmission at 2  $\mu$ m remains loss reduction.

Figure 5.2 shows the loss of solid core and hollow core fibres across a large spectral bandwidth. The loss mechanisms that fundamentally limit transmission through optical fibres has long been an area of study [148] and has been covered in Chapter 2 where the traditional optical transmission "windows" have been discussed along with the main loss mechanisms. Over the years different fabricating processes have reduced impurities and removed contaminants [135].

The loss reduction in solid core fibre has continued to this day [34], to the point where loss is dominated by Rayleigh scattering up to 1.66  $\mu$ m after which infra-red absorption losses become dominant. However, in contrast to solid core fibres, light in hollow core fibres is not guided by total internal reflection and Snells law. Instead, the light is confined to the core due to the bandgap created by the fibre structure (see Chapter 2). This means that over 99% of the light propagates through the centre of the fibre even when the centre is made of air. Concordantly, infrared absorption and Rayleigh scattering losses can be dramatically reduced. Figure 5.2 shows how the different method

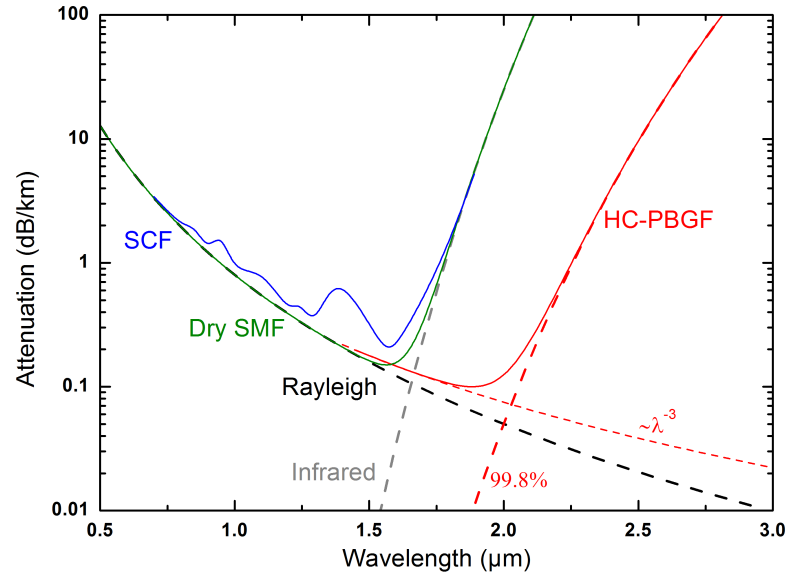


Figure 5.2: Fibre loss illustrating the traditional low-loss windows (0.8 $\mu$ m, 1.3 $\mu$ m and 1.5 $\mu$ m) with impurity losses as described in Chapter 2 Figure 2.5. The practical low-loss SMF is shown in green as predicted by [140]. Red traces show the predicted fourth transmission window for hollow core fibre at 2 $\mu$ m where infrared absorption is reduced and surface scattering ( $\sim \lambda^{-3}$ ) dominates over Rayleigh scattering

of propagation in hollow core fibres allows the existence of a fourth window at 2  $\mu$ m where the loss mechanisms are dominated by scattering from the air/glass interface ( $\approx \lambda^{-3}$ ) up to 2.03  $\mu$ m, at which point infra-red absorption losses become dominant yet again. This fourth transmission window was predicted by Roberts et al. [140] where loss could be as low as 0.1 dB/km over a large bandwidth. Therefore, hollow core fibre offers attractive possibilities for low loss transmission with continued progress in reducing loss [25]. Provided that this progress is maintained and assuming that commercial challenges and industrial inertia can be overcome subsystem requirements should be addressed now to identify and overcome any potential bottlenecks. Already, mode multiplexing over hollow core fibre has been demonstrated [97]. This was done at the traditional 1.5  $\mu$ m wavelength where there is well established infrastructure. Moving to 2  $\mu$ m will require many supporting technologies in order to unlock any available bandwidth.

## 5.2 2 $\mu$ m System Components

This section outlines some of the components that have been developed under the MODE-GAP project [149]. The follow sections give a brief overview of some of the major components that enabled system demonstrations. There are a number of com-



ponents, that are not listed here, that were commercially obtained. These commercial products will be explained, as required, in Section 5.3.

### 5.2.1 2 $\mu$ m Single Mode Lasers

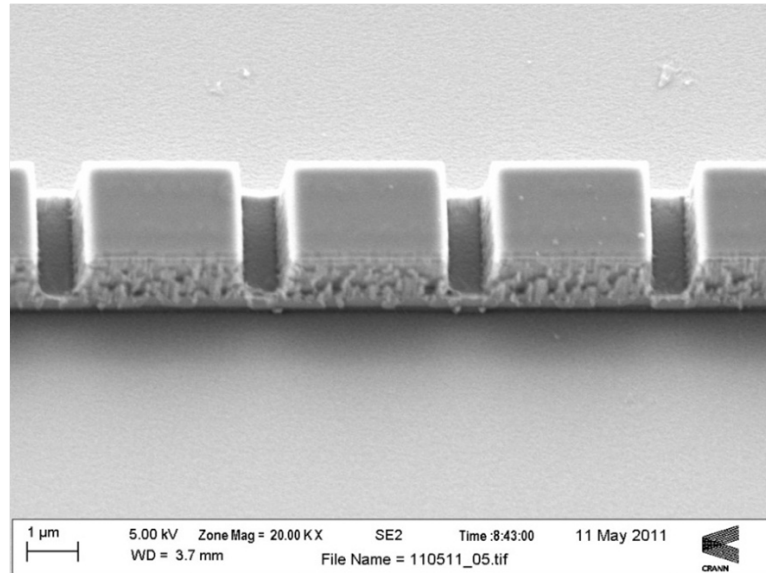


Figure 5.3: SEM image of etched waveguide structure. Courtesy of Eblana Photonics [150].

Loss reduction was not the only breakthrough in the 1970s and 80s, it was the advent of supporting technologies that turned optical systems into the backbone of global communications that they are today. Particularly important in building a system was the realisation of AlGaAs lasers at room temperature in 1970 [151, 152], followed by lasers using InGaAsP on InP in 1976 [153]. The same is true for the development of components at 2  $\mu$ m, one of the most critical components required being the lasers. Eblana Photonics have designed and fabricated a discrete mode laser operating at 2  $\mu$ m, where the author was involved in helping characterise both the material and packaged devices. The lasers have been designed using traditional InP based material, due to the technologies maturity at traditional communication wavelengths.  $In_{0.75}Ga_{0.25}As$  can be used to create a bandgap material around 2  $\mu$ m, this is done by introducing strain in the lattice between the  $InGaAs$  and the  $InP$  substrate. More details on the material growth can be found in [154, 150]. A single mode of the Fabry P rot material structure is selected by etching slots into the upper waveguide layer. A scanning electron microscope (SEM) image of the material structure can be seen in Figure 5.3, where the etched slots can be seen as a series of vertical lines running through the material. The slots are used to isolate a single mode where the resonator has a facet on either end (facet is not shown in Figure 5.3. The cavity is orientated in the horizontal direction and the current flows from top to bottom of the image).

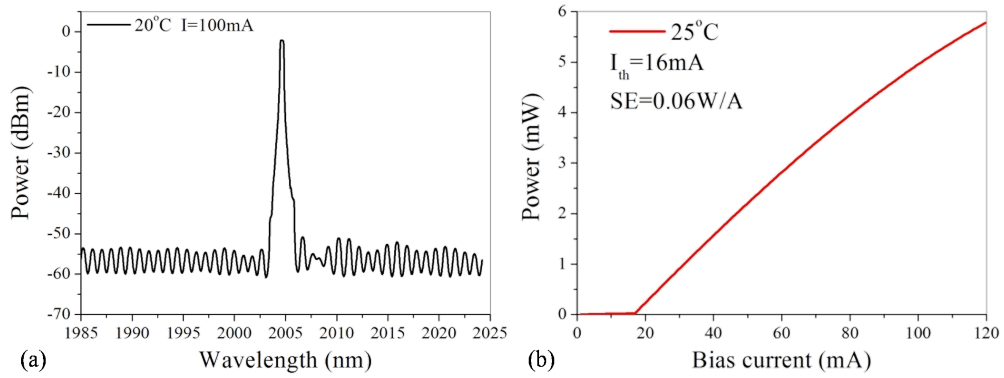


Figure 5.4: Laser characteristics: (a) Spectrum of a laser operating at 2005nm with  $\approx 50$  dB SMSS, measured at 20°C with 100 mA bias current. (b) Output optical power as a function of bias current, threshold at 16 mA.

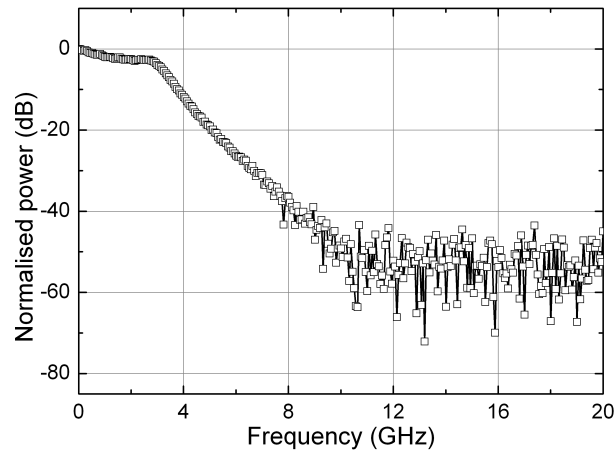


Figure 5.5:  $s_{21}$  measurements of packaged 2 $\mu$ m laser, indicating a 3dB bandwidth  $\approx 3$  GHz.

The slotted laser structure successfully isolated a single Fabry P  rot mode and gave a high side mode suppression ratio ( $> 40$  dB) from the other Fabry P  rot modes by the careful etching of slots in the upper InP waveguide [150]. This single mode operation is shown in Figure 5.4(a), where the measurements were taken on bar using a simple coupling fibre connected to an optical spectrum analyser with 0.2 nm bandwidth resolution. Figure 5.4(b) shows the output optical power as a function of bias current with optical powers  $> 5$  mW ( $\approx 7$  dBm) before packaging. After cleaving, the lasers were packaged in a butterfly package with 60% coupling efficiency into a solid core fibre pigtail. The packaging was designed to allow direct modulation of the lasers. In order to ascertain the frequency response of the packaged device, an  $s_{21}$  measurement was taken using a network analyser and a commercially available 8 GHz 2  $\mu$ m detector, where an  $s$  parameter corresponds to a particular element in a

two port scattering matrix where each component is a vector giving amplitude and phase information. For the purposes of this work the  $s_{21}$  parameter can be thought of as a measurement of voltage out versus voltage in as a function of frequency. An optical isolator was used between the laser and detector to reduce any reflections that would degrade the frequency response, the second generation of butterfly packages incorporate an optical isolator within the package. The results are plotted in Figure 5.5 and show a 3 dB bandwidth of  $\approx 3$  GHz after which there is a gradual roll-off in response due to the capacitance of the material affecting the RC time constant. The frequency response of the laser could be increased by reducing the capacitance of the material by careful regrowth of a semi-insulating layer [155, 156].

### 5.2.2 2 $\mu$ m Photodiodes

High speed optical communication systems are impossible to achieve without the use of high speed detectors. The required properties of 2  $\mu$ m photodiodes for communications include high speed, high responsivity as well as low dark current. These properties are significantly dependent on the design of the material. In this case the same InGaAs on InP material, as outline in Section 5.2.1, was used to produce the required bandgap at 2 $\mu$ m. The quantum wells in this material reduce the lattice strain and, as a result, low defect density and, therefore, low noise. Further details of the material can be found in [157].

In the first generation design, an edge coupled waveguide structure was adopted instead of a top illuminated mesa structure for achieving both high speed and high efficiency simultaneously. This design allows the flexibility for monolithic integration with other waveguide based optoelectronic devices on InP substrates, such as laser diodes, semiconductor optical amplifiers, and electro-absorption modulators that may be developed in the future. In order to achieve high speed, which is determined by the RC time constant and the carrier transit time, a small intrinsic area is preferred in order to minimise capacitance.

The electrode pads consisted of a coplanar ground-signal electrodes with benzocyclobutene polymer underneath, designed to minimise parasitic capacitance for enhanced high speed performance. The structure of the device can be seen in Figure 5.6 and is described in detail in [157]. The device consisted of a deep etched ridge through the quantum wells layers where SiO<sub>2</sub> was used as the etching mask followed by deposition of a 150 nm thick SiN<sub>x</sub> passivation layer. A BCB layer (Benzocyclobutene polymer passivation layer) was then spin coated and cured followed by a further etch to access the n-type InP. This was followed by a layer of SiO<sub>2</sub> to increase adhesion with the metal contacts. A final etching process was used to access both the n- and p-type contacts before TiAu was evaporated for both p- and n-type metal electrodes.

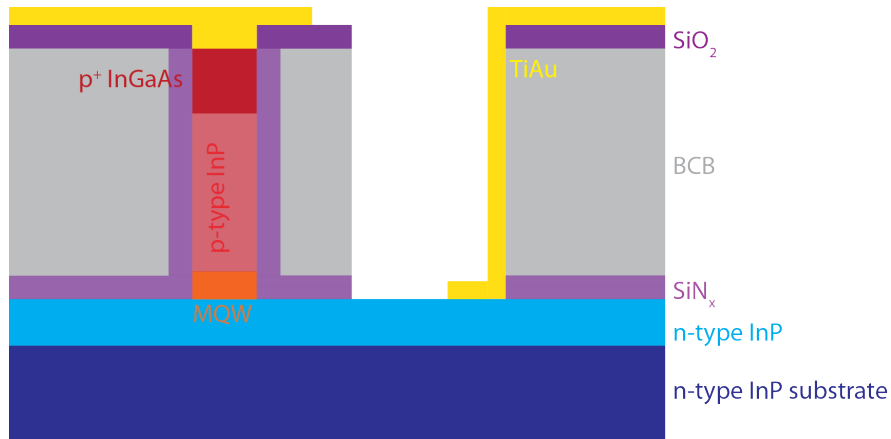


Figure 5.6: Schematic of 2 $\mu$ m photodiode layer structure.

When the device was measured it showed very low leakage  $< 120$  nA with  $-3$  V bias voltage and a photoresponsivity of 0.3 A/W. The low leakage current indicates the material has very good crystal quality and the fabrication process was successful. The responsivity of 0.3 A/W is relatively low, and is limited by the low coupling efficiency between the waveguide mode and the fibre mode. The responsivity could be potentially improved to a photoresponsivity  $> 1$  A/W by AR coating the input facet or by integration with a mode size converter to match the fibre mode.

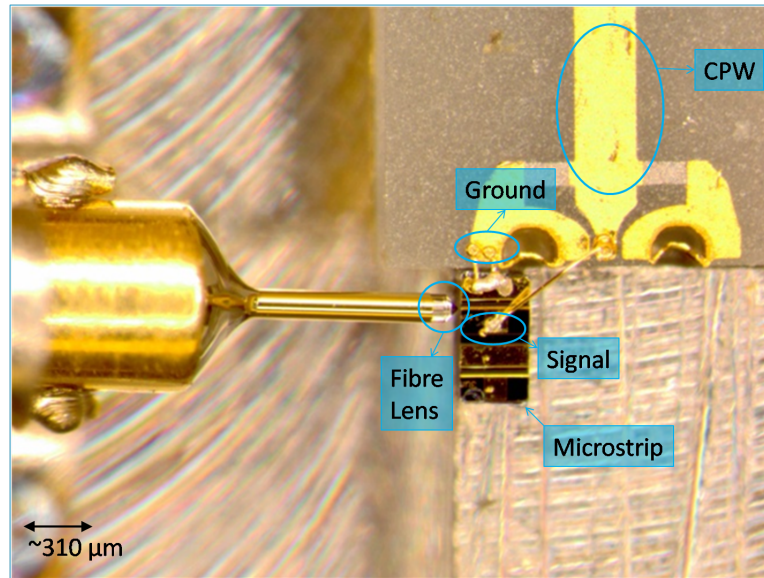


Figure 5.7: Image of 2 $\mu$ m photodiode in unsealed package.

To characterise the high-speed performance of the device, a high-speed butterfly package with a K (2.92 mm) connector was used. The device was wire bonded to a specially designed high-speed micro-strip line and CPW lines integrated circuit on AlN with two  $100\Omega$  resistors in parallel for impedance matching to reduce the reflection loss. A lens ended (angle:  $85^\circ$ , curvature radius:  $11.5 \mu\text{m}$ ), single mode fibre (core NA: 0.20, for reduced loss at  $2 \mu\text{m}$ ) was used to couple light into the waveguide of the device in

the package. Figure 5.7 shows a microscope image of the packaged device. The small signal response of the packaged PD was measured at 2  $\mu\text{m}$  using the setup shown in Figure 5.8.

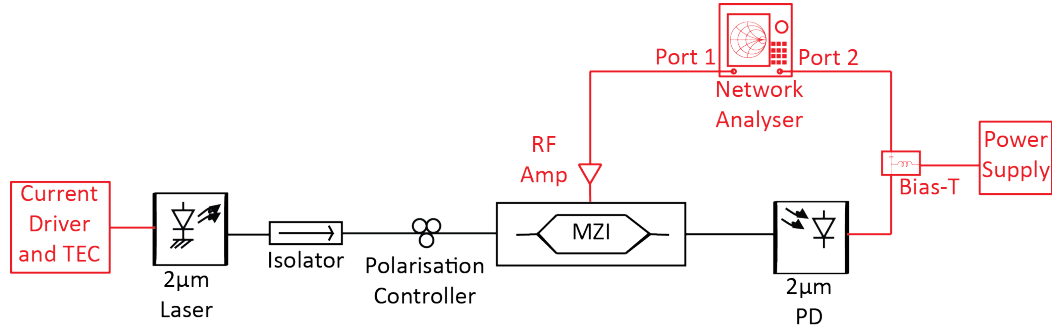


Figure 5.8: Setup for measuring  $s_{21}$  of 2  $\mu\text{m}$  detector with optical paths shown in black and electrical paths shown in red.

The optical setup consisted of a 2  $\mu\text{m}$  laser, optical isolator, polarisation controller, 2  $\mu\text{m}$  Mach-Zehnder modulator and 2  $\mu\text{m}$  detector (the device under test). The 2  $\mu\text{m}$  laser was powered using a current source set to  $\sim 85$  mA (for  $\sim 3$  dBm) and was temperature controlled to set the wavelength at 2006 nm. The 2  $\mu\text{m}$  detector was powered via a bias-T with the AC port of the bias-T connected to port 2 of the network analyser. The output port (port 1) of the network analyser was connected to the 2  $\mu\text{m}$  Mach-Zehnder modulator via an RF amplifier (where the output voltage swing of the amplifier was  $\sim 10$  V). The RF cables were first calibrated by connecting the output of the RF amplifier to the cable attached between the 2  $\mu\text{m}$  detector and bias-T in Figure 5.8. The remaining results were normalised to this measurement to remove any responses from the cabling and connector adapters (connectors not shown in Figure 5.8). When measuring the frequency response of the RF path no major frequency roll-off was visible up to 20 GHz. The RF connections were then connected to the Mach-Zehnder modulator and 2  $\mu\text{m}$  detector respectively and the resultant  $s_{21}$  plots can be seen in Figure 5.9(bottom). To mitigate the response of the Mach-Zehnder modulator the experiment was also performed at 1.55  $\mu\text{m}$  using a 1.55  $\mu\text{m}$  laser and detector, where the detector had 60 GHz bandwidth. The system was calibrated using a 40 GHz 1.55  $\mu\text{m}$  modulator as reference before measuring the frequency response of the 2  $\mu\text{m}$  modulator, the result can be seen in the blue trace of Figure 5.18 where the modulator has a 3 dB bandwidth of  $\sim 10$  GHz. The 40 GHz 1.55  $\mu\text{m}$  modulator was again placed in the system to measure the response of the 2  $\mu\text{m}$  detector at 1550nm.

A modulated light signal was input to the packaged PD which was reverse biased under different voltages. The optimum frequency response performance was found at a reverse bias voltage of 5 V. The measured 3dB bandwidth of the packaged device is shown in Figure 5.9 where the device was measured at 1.5 $\mu\text{m}$  to have a 3 dB bandwidth of  $\sim 14$  GHz. The bandwidth at 2  $\mu\text{m}$  reduced to 10 GHz. This reduction is believed to be bandwidth limited by the 2  $\mu\text{m}$  modulator which, as will be dis-

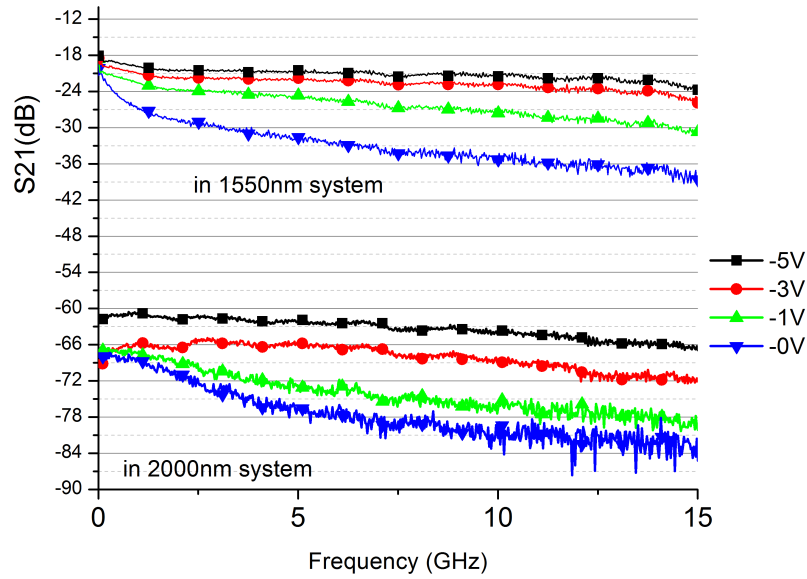


Figure 5.9: Frequency response of 2 $\mu$ m photodiode, attained from S21 measurements.

cussed in greater detail in Section 5.3, had a bandwidth of  $\sim 10$  GHz. The sensitivity is considerably reduced at 2  $\mu$ m due to the coupling efficiency between the waveguide mode and fibre mode. The low sensitivity made the detector unsuitable for use with the transmission experiments and a commercially available detector was used. Since completion of this thesis the material has been re-fabricated with a mode size converter and AR coating giving a higher sensitivity.

### 5.2.3 Thulium-Doped Fibre Amplifiers

The implementation of the erbium doped fibre amplifier in 1987, considered revolutionary at the time, signified continued progress in optical communications by removing the need for complex optoelectronic regenerators. In order for 2  $\mu$ m transmission to be viable, such amplifiers must be created in the 2  $\mu$ m window.

Thulium ( $Tm^{3+}$ ) is a very promising candidate for optical amplification in this band. It produces a remarkably broad,  $\approx 30$  THz, emission spectrum due to the  $^3F_4 \rightarrow ^3H_6$  transitions in  $Tm^{3+}$  doped silica. This is about double the bandwidth of erbium doped fibres  $^4I_{13/2} \leftrightarrow ^4I_{15/2}$  transitions, compared to  $\sim 15$  THz for  $Er^{3+}$  doped silica. The ASE of the first generation TDFA is compared to a modern day EDFA in Figure 5.10, this illustrates the potential for TDFAs to surpass the bandwidth of existing EDFAs.

A thulium doped optical fibre amplifier (TDFA) was developed for use in the system, and its schematic is shown in Figure 5.11. The amplifier was designed and constructed in the University of Southampton as part of MODE-GAP by Zihong Li and colleagues

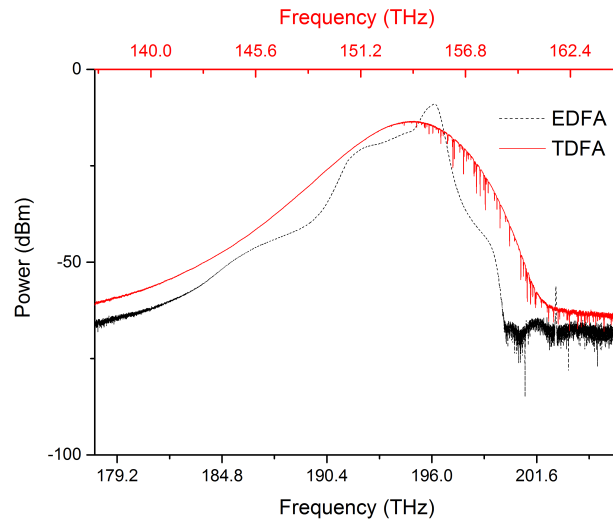


Figure 5.10: Comparison of first generation TDFA and EDFA ASE bandwidth. The sudden dips in the TDFA spectrum at high frequencies is likely due to gas absorption in the OSA.

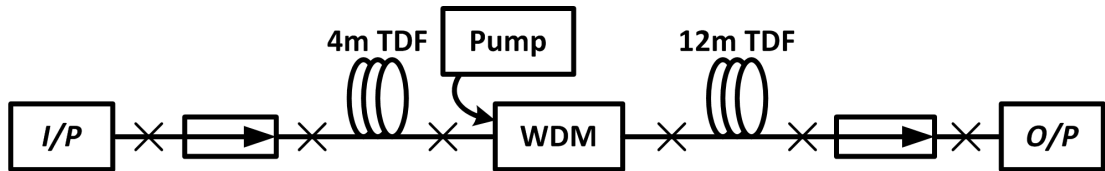


Figure 5.11: TDFA Block Diagram.

[158]. It was used extensively in the transmission experiments that are to follow. The amplifier was built with commercially available  $Tm^{3+}$ -doped fibre with a mode field diameter of 5  $\mu$ m at 1.7  $\mu$ m and absorption of 200 dB/m at 790nm (TmDF200)[159]. The amplifier had two stages, which provided enhanced gain at wavelengths around 2  $\mu$ m. It consisted of two sections: firstly, a 4 m long TDF section before the WDM coupler, followed by a second 12 m long forward-pumped TDF section after this coupler. The second section was forward pumped by a 1565 nm fibre Bragg grating (FBG) stabilized single mode laser. The first section was backward pumped by back-propagating ASE from the second stage which enhanced the long wavelength gain at 2  $\mu$ m by  $\approx$  5 dB. The amplifier gain and external noise figure (NF) are plotted in Figure 5.12, where the results were obtained by Zihong Li in the University of Southampton. The 3 dB gain bandwidth of the amplifier was  $\approx$  80 nm, centred at 1960 nm. A minimum NF of  $\approx$  6 dB was measured for practical input powers with pump powers above 27.5 dBm. A reduction of this NF should be possible and was limited in this case to the losses of the first generation of passive components used in the input stage of the amplifier. As can be seen from Figure 5.12(a), the TDFA had gains  $> 30$  dB for pump powers above 27.5 dBm.



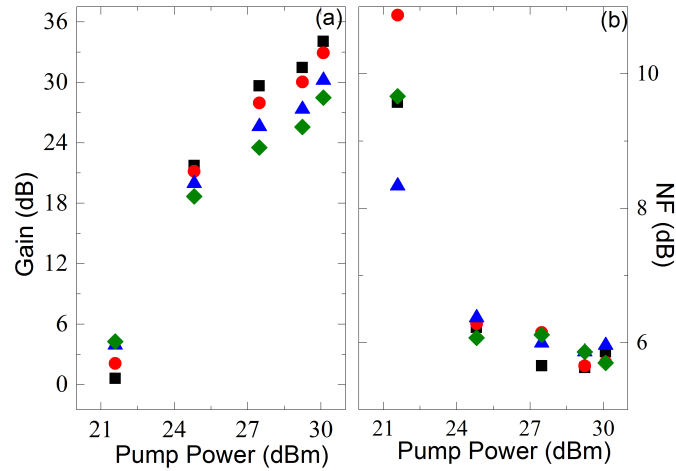


Figure 5.12: (a) Gain and (b) Noise Figure Performance of first generation TDFA, measurements provided by the author of [158].

#### 5.2.4 Hollow Core Photonic Bandgap Fibres

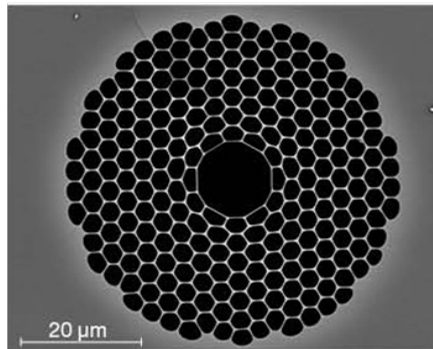


Figure 5.13: SEM image of the 19-cell hollow core fibre.

The basic principles of hollow core fibre have been outlined in Chapter 2 and their promising low-loss at 2 $\mu$ m has been discussed in Section 5.1, with much improvement in the reduction of loss recorded recently [97, 142]. For the transmission experiments we used fibres developed, by the University of Southampton. A 19-cell core structure, illustrated in Figure 5.13, was developed for low-loss transmission at 2  $\mu$ m. The cladding was composed of 6½ rings of holes with an average spacing of  $\approx 5.5 \mu$ m and relative hole size of  $\approx 0.96 \pm 0.05$ . The core had a 36  $\mu$ m diameter, surrounded by a thin silica layer carefully engineered to minimise the number of surface modes, and hence obtain low-loss guidance with extended bandwidth [160]. The fibre was largely single mode with some surface modes present but with a higher order mode suppression of  $\approx 30$  dB. The attenuation characterisation is shown in Figure 5.14 (red trace), with a record minimum loss of  $< 4.5$  dB/km at 1.97  $\mu$ m, opening a bandwidth of  $\approx 152$  nm. As no precaution was taken to avoid atmospheric gas into the fibre during fabrication and characterisation, carbon dioxide absorption was observed at



the centre of the attenuation curve. The three most prevalent gasses at these wavelengths are  $CO_2$ ,  $H_2O$  and  $HCl$  (where  $HCl$  is present from the processing of the fibre preform), the absorption lines are plotted in Figure 5.14 in grey, blue and green respectively. As the absorption lines were very narrow (<60pm), de-tuning the lasers slightly ensured optimum performance for the proof-of-concept experiments. The data on the gas absorption was taken from the HITRAN database [161].

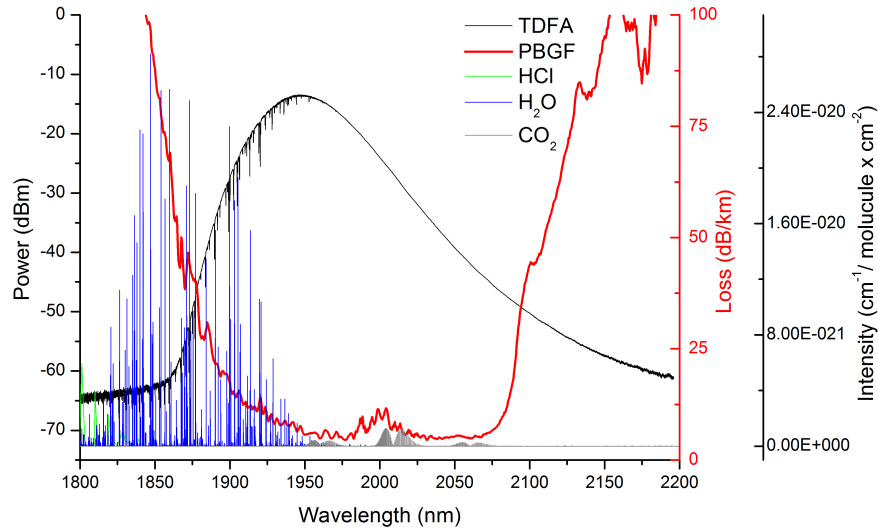


Figure 5.14: Plot of HC-PBGF transmission loss (red) along with ASE gain spectrum of TDFA (black). Green, blue and grey traces show intensity lines for  $HCl$ ,  $H_2O$  and  $CO_2$  respectively. Absorption lines taken from the HITRAN database [161] and loss spectrum based on [25].

Table 5.2: Key characteristics of the fibre used for transmission at 2 $\mu$ m

Hollow Core Fibre Characteristics	
Pitch ( $L$ )	5.5 $\mu$ m
$d/\lambda$	0.96
Core Diameter	36 $\mu$ m
Mode Field Diameter	estimated $\approx$ 22 $\mu$ m
3dB Bandwidth	152 nm
Minimum Loss	4.5dB/km @1970 nm
High Order Mode suppression	$\approx$ 30dB

### 5.2.5 Passive Components

This section outlines, briefly, some of the passive components that had to be developed at 2  $\mu$ m and used as part of the transmission experiments.

### 5.2.5.1 Couplers

Fused couplers were developed by Phoenix Photonics [162], using passive optical fibre with an excess insertion loss  $< 1\text{dB}$ . The couplers in this experiment consisted of a 4:1 combiner, consisting of three standard  $2 \times 2$  couplers.  $2 \times 2$  couplers were also available in power ratios of 50 : 50 and  $\approx 90 : 10$ .

### 5.2.5.2 Filters

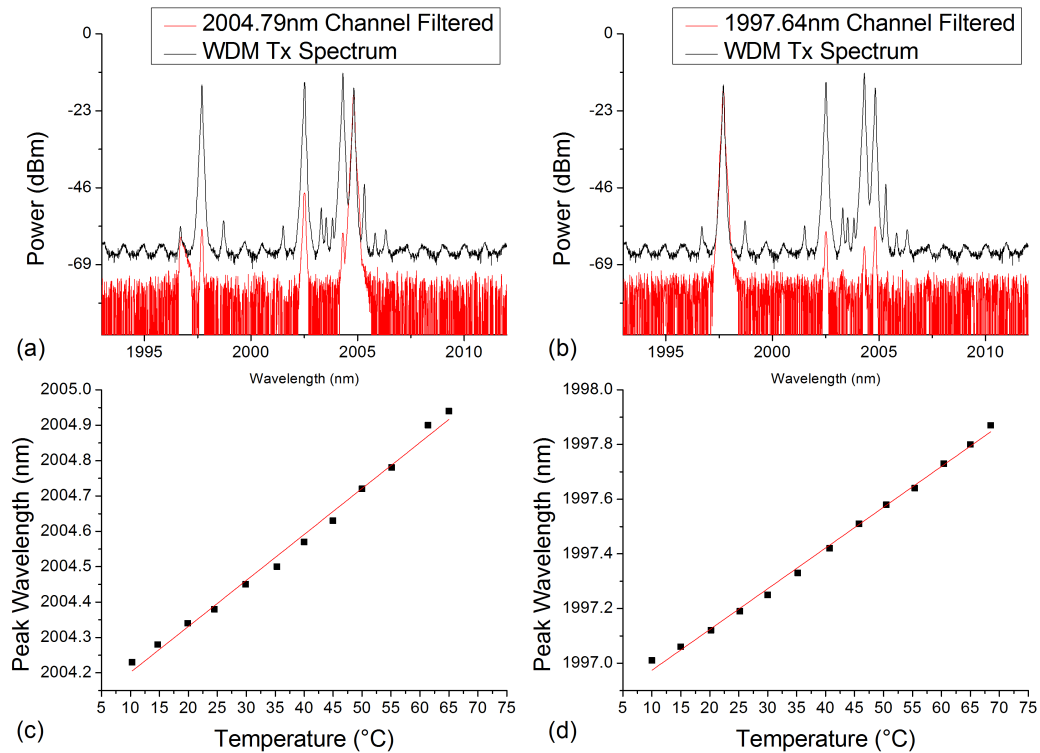


Figure 5.15: Filter characterisation with optical spectrum at 0.1 nm resolution where the output spectrum of a 4:1 combiner is shown in the black traces of (a) and (b). Red traces taken at the return port of the circulator using two separate Bragg gratings to filter 2004.79 nm and 1997.64 nm channels in (a) and (b) respectively.

For the system experiments, the filter comprised of a circulator and a set of three thermally tuned fibre Bragg gratings (FBG), with an extinction ratio  $> 20\text{dB}$ , a 3dB bandwidth of  $< 0.5\text{nm}$ , and a (thermal) tuning range  $> 1\text{nm}$ . Each of the wavelength channels were selected by a combination of inserting the relevant FBG to the circulator and tuning their temperatures. This resulted in a maximum loss of 3.5dB. A fibre Bragg grating for filtering the  $\sim 1997.64\text{ nm}$  channel was spliced to the output port of the circulator and was detuned to a lower wavelength when other channels were under test, this can be seen in Figure 5.15(a) where there are two peaks close to 1997 nm due to Bragg detuning. When studying the 1997.64 nm channel only a single Bragg

grating was used, with a thermal tuning range shown in Figure 5.15(d), where the fibre Bragg grating was placed on a thin sheet of aluminium with thermal paste. The temperature was controlled using Peltier plates placed under the aluminium strip. When tuning to the 2004.79 nm or 2004.27 nm channels a second Bragg grating was placed in series with the 1997 nm Bragg grating, an example can be seen in Figure 5.15(a) with a thermal tuning range given in Figure 5.15(c). Finally for the 2002.22 nm channel the 2004 nm Bragg grating was replaced with a Bragg grating tuned to the 2002.22 nm channel, though this filter remained in series with the 1997 nm Bragg grating. The 2002 nm and 2004 nm Bragg gratings only had a single side pigtailed with the the opposite side remaining a bare ended fibre cleave. It is possible that this lead to a reduced extinction ratio for the 2002.22, 2004.27 and 2004.79 nm channels due to reflections at the bare fibre output of the 2002 nm and 2004 nm Bragg gratings. This was mitigated by placing the bare fibre ends into index matching fluid. However, a slightly lower extinction ratio remained for the channels using the fibre Braggs with bare fibre ends, as can be seen in Figure 5.15(a). The best filtering was achieved for the 1997.64 nm channel (Figure 5.15(b)) where only a single Bragg grating was used, where both fibre ends were pigtailed with angled connectors and coupled to a spool of SMF to reduce the power of Fresnel reflections.

### 5.2.5.3 Patch Cords, Polarisation Controllers and Attenuators

Standard SMF has significant bending losses at 2  $\mu\text{m}$  ( $> 1$  dB for a one meter patch cord). 2  $\mu\text{m}$  polarisation controllers should be available in the near future [162]. In the interim, to reduce bending loss, Nufern SM1950 fibre was used with polarisation controllers. This fibre has a  $\text{SiO}_2/\text{GeO}_2$  doped core, with a core numerical aperture = 0.2. The fibre was used to create standard all-fibre polarisation controllers, made up of three paddles or "bat-ears" consisting of a turns ratio and bending diameter to create one half wave plate and two quarter wave plates. The polarisation controllers had an excess loss of  $\sim 0.6$  dB due to bending losses.

For the attenuators a SMF tunable attenuator, typically for 1550 nm, was used at 2  $\mu\text{m}$ . This had an excess loss of  $\sim 3$  dB and was very sensitive to manual adjustment. Figure 5.16 shows the attenuation as a function of input power with the attenuator manually adjusted to a single position and not adjusted over the course of the measurement. The measurements show a highly nonlinear relationship and accentuate the need for customised components for the 2  $\mu\text{m}$  wavelength. In the majority of cases the attenuator operated in the low input power region, where the performance was more linear. The input and output power of the attenuator was closely monitored when taking experimental measurements and the attenuator adjusted to maintain the required amount of attenuation.

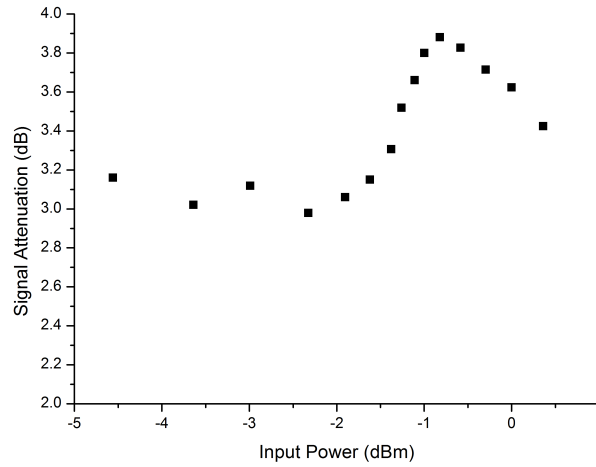


Figure 5.16: Plot of attenuation as a function of input power showing a nonlinear relation, particularly at high input powers.

### 5.3 System Experiments

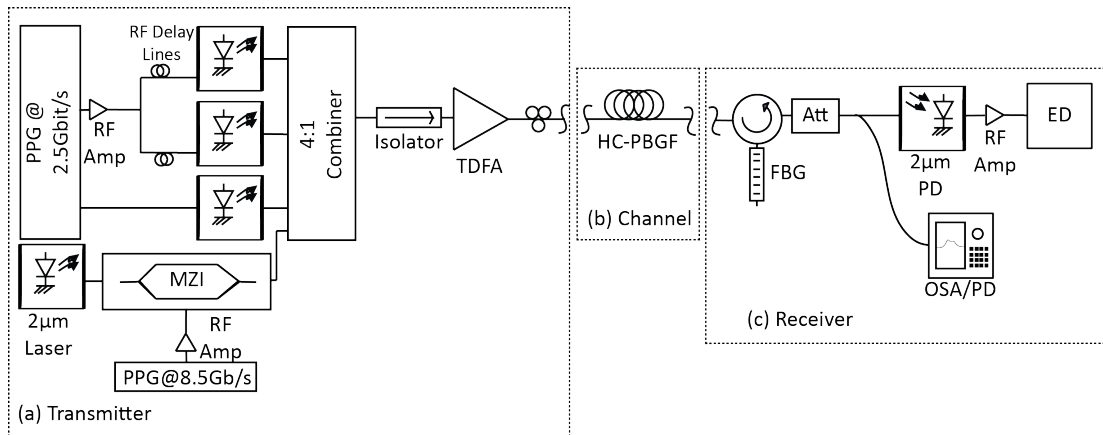


Figure 5.17: Experimental setup showing (a) Transmitter, (b) Channel consisting of 290m of HC-PBGF and (c) Receiver.

Figure 5.17 shows the experimental setup for the world's first 2  $\mu$ m WDM transmitter and receiver subsystem. The majority of the systems components were developed for the trial and are outlined in Section 5.2. For the transmitter, seen in Figure 5.17(a), four InGaAs/InP multiple quantum-well discrete-mode lasers, operating at 1997.64, 2002.22, 2004.27 and 2004.79nm wavelengths were used as the four source frequencies. Three of the lasers were directly modulated (2004.79, 2004.27 and 1997.64nm) to demonstrate the capabilities of the first generation of laser diodes. The lasers were directly modulated using a pulse pattern generator at 2.5 Gbit/s with data and data inverse output ports. The data output port was to drive two lasers with the signal first being amplified using an RF amplifier to maintain a  $V_{pp} \approx 1$  V for each laser, after

which the power was split evenly where an RF delay line was used to decorrelate the data in each path. The inverse data port of the pulse pattern generator was connected directly to the third directly modulated laser with 1 V peak to peak.

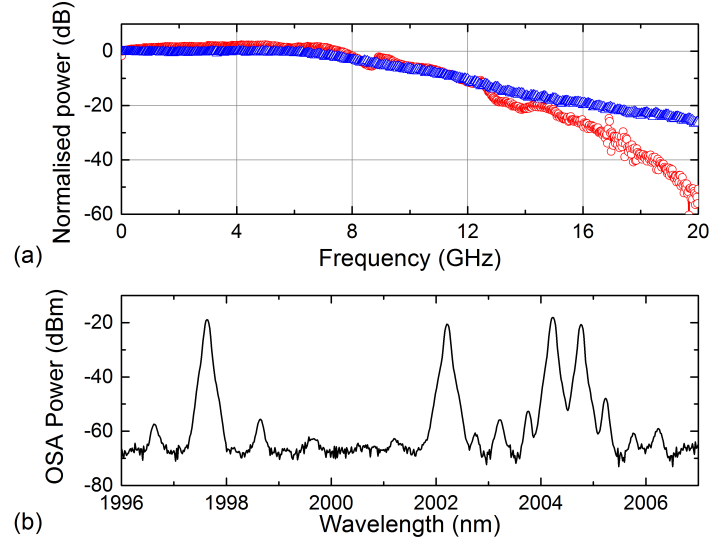


Figure 5.18: (a) S21 measurement of the external modulator at 1.5 $\mu$ m (blue) and at 2 $\mu$ m (red). (b) Spectrum showing the four channel WDM transmitter measured at the output of the 4:1 combiner with 0.1nm resolution bandwidth.

The remaining optical channel at 2002.22nm was biased to produce cw output power  $\approx 3$  dBm and from there propagate to an intensity modulator. At this point the wavelength was externally modulated using the commercially available LiNbO<sub>3</sub> Mach-Zehnder intensity modulator at a bit rate of 8.5 Gbit/s NRZ OOK using a  $2^{31} - 1$  pseudo random bit sequence, where the  $V\pi$  of the modulator was  $\approx 9.5V$ . The RF bandwidth of this channel was limited by the modulator and detector, with a combined 3dB frequency response of 8 GHz both at 1.5  $\mu$ m and 2  $\mu$ m (Figure 5.18(a), blue triangles and red circles respectively). The frequency response at 1.5  $\mu$ m used a detector with  $> 20$  GHz bandwidth and thus the frequency response of the modulator was directly measured. However, due to the bandwidth limitation of the 2  $\mu$ m detector the measurement at 2  $\mu$ m was a combined response of the detector and modulator.

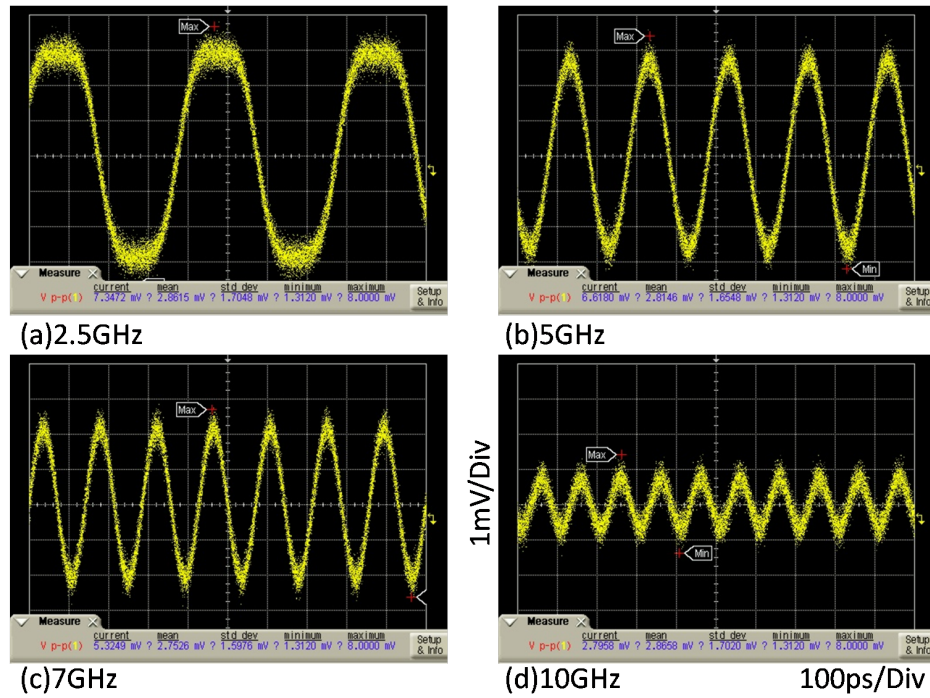


Figure 5.19: Modulator output for four clock frequencies applied to the modulator RF port. The four clock frequencies were (a)2.5 GHz, (b)5 GHz, (c)7 GHz and (d)10 GHz.

Figure 5.19 shows the resultant response of the modulator for bit rates of 2.5, 5, 7 and 10 Gbit/s. This was done by placing a clock synthesiser at the RF input of the modulator and adjusting the clock frequency. At 7 GHz (Figure 5.19(c)) the signal began to degrade with a rapid drop-off in performance after 8.5 GHz and continued to degrade (see Figure 5.19(d)) due to the frequency response of the 2  $\mu$ m detector. The 8.5Gbit/s bit rate was selected as it was the highest possible bit rate achievable with a tolerable penalty due to combined detector and modulator frequency response roll-off. The process was repeated when choosing an operating bit rate for the directly modulated lasers. Figure 5.20 shows the response of a directly modulated laser for three separate clock frequencies. The largest peak to peak voltage response was achieved at a frequency of 2.5 GHz, after which the signal degraded due to the frequency response of the laser.

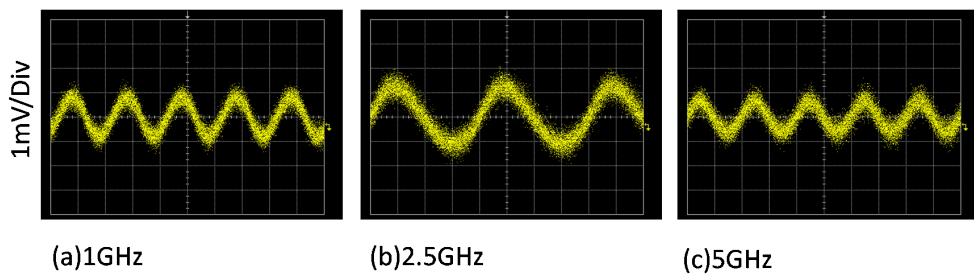


Figure 5.20: Laser output for three clock frequencies applied directly to the laser showing a reduced response for higher frequencies.

The WDM signals were then combined with a passive optical fibre based 4:1 combiner with an average excess loss of 1 dB, provided by Phoenix Photonics. The combiner was followed by an optical isolator, in order to avoid unwanted back reflections. It would be preferable to have an isolator at the output of each of the four lasers, however due to the scarcity of components at 2 $\mu$ m (and as a result, expense), only one isolator was used after the 4:1 combiner. Figure 5.18(b) shows the spectral output of the transmitter, with a 0.1nm resolution, showing that the side-mode suppression of the lasers was below 30dB. The spectrum was acquired using a Yokogawa AQ6375 long wavelength optical spectrum analyser.

The filter comprised a circulator and a set of three thermally tuned FBGs as outlined in Section 5.2.5.2. The individual filter components were commercially acquired and the filter was then assembled in-house. Each of the wavelength channels were selected by a combination of inserting the relevant FBG to the circulator and tuning their temperatures. This resulted in a maximum loss of 3.5 dB, at the negligible expense of a slight increase in the out-of-band spontaneous emission. The received power was then controlled with a tunable attenuator and a tap monitor was inserted to monitor, either, the optical power for the bit error rate (BER) measurements, or the filtered spectrum at the receiver. The optical power was measured using a ThorLabs long wavelength detector capable of measuring signal from DC to 10 MHz.

Finally, a high speed detector at 2  $\mu$ m was used. Unfortunately, the first generation 10 GHz 2  $\mu$ m detector described in Section 5.2.2 did not have sufficient responsivity and the packaging of the device required improvement. Instead, a commercially available 8 GHz detector from EOT was used, along with an RF amplifier. The detector had a responsivity of  $\sim 1.6$  A/W with an inbuilt transimpedance amplifier and a dark current  $< 300$   $\mu$ A with three volts reverse biased. Once in the electrical domain the signal was fed to a PRBS error detector where the clock was "bootstrapped" from the pattern generator clock output. As there were two separate bit rates this meant that two separate PRBS error detectors were used, both had a clock in common with their respective PRBS pattern generators. A picture of the complete setup can be seen in Figure 5.21.

### 5.3.1 Performance of 2 $\mu$ m Subsystems

In order to study the subsystems scalability the system was modified to carry an advanced modulation format operating at a higher bit rate of 5 Gbit/s. To achieve this BPSK using Fast-OFDM was selected as the most suitable candidate to maximise the use of the available bandwidth of the 2  $\mu$ m lasers while maintaining direct detection at the receiver. The BPSK Fast-OFDM format was implemented with the help of Dr. Jian Zhao and had 128 discrete-cosine transform point size, among which 106 subcarriers were used for data modulation. Direct modulation using BPSK Fast-OFDM on



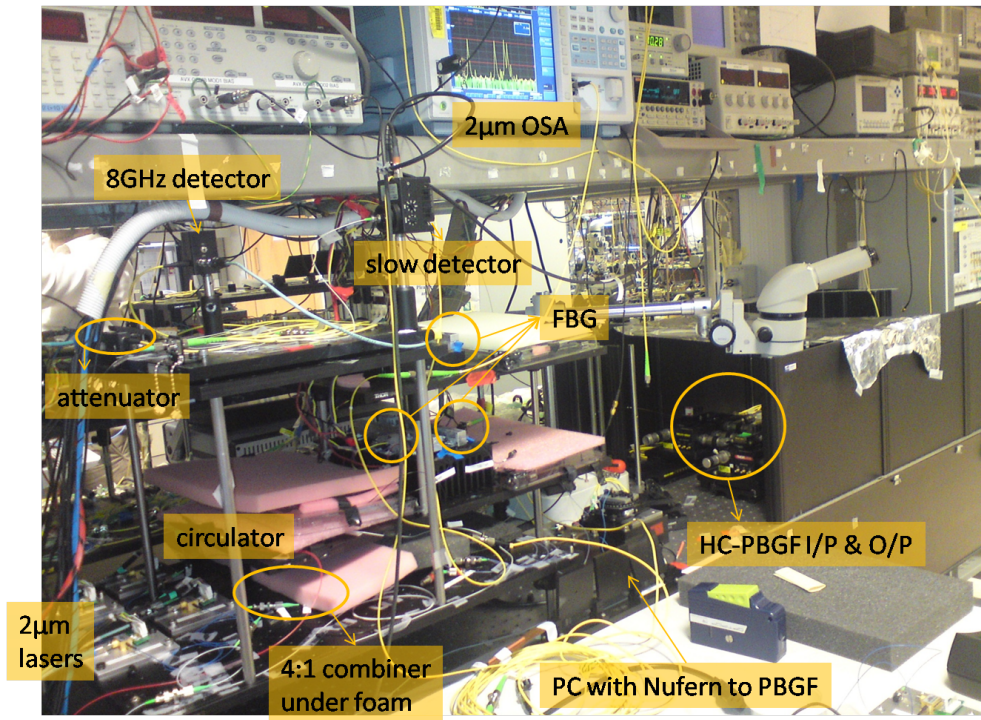


Figure 5.21: Picture of experimental setup with visible components labelled.

each of the 128 subcarriers increased the capacity of each directly modulated laser to 5 Gbit/s. Two independent outputs and one complementary output of an Arbitrary Waveform Generator, operating at 12 GS/s, were used to repeatedly transmit 7 de-correlated frames, containing 100 data symbols, preceded by one training symbol for synchronization [163].

The transmitter was divided into two separate bit rates. The 2004.79, 2004.27 and 1997.64nm channels were directly modulated using BPSK Fast-OFDM at 5Gbit/s, while the externally modulated channel was encoded using NRZ OOK at 8.5Gbit/s. This mixed format transmitter was then connected to fifty metres of Nufern solid core fibre. The fibre had a loss  $\approx 4.2\text{dB}$ , dominated by splicing losses to SMF fibre pigtailed with an estimated 2 dB loss per splice. The pigtailed fifty metre spool allowed for simple insertion and removal between the transmitter and receiver. At the output the signal was pre-amplified by the TDFA. From there the system remained the same as Figure 5.17, consisting of a filtering system, optical taps for monitoring received power and a high speed detector. Once the optical signal was returned to the electrical domain it was amplified, using a standard 12GHz RF amplifier with 9dB gain. From there a PRBS error detector was used to recover the data, in the case of the externally modulated channel. For the directly modulated channels, encoded with BPSK Fast-OFDM data, the data was recovered using a real time oscilloscope (12GHz 50GS/s) and offline digital signal processing.

The  $2\mu\text{m}$  WDM subsystem was analysed in terms of its bit error rate (BER) perfor-



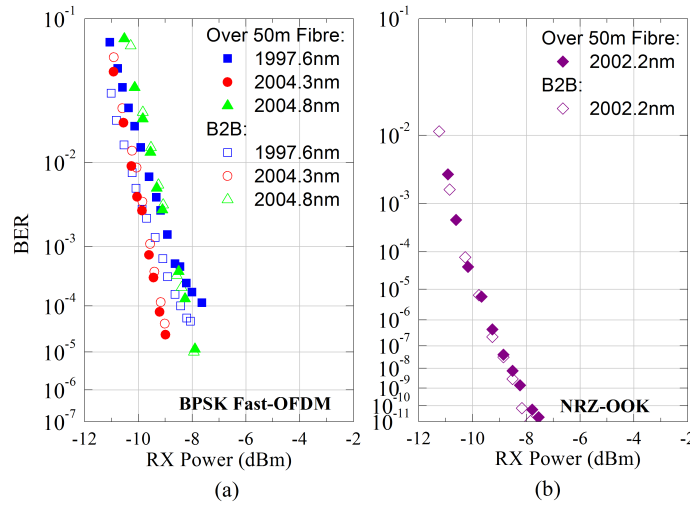


Figure 5.22: BER measurements as a function of received power for (a) directly modulated BPSK Fast-OFDM channels and (b) externally modulated NRZ OOK channel for back-to-back (open symbols) and over 50m solid core Nufern fibre (solid symbols)

mance either at back-to-back, or after 50m of a solid core single mode fibre with a total input power below 3dBm. The results in Figure 5.22(a) show that the 5 Gbit/s directly modulated BPSK Fast-OFDM channels gave receiver sensitivities at  $1 \times 10^{-3}$  of -8.5dBm or below, with a spread of less than 1dB between channels at this BER. This 1dB spread is likely due to the coupling losses between ports from the 4:1 combiner, and the slight tilt on the amplifier gain over this wavelength region ( $\sim 2$  dB across the range of wavelengths in use). For the NRZ-OOK externally modulated channel (Figure 5.22(b)), error-free performance was achieved, with a receiver sensitivity of -10.7dBm also at a BER of  $1 \times 10^{-3}$ .

Less than 0.5dB penalty was observed after the fifty metres of fibre for all four channels, indicating that longer fibre lengths should be readily achieved. Figure 5.23 shows open eye diagrams and clear constellations for two channels after 50 m of fibre, showing that no additional penalty is observed after fibre transmission.

This work shows, for the first time, the direct implementation of a telecommunications grade optical subsystem at 2  $\mu$ m. These are promising results that show the first generation of components at 2  $\mu$ m have the basic functionality required for creating an optical link at 2  $\mu$ m.

### 5.3.2 Transmission Over Hollow Core Fibre

For transmission over the fibre it was first necessary to couple light in out of the fibre, this was done by "butt-coupling" SMF to either end of the HC-PBGF, using *xyz* stages to control alignment of the fibres. This allowed manual tuning to maximise the

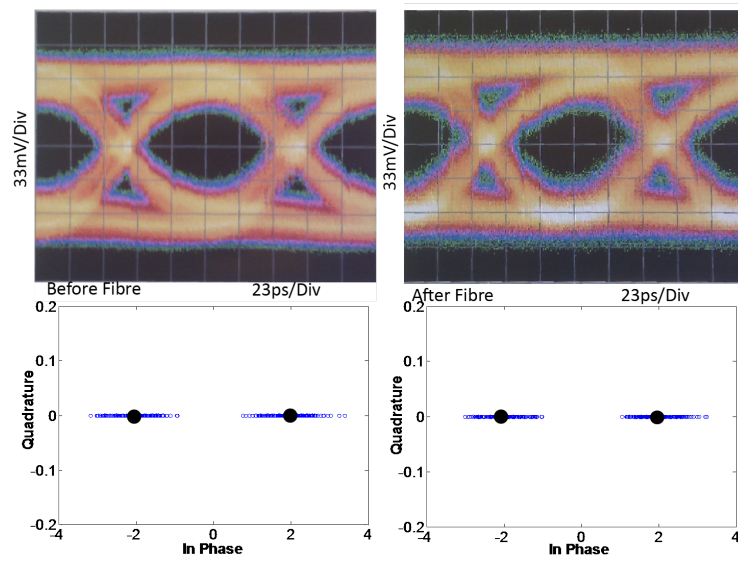


Figure 5.23: Eye diagram of externally modulated channel (top row) before (left) and after (right) transmission. Bottom row shows constellation diagram for a directly modulated BPSK Fast-OFDM channel before (left) and after (right) transmission.

extinction ratio between other modes supported by the fibre, while at the same time avoiding the relatively large splice losses of splicing solid core SMF to a HC-PBGF with mismatched core diameters. The channel link (Figure 5.17(b)) had  $\approx 10\text{dB}$  loss and was dominated by coupling losses ( $\approx 4\text{dB}$ ) at either end. Since these initial investigations there has been considerable work on improving the quality of SMF to HC-PBGF splicing and hollow core to hollow core splicing [164]. This shows great promise for reducing excess loss in transmitter and receiver components. It may also help, in the short term, to provide HC-PBGF lengths in the order of kilometres.

The transmitter was divided into two separate bit rates. The 2004.79, 2004.27 and 1997.64nm channels were directly modulated using NRZ OOK at 2.5Gbit/s instead of BPSK Fast-OFDM. This decision was made due to the constraint of offline processing and the difficulty of aligning the fibre. By using OOK it was possible to continuously monitor the BER and recognise system drifts, such as drifting in the butt coupling alignment. The 2002.22nm channel was directly modulated at a bit rate of 8.5Gbit/s. The performance of the system was analysed by measuring bit error rates for both back-to-back and over 290 meters of HC-PBGF. The results of these measurements can be viewed in Figure 5.24 for each of the four WDM channels. Error free transmission was achieved for all channels in both the direct and externally modulated cases. For the externally modulated channel (Figure 5.24(b)), there was a negligible transmission penalty when transmitting over fibre, with receiver sensitivity below  $-10.5\text{ dBm}$  at a BER of  $1 \times 10^{-3}$ . The eye diagram after transmission for the externally modulated channel can be seen in Figure 5.25(b) with slight patterning due to the bit rate being on the limit of the detector's frequency response. This was deemed an acceptable penalty to achieve a higher bit-rate and the patterning can be removed by reducing the bit-rate.

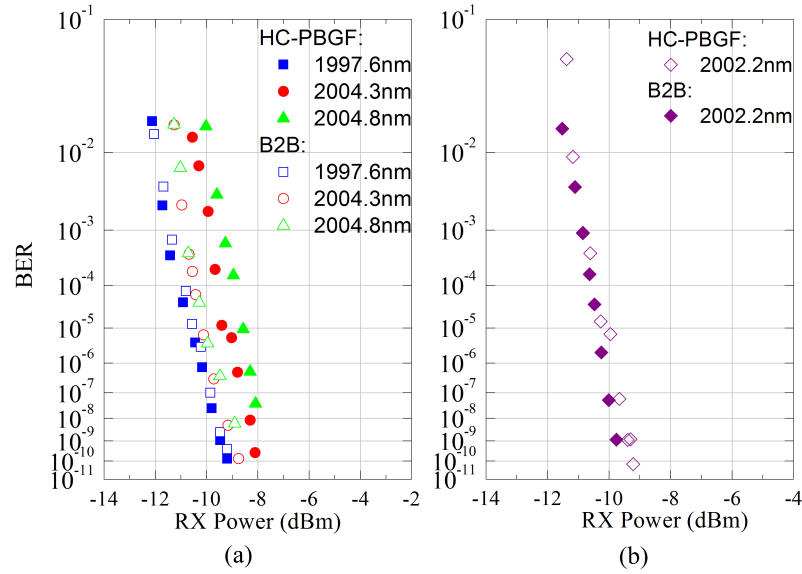


Figure 5.24: Bit error rate results for directly modulated (a) and externally modulated channels (b) for back-to-back (open symbols) and over 290 metres HC-PBGF (closed symbols).

For the directly modulated channels receiver sensitivities of  $-10.3\text{dBm}$  and less were achieved for each wavelength, after transmission, at a  $\text{BER}$  of  $1 \times 10^{-3}$ , as shown in Figure 5.24(a). The bias currents of the lasers were adjusted for optimum BER after transmission. A maximum sensitivity penalty of  $1.3\text{dB}$  was observed when transmitting over fibre compared to back-to-back. The channel requiring the highest receiver sensitivity ( $2004.79\text{ nm}$  see Figure 5.25(a)) corresponds to the laser with the lowest SMSR. Figure 5.25(c) shows the eye diagram of the  $2004.79\text{ nm}$  channel before transmission, showing large overshoot, possibly due to mode partition noise and reflected light from the 4:1 combiner. This coupled with a slight detuning or reduction in extinction ratio of the receiver filter would allow more noise to the receiver, with dispersion exacerbating the effect. Repeated experiments were unable to match the back-to-back performance achieved in Figure 5.24(a) indicating that the Bragg grating may have been damaged, potentially due to over-cooling.

These results constitute the first direct implementation of a WDM fibre based system operating at a transmission wavelength of  $2\mu\text{m}$ .

These measurements constitute a proof of principle and are currently limited by the complexities of integrating the HC-PBGF into the system and the limitations of available components.

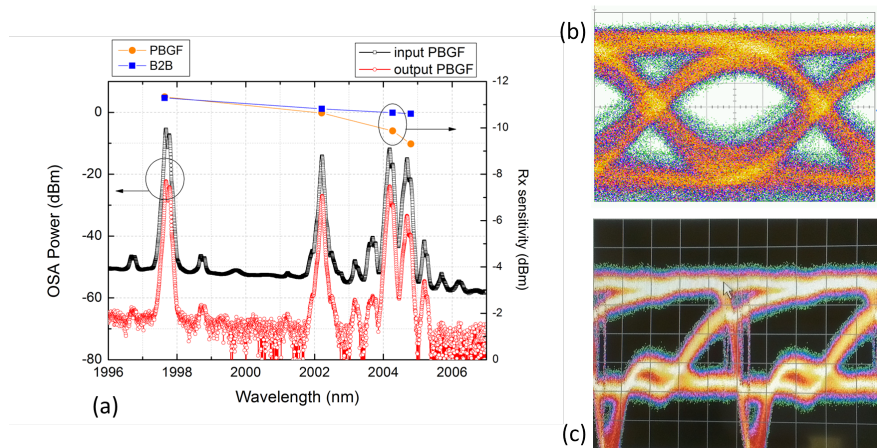


Figure 5.25: (a) Spectrum of all four channels before (black) and after (red) transmission. (b) Eye diagram of externally modulated channel after transmission. (c) Eye diagram of directly modulated channel at 2004.79 nm.

## 5.4 Chapter Summary

This chapter investigated the benefits of hollow core photonic band-gap fibre and the challenge of transmission at the predicted low loss minima of 2  $\mu$ m.

Many of the enabling technologies were discussed, including the development of a high speed (10 GHz) detector and 2  $\mu$ m lasers. A proof of principle experiment demonstrated the world's first subsystem implemented directly at the 2  $\mu$ m wavelength utilising a mixed format WDM system with a total capacity of 23.5 Gbit/s. This was followed by a second demonstration, the first ever WDM transmission over 290 m of hollow core photonic band-gap fibre at 2  $\mu$ m.

Despite the promising results and successful proof of principle experiments there are several areas where improvements could be made. Future work could develop more advanced modulators capable of generating IQ modulation formats. This will require further development of components to allow coherent detection. Development of second generation lasers could improve frequency response to allow for greater bandwidth when directly modulating. More development on all components including couplers and filters will insure that systems at 2  $\mu$ m can become a reality. This work has shown that such subsystems are possible with the ability to produce ultra-low loss fibres at significant ultimately determining the viability of such systems.

## Chapter 6

# Conclusions

*"So we beat on, boats against the current, borne back ceaselessly into the past."*

F. Scott Fitzgerald

This thesis investigated some of the potential solutions for delivering high capacity digital communications and hoped to contribute, in some way, to designing the optical communications system of the future. To do this the thesis was broken into two main parts. One part investigated future improvements to SMF while the remainder of the thesis made a thorough examination into new fibre technology. The progress of both respective tracks will now be reviewed.

### 6.1 Future Improvements in SMF

As mentioned at the start of the thesis, there are several approaches to increasing the capacity of current SMF, varying from high spectral efficiency systems utilising advanced wavelength division multiplexing techniques [16], to compensation techniques such as digital back propagation [17] and optical phase conjugation [18] that aim to compensate for fibre transmission impairments. This thesis studied the efficiency of modulation formats and implementing a power efficient modulation format that uses the entire signal space for modulation, enabling a higher overall efficiency per bit in a SMF.

These advanced modulation formats, that target efficient use of the signal space to achieve greater nonlinear tolerance, were covered in Chapter 3. The chapter began by investigating new techniques to view multidimensional modulation formats with a view to having an efficient visual representation of the signal, similar to the constellation diagram. The four dimensions of a dual-polarisation wave were defined as the absolute amplitude and phase with the second polarisation adding two additional degrees of freedom, relative amplitude and phase. A visualisation technique known as stereographic projection was introduced and applied to modulation formats for the first time, to the authors knowledge. It is hoped that future work using

the visualisation techniques presented could extend the stereographic projection approach to higher degrees of freedom, such as frequency or space. After the visualisation techniques were introduced the power saving of advanced modulation formats was discussed. This was done by comparing spectral efficiency to asymptotic power efficiency, the former a metric of how many bits a modulation format can convey and the latter a metric of energy required per bit. The trade off between the two showed that simplexes were the most efficient in two and three dimensions while a new triadic modulation format, referred to as PS-QPSK was found to have the optimum trade-off in four dimensions.

An experimental demonstration of the PS-QPSK format in a typical terrestrial WDM system was then presented and compared with the performance of polarisation-multiplexed QPSK at the same bit rate of 40.5 Gb/s. PS-QPSK and DP-QPSK were compared for a single-channel, back-to-back configuration, and for  $10 \times 100$  km WDM transmission over standard SMF with 50 GHz-spaced neighbour channels of the same modulation format. The results demonstrate compelling advantages of PS-QPSK over DP-QPSK, including 0.9 dB sensitivity improvement for back-to-back (at  $10^{-3}$  BER) assuming conventional hard-decision forward-error-correction and up to 1.6 dB higher launch power tolerance for a 1 dB penalty in required OSNR relative to back-to-back. Thus, PS-QPSK has shown some promising results to extend the functionality of current SMF. However, modulation formats such as DP-QPSK and 16-QAM do have higher spectral efficiencies and it is possible that these formats will be required for providing higher capacity at the expense of higher energy consumption and potentially lower reach due to nonlinearities. However, PS-QPSK is only one particular power efficient modulation format and by using similar approaches it should be possible to design highly efficient dual polarisation modulation formats that deliver high spectral efficiency at an optimum power efficiency.

## 6.2 Advantages of New Fibre Technology

Moving beyond transmitter and receiver design presented in Chapter 3 the thesis turns to discuss the possible benefits of using new fibres that have a higher power threshold that are envisioned to have far fewer nonlinear Kerr effects and thus the potential for higher capacity systems. This thesis set out to experimentally investigate the nonlinear advantages of few-mode fibres and the potential capacity increase as a result of using multi-mode transmission.

Chapter 4 starts by studying the benefits of multi-mode and few-mode fibre that has lead them to be a fruitful research topic in optical communications of late, with many high-profile examples [38, 96]. In order to estimate the overall advantage of few-mode fibres compared to single mode fibre several experiments were carried out to com-

pare the nonlinear performance of FMF. The nonlinear limit was of interest as it is at this point that nonlinear fibre impairments begin to dominate and limit transmission capacity (assuming the most efficient encoding has been employed, as discussed in Chapter 3). Several nonlinear effects were studied including stimulated Brillouin scattering, self phase modulation and four wave mixing. For stimulated Brillouin scattering experimental measurements confirmed that SBS is present in FMF where the basic effect is the same as the SMF case, due to the silica core in both fibres. The major difference between SMF and FMF is the considerably larger acoustic effective area, due to the larger core.

Investigations into self-phase modulation in FMF were presented that showed experimental work that successfully demonstrated self-phase modulation in FMF. The experiments showed that there were clear effects of dispersion and SPM in individual modes of a FMF with the results compared to current numerical models that neglect inter-mode effects. It was found that such models remain useful for estimating performance, for accurate modelling additional effects should be included.

Another set of experimental techniques were presented in Chapter 4 to investigate the affect of inter-mode effects in greater detail. This lead to investigations into four-wave-mixing in FMF where intra- and inter-mode four wave mixing were isolated. The results were compared to a model that included both intra- and inter-mode FWM confirming both the presence of inter-mode FWM and the accuracy of the numerical model. It was found, for the particular fibre under investigation, that there was a 3 dB increase in FWM signal compared to what would be expected from intra-mode FWM alone.

From the experimental measurements carried out to estimate the nonlinear effects in FMF and experimentally verifying closed form expressions for FWM it was possible to use this FWM model to calculate the lower-bound capacity limit of few-mode fibres. It was found, for the fibre in use for the FWM experiments, that inter-mode FWM reduced the overall capacity of the FMF. For the fibre in question it was found that each mode had a capacity limit similar to a SMF, indicating that there is a linear growth in overall capacity as the number of fibre modes increases. Depending on how additional modes are added (by increasing or decreasing the deferential mode delay between the fastest and slowest modes), inter-mode four-wave mixing has the potential to reduce the capacity of each mode as additional modes are added to the fibre.

Chapter 5 investigated another radically new fibre, hollow-core photonic band-gap fibre and the engineering challenges that go with it. The impact of additional bandwidth, coupled with the potential of higher nonlinear thresholds, offers an exciting and radical approach to overcome the capacity limits of today's systems. The chapter examined the possible scenario where hollow core fibre can be manufactured at low-loss and high yield. In this scenario the preferred low-loss window would be at 2  $\mu\text{m}$ .

Chapter 5 studied the requirements of any subsystems and the challenges in moving to another transmission window. The chapter covered the development of essential components to unlock the 2  $\mu\text{m}$  window.

Many of the critical components are feasible with components such as Thulium doped fibre amplifiers and 2  $\mu\text{m}$  lasers already developed. The development of a high speed detector was presented along with characterisation of various components such as fibre Bragg gratings used for filtering at 2  $\mu\text{m}$ . The thesis culminates in the construction of the world's first WDM subsystem operating at 2  $\mu\text{m}$ . The system was then used to transmit 16 GHz over 290 m of hollow core fibre using direct detection. This work shows that subsystems at 2  $\mu\text{m}$  are feasible.

The viability of 2  $\mu\text{m}$  for optical transmission is ultimately dependant on the availability of low-loss fibre with a loss minima at 2  $\mu\text{m}$ . At the moment fibre technology is still under development with noteworthy reductions in loss noted in Chapter 5. However, hollow core fibre has not yet matched the performance and scalability of standard single mode fibre. Systems utilising hollow core fibre are unlikely to be deployed in the near term with the maturity of components at 1.5  $\mu\text{m}$  favouring the more readily scalable few-mode fibres. As was seen in this thesis, there is a benefit to using few-mode fibre but the margins to increase capacity are not as large as initially anticipated.

As Chapter 1 has shown, the future of such technologies will ultimately be decided by their cost benefit. It may well prove to be more beneficial to remain using single mode fibre where efficiency will become crucial. Whether future optical communication systems continue to use standard single-mode fibre of the present day or a radically new fibre is deployed, it is hoped that the work presented in this thesis will contribute, in some small way, to the optical communication solutions of the future.



# References

- [1] Claude Elwood Shannon. A mathematical theory of communication. *The Bell System Technical Journal*, 27:379–423, 1948.
- [2] Partha P Mitra and Jason B Stark. Nonlinear limits to the information capacity of optical fibre communications. *Nature*, 411(6841):1027–1030, 2001.
- [3] René-Jean Essiambre, Gerard Foschini, Peter Winzer, and Gerhard Kramer. Capacity limits of fiber-optic communication systems. In *Optical Fiber Communication Conference and National Fiber Optic Engineers Conference*, page OThL1. Optical Society of America, 2009.
- [4] Andrew D. Ellis, Jian Zhao, and David Cotter. Approaching the non-linear shannon limit. *J. Lightwave Technol.*, 28(4):423–433, Feb 2010.
- [5] "Universal Postal Union". [www.upu.int](http://www.upu.int). Accessed on 15 Oct 2013. <http://www.upu.int/en/the-upu/history/about-history.html>.
- [6] Gregory Clark. Lifestyles of the rich and famous: Living costs of the rich versus the poor in england, 1209-1869, paper presented in conference, towards a global history of prices and wages (2004). *Paper presented in conference, Towards a global history of prices and wages (2004)*, 2004.
- [7] Jeremiah E. Dittmar. Information technology and economic change: The impact of the printing press. *The Quarterly Journal of Economics*, 126(3):1133–1172, 2011.
- [8] Professor David Edward Hughes. Prof. d. e. hughes's research in wireless telegraphy. *The Electrician*, pages 40–41, May 5 1899.
- [9] J.E. Brittain. Electrical engineering hall of fame: Guglielmo marconi. *Proceedings of the IEEE*, 92(9):1501–1504, 2004.
- [10] Kenneth D. Garbade and William L. Silber. Technology, communication and the performance of financial markets: 1840-1975. *The Journal of Finance*, 33(3):pp. 819–832, 1978.
- [11] Dale W. Jorgenson, Mun S. Ho, Jon D. Samuels, and Kevin J. Stiroh. Industry origins of the american productivity resurgence. *Economic Systems Research*, 19(3):229–252, 2007.

- [12] "The State of Broadband 2013: Universalizing Broadband", Commissioned by the United Nations. Accessed on 9 Nov 2013. <http://www.broadbandcommission.org/Documents/bb-annualreport2013.pdf>.
- [13] "The Zettabyte Era Trends and Analysis", Cisco white paper 2012-2017. Accessed on 9 Nov 2013. [http://www.cisco.com/en/US/solutions/collateral/ns341/ns525/ns537/ns705/ns827/VNI\\_Hyperconnectivity\\_WP.html](http://www.cisco.com/en/US/solutions/collateral/ns341/ns525/ns537/ns705/ns827/VNI_Hyperconnectivity_WP.html).
- [14] "ICT Facts and Figures 2013". Accessed on 9 Nov 2013. <http://www.itu.int/en/ITU-D/Statistics/Documents/facts/ICTFactsFigures2013.pdf>.
- [15] "Internet World Stats". Accessed on 9 Nov 2013. <http://www.internetworldstats.com/stats.htm>.
- [16] Paola Frascella. *High-Capacity Direct Detection Coherent WDM*. PhD thesis, University College Cork, 2011.
- [17] Danish Rafique. *Electronic Signal Processing in Optical Communications: Analysis and Applications of Nonlinear Transmission Limits*. PhD thesis, University College Cork, 2012.
- [18] Xiang Liu, AR Chraplyvy, PJ Winzer, RW Tkach, and S Chandrasekhar. Phase-conjugated twin waves for communication beyond the kerr nonlinearity limit. *Nature Photonics*, 2013.
- [19] E. Snitzer. Cylindrical dielectric waveguide modes. *J. Opt. Soc. Am.*, 51(5):491–498, May 1961.
- [20] John M Senior and M Yousif Jamro. *Optical fiber communications: principles and practice*. Pearson Education, 2009.
- [21] Dt Gloge. Dispersion in weakly guiding fibers. *Applied optics*, 10(11):2442–2445, 1971.
- [22] Robert Manning. Introduction to lasers and photonics. Department of Physics, University College Cork, 2012.
- [23] Govind P Agrawal. *Fiber-optic communication systems*. John Wiley & Sons, 4th edition, 2010.
- [24] Rajiv Ramaswami, Kumar Sivarajan, and Galen Sasaki. *Optical networks: a practical perspective*. Morgan Kaufmann, 2009.
- [25] F Poletti, NV Wheeler, MN Petrovich, N Baddela, E Numkam Fokoua, JR Hayes, DR Gray, Z Li, R Slavík, and DJ Richardson. Towards high-capacity fibre-optic

- communications at the speed of light in vacuum. *Nature Photonics*, 7(4):279–284, 2013.
- [26] J. C. Knight, J. Broeng, T. A. Birks, and P. St. J. Russell. Photonic band gap guidance in optical fibers. *Science*, 282(5393):1476–1478, 1998.
- [27] F Benabid. Hollow-core photonic bandgap fibre: new light guidance for new science and technology. *Philosophical Transactions of the Royal Society A: Mathematical, Physical and Engineering Sciences*, 364(1849):3439–3462, 2006.
- [28] Francesco Poletti. *Direct and inverse design of microstructured optical fibres*. PhD thesis, University of Southampton, Faculty of Engineering, Science and Mathematics, Optoelectronics Research Centre, 2007.
- [29] "The Nobel Prize in Physics 2009". Nobelprize.org. Nobel Media AB 2013. Web. 5 Sep 2013. [http://www.nobelprize.org/nobel\\_prizes/physics/laureates/2009/](http://www.nobelprize.org/nobel_prizes/physics/laureates/2009/).
- [30] Tetsuo Miya, Y Terunuma, T Hosaka, and Tadashi Miyashita. Ultimate low-loss single-mode fibre at 1.55  $\mu\text{m}$ . *Electronics Letters*, 15(4):106–108, 1979.
- [31] T. Izawa, N. Shibata, and A. Takeda. Optical attenuation in pure and doped fused silica in the ir wavelength region. *Applied Physics Letters*, 31(1):33–35, 1977.
- [32] Nicole Levy. Ultraviolet analysis of graded-index lightguide preforms. *Appl. Opt.*, 20(3):460–464, Feb 1981.
- [33] P. C Schultz. Ultraviolet absorption of titanium and germanium in fused silica. In *International Congresses On Glass*, 1962.
- [34] M. Hirano, T. Haruna, Y. Tamura, T. Kawano, S. Ohnuki, Y. Yamamoto, Y. Koyano, and T. Sasaki. Record low loss, record high fom optical fiber with manufacturable process. In *Optical Fiber Communication Conference and Exposition and the National Fiber Optic Engineers Conference (OFC/NFOEC)*, 2013, pages 1–3, 2013.
- [35] R. Olshansky. Propagation in glass optical waveguides. *Rev. Mod. Phys.*, 51:341–367, Apr 1979.
- [36] Andrew D. Ellis. *All Optical Networking Beyond 10 Gbit/s; OTDM Networks Based on Electro-Optic Modulators and Fibre Ring Lasers*. PhD thesis, University of Aston in Birmingham, 1997.
- [37] C. Wree, N. Hecker-Denschlag, E. Gottwald, P. Krummrich, J. Leibrich, E.-D. Schmidt, B. Lankl, and W. Rosenkranz. High spectral efficiency 1.6-b/s/hz transmission (8 x 40 gb/s with a 25-ghz grid) over 200-km ssmf using rz-dqpsk and polarization multiplexing. *Photonics Technology Letters, IEEE*, 15(9):1303–1305, 2003.

- [38] V.A.J.M. Sleiffer, Y. Jung, V. Veljanovski, R.G.H. van Uden, M. Kuschnerov, H. Chen, B. Inan, L. Grüner Nielsen, Y. Sun, D.J. Richardson, S.U. Alam, F. Poletti, J.K. Sahu, A. Dhar, A.M.J. Koonen, B. Corbett, R. Winfield, A.D. Ellis, and H. de Waardt. 73.7 tb/s ( $96 \times 3 \times 256$ -gb/s) mode-division-multiplexed dp-16qam transmission with inline mm-edfa. *Opt. Express*, 20(26):B428–B438, Dec 2012.
- [39] Sebastian Randel, Roland Ryf, Alberto Sierra, Peter J. Winzer, Alan H. Gnauck, Cristian A. Bolle, René-Jean Essiambre, David W. Peckham, Alan McCurdy, and Robert Lingle. 6×56-gb/s mode-division multiplexed transmission over 33-km few-mode fiber enabled by 6×6 mimo equalization. *Opt. Express*, 19(17):16697–16707, Aug 2011.
- [40] J. Carpenter, B.C. Thomsen, and T.D. Wilkinson. Degenerate mode-group division multiplexing. *Lightwave Technology, Journal of*, 30(24):3946–3952, 2012.
- [41] Karsten Rottwitt, Jake Bromage, Andrew J Stentz, Lufeng Leng, Malcolm E Lines, and Henrik Smith. Scaling of the raman gain coefficient: Applications to germanosilicate fibers. *Journal of lightwave technology*, 21(7):1652, 2003.
- [42] Andrey Kobayakov, Michael Sauer, and Dipak Chowdhury. Stimulated brillouin scattering in optical fibers. *Advances in optics and photonics*, 2(1):1–59, 2010.
- [43] D Cotter. Stimulated brillouin scattering in monomode optical fiber. *Journal of Optical Communications*, 4(1):10–19, 1983.
- [44] FW Willems, W Muys, and JS Leong. Simultaneous suppression of stimulated brillouin scattering and interferometric noise in externally modulated lightwave am-scm systems. *Photonics Technology Letters, IEEE*, 6(12):1476–1478, 1994.
- [45] John Kerr. XI. a new relation between electricity and light: Dielectrified media birefringent. *The London, Edinburgh, and Dublin Philosophical Magazine and Journal of Science*, 50(332):337–348, 1875.
- [46] Akira Hasegawa. *Optical Solitons in Fibers*. Springer-Verlag, 2nd edition, 1990.
- [47] Govind Agrawal. *Nonlinear Fiber Optics*. Academic Press, 3rd edition, 2001.
- [48] Regan T Watts. *Novel Diagnostic Technologies for Optical Communication Systems*. PhD thesis, University of Auckland, 2008.
- [49] J. Toulouse. Optical nonlinearities in fibers: review, recent examples, and systems applications. *Lightwave Technology, Journal of*, 23(11):3625–3641, 2005.
- [50] Shiva Kumar. *Impact of nonlinearities on fiber optic communications*, volume 7. Springer, 2011.
- [51] Xi Chen and William Shieh. Closed-form expressions for nonlinear transmission

- performance of densely spaced coherent optical ofdm systems. *Opt. Express*, 18(18):19039–19054, Aug 2010.
- [52] P. Poggiolini, A. Carena, V. Curri, G. Bosco, and F. Forghieri. Analytical modeling of nonlinear propagation in uncompensated optical transmission links. *Photonics Technology Letters, IEEE*, 23(11):742–744, 2011.
- [53] Noam Ophir, Ryan K. W. Lau, Michael Menard, Xiaoliang Zhu, Kishore Padmaraju, Yoshitomo Okawachi, Reza Salem, Michal Lipson, Alexander L. Gaeta, and Keren Bergman. Wavelength conversion and unicast of 10-gb/s data spanning up to 700 nm using a silicon nanowaveguide. *Opt. Express*, 20(6):6488–6495, Mar 2012.
- [54] Ruwan Weerasuriya, Stylianos Sygletos, Selwan K Ibrahim, Richard Phelan, John O Carroll, Brian Kelly, James O’Gorman, and Andrew D Ellis. Generation of frequency symmetric signals from a bpsk input for phase sensitive amplification. In *Optical Fiber Communication Conference*. Optical Society of America, 2010.
- [55] Nadir Dagli. Wide-bandwidth lasers and modulators for rf photonics. *Microwave Theory and Techniques, IEEE Transactions on*, 47(7):1151–1171, 1999.
- [56] F. Koyama and K. Iga. Frequency chirping in external modulators. *Lightwave Technology, Journal of*, 6(1):87–93, 1988.
- [57] David G. Moodie, Andrew D. Ellis, Xin Chen, Fatima C. Garcia, David C. Rogers, Simon D. Perrin, Paul J. Cannard, Robert I. McLaughlin, Mike J. Robertson, Sean Amos, Simon Cole, Colin W. Ford, and Ian Reid. Applications of electroabsorption modulators in high bit-rate extended reach transmission systems. In *Optical Fiber Communication Conference*, page TuP1. Optical Society of America, 2003.
- [58] A.H. Gnauck and P.J. Winzer. Optical phase-shift-keyed transmission. *Lightwave Technology, Journal of*, 23(1):115–130, 2005.
- [59] P.J. Winzer and R. J Essiambre. Advanced modulation formats for high-capacity optical transport networks. *Lightwave Technology, Journal of*, 24(12):4711–4728, 2006.
- [60] R.A. Griffin and A.C. Carter. Optical differential quadrature phase-shift key (odqpsk) for high capacity optical transmission. In *Optical Fiber Communication Conference and Exhibit, 2002. OFC 2002*, pages 367–368, 2002.
- [61] H. Nyquist. Certain factors affecting telegraph speed. *American Institute of Electrical Engineers, Transactions of the*, XLIII:412–422, 1924.

- [62] Claude Shannon and Warren Weaver. *The Mathematical Theory of Communication*. University of Illinois Press, 1949.
- [63] Stamatios V Kartalopoulos. *Optical bit error rate: an estimation methodology*, volume 1. Wiley, 2004.
- [64] R. Essiambre, G. Kramer, P.J. Winzer, G.J. Foschini, and B. Goebel. Capacity limits of optical fiber networks. *Lightwave Technology, Journal of*, 28(4):662–701, 2010.
- [65] A. D. Ellis. The nonlinear shannon limit and the need for new fibres. *Proc. SPIE*, 8434:84340H–84340H–10, 2012.
- [66] Rene-Jean Essiambre. Overview of the nonlinear shannon limit for optical fibers. In *Latin America Optics and Photonics Conference*, page LM1C.1. Optical Society of America, 2012.
- [67] Magnus Karlsson and Erik Agrell. Which is the most power-efficient modulation format in optical links? *Opt. Express*, 17(13):10814–10819, Jun 2009.
- [68] E. Agrell and M. Karlsson. Power-efficient modulation formats in coherent transmission systems. *Lightwave Technology, Journal of*, 27(22):5115–5126, 2009.
- [69] Henning Bülow. Polarization qam modulation (pol-qam) for coherent detection schemes. In *Optical Fiber Communication Conference and National Fiber Optic Engineers Conference*, page OWG2. Optical Society of America, 2009.
- [70] Pal Roe Sundsoy. *Depolarization of orthogonal states of polarization in fiber optic high-speed transmission*. PhD thesis, NTNU, Trondheim, 2004.
- [71] R. Clark Jones. A new calculus for the treatment of optical systems. *J. Opt. Soc. Am.*, 31(7):488–493, Jul 1941.
- [72] Magnus Karlsson and Erik Agrell. Power-efficient modulation schemes. In Shiva Kumar, editor, *Impact of Nonlinearities on Fiber Optic Communications*, volume 7 of *Optical and Fiber Communications Reports*, pages 219–252. Springer New York, 2011.
- [73] E. Agrell and M. Karlsson. On the symbol error probability of regular polytopes. *Information Theory, IEEE Transactions on*, 57(6):3411–3415, 2010.
- [74] Masoud Proakis, John G.; Saleni. *Digital Communications, Fifth Edition*. Mc Graw Hill, 2008.
- [75] Wu-Yi Hsiang. On the sphere packing problem and the proof of kepler’s conjecture. *International Journal of Mathematics*, 4(05):739–831, 1993.
- [76] P. Poggiolini, G. Bosco, A. Carena, V. Curri, and F. Forghieri. Performance eval-

- uation of coherent wdm ps-qpsk (hexa) accounting for non-linear fiber propagation effects. *Opt. Express*, 18(11):11360–11371, May 2010.
- [77] P. Serena, A. Vannucci, and A. Bononi. The performance of polarization switched-qpsk (ps-qpsk) in dispersion managed wdm transmissions. In *Optical Communication (ECOC), 2010 36th European Conference and Exhibition on*, pages 1–3, 2010.
- [78] S. Benedetto and P. Poggiolini. Theory of polarization shift keying modulation. *Communications, IEEE Transactions on*, 40(4):708–721, 1992.
- [79] S. Betti, F. Curti, G. De Marchis, and E. Iannone. A novel multilevel coherent optical system: 4-quadrature signaling. *Lightwave Technology, Journal of*, 9(4):514–523, 1991.
- [80] S. Betti, G. De Marchis, E. Iannone, and P. Lazzaro. Homodyne optical coherent systems based on polarization modulation. *Lightwave Technology, Journal of*, 9(10):1314–1320, 1991.
- [81] Ekaterina S. Masalkina, Roman Dischler, and Henning Buelow. Experimental study of polarization-switched-qpsk subcarrier modulation and iterative demapping on optical ofdm systems. In *Optical Fiber Communication Conference/National Fiber Optic Engineers Conference 2011*, page OThO6. Optical Society of America, 2011.
- [82] Martin Sjödin, Pontus Johannisson, Henk Wymeersch, Peter A. Andrekson, and Magnus Karlsson. Comparison of polarization-switched qpsk and polarization-multiplexed qpsk at 30 gbit/s. *Opt. Express*, 19(8):7839–7846, Apr 2011.
- [83] Pontus Johannisson, Martin Sjödin, Magnus Karlsson, Henk Wymeersch, Erik Agrell, and Peter A. Andrekson. Modified constant modulus algorithm for polarization-switched qpsk. *Opt. Express*, 19(8):7734–7741, Apr 2011.
- [84] L. E. Nelson, X. Zhou, N. Mac Suibhne, A. D. Ellis, and P. Magill. Experimental comparison of coherent polarization-switched qpsk to polarization-multiplexed qpsk for  $10 \times 100$  km wdm transmission. *Opt. Express*, 19(11):10849–10856, May 2011.
- [85] Johannes Karl Fischer, Saleem Alreesh, Robert Elschner, Felix Frey, Christian Meuer, Lutz Molle, Carsten Schmidt-Langhorst, Takahito Tanimura, and Colja Schubert. Experimental investigation of 126-gb/s 6pol-sk-qpsk signals. *Opt. Express*, 20(26):B232–B237, Dec 2012.
- [86] J.K. Fischer, S. Alreesh, T. Tanimura, R. Elschner, F. Frey, C. Meuer, L. Molle, C. Schmidt-Langhorst, and C. Schubert. Four-dimensional coded modulation: 6pol-sk-qpsk. In *Photonic Networks, 14. 2013 ITG Symposium. Proceedings*, pages 1–6, 2013.

- [87] David S. Millar and Seb J. Savory. Blind adaptive equalization of polarization-switched qpsk modulation. *Opt. Express*, 19(9):8533–8538, Apr 2011.
- [88] D. Godard. Self-recovering equalization and carrier tracking in two-dimensional data communication systems. *Communications, IEEE Transactions on*, 28(11):1867–1875, 1980.
- [89] Xiang Zhou, Jianjun Yu, and Peter Magill. Cascaded two-modulus algorithm for blind polarization de-multiplexing of 114-gb/s pdm-8qam optical signals. In *Optical Fiber Communication Conference and National Fiber Optic Engineers Conference*, page OWG3. Optical Society of America, 2009.
- [90] Xiang Zhou, Jianjun Yu, Ming-Fang Huang, Yin Shao, Ting Wang, Lynn Nelson, Peter Magill, Martin Birk, Peter I. Borel, David W. Peckham, Robert Lingle, and Benyuan Zhu. 64-tb/s, 8 b/s/hz, pdm-36qam transmission over 320 km using both pre- and post-transmission digital signal processing. *J. Lightwave Technol.*, 29(4):571–577, Feb 2011.
- [91] Xiang Zhou. An improved feed-forward carrier recovery algorithm for coherent receivers with m-qam modulation format. *Photonics Technology Letters, IEEE*, 22(14):1051–1053, 2010.
- [92] David S. Millar, Domaniç Lavery, Sergejs Makovejs, Carsten Behrens, Benn C. Thomsen, Polina Bayvel, and Seb J. Savory. Generation and long-haul transmission of polarization-switched qpsk at 42.9 gb/s. *Opt. Express*, 19(10):9296–9302, May 2011.
- [93] Brian Krongold, Timo Pfau, Noriaki Kaneda, and SC Lee. A comparison between ps-qpsk and pdm-qpsk with equal rate and bandwidth. *Photonics Technology Letters, IEEE*, (99):1–1, 2012.
- [94] Roland Ryf, Sebastian Randel, Alan H Gnauck, Cristian Bolle, Rene-Jean Essiambre, Peter Winzer, David W Peckham, Alan McCurdy, Robert Lingle, et al. Space-division multiplexing over 10 km of three-mode fiber using coherent  $6 \times 6$  mimo processing. In *Optical Fiber Communication Conference*. Optical Society of America, 2011.
- [95] Roland Ryf, Sebastian Randel, Alan H Gnauck, Cristian Bolle, Alberto Sierra, Sami Mumtaz, Mina Esmaeelpour, Ellsworth C Burrows, R Essiambre, Peter J Winzer, et al. Mode-division multiplexing over 96 km of few-mode fiber using coherent 6< formula formulatype=. *Lightwave Technology, Journal of*, 30(4):521–531, 2012.
- [96] Peter J Winzer. Optical networking beyond wdm. *Photonics Journal, IEEE*, 4(2):647–651, 2012.
- [97] Vincent Sleiffer, Yongmin Jung, Vladimir Veljanovski, Roy van Uden, Maxim



- Kuschnerov, Qiongyue Kang, Lars Grüner-Nielsen, Yi Sun, David Richardson, Shaif-ul Alam, et al. 73.7 tb/s (96x3x256-gb/s) mode-division-multiplexed dp-16qam transmission with inline mm-edfa. In *European Conference and Exhibition on Optical Communication*. Optical Society of America, 2012.
- [98] Lars Gruner-Nielsen, Yi Sun, Jeffrey W. Nicholson, Dan Jakobsen, Robert Lingle, and Bera Palsdottir. Few mode transmission fiber with low dgd, low mode coupling and low loss. In *Optical Fiber Communication Conference*, page PDP5A.1. Optical Society of America, 2012.
- [99] Sebastian Randel, Roland Ryf, Alan Gnauck, Miguel A. Mestre, Christian Schmidt, Rene Essiambre, Peter Winzer, Roger Delbue, Peter Pupalais, Anirudh Sureka, Yi Sun, Xinli Jiang, and Robert Lingle. Mode-multiplexed 6x20-gbd qpsk transmission over 1200-km dgd-compensated few-mode fiber. In *Optical Fiber Communication Conference*, page PDP5C.5. Optical Society of America, 2012.
- [100] Dietrich Marcuse. *Theory of dielectric optical waveguides*. Access Online via Elsevier, 1974.
- [101] Bruno Crosignani and Paolo Di Porto. Soliton propagation in multimode optical fibers. *Opt. Lett.*, 6(7):329–330, Jul 1981.
- [102] P. L. Baldeck, F. Raccach, and R. R. Alfano. Observation of self-focusing in optical fibers with picosecond pulses. *Opt. Lett.*, 12(8):588–589, Aug 1987.
- [103] F. Ferreira, S. Jansen, P. Monteiro, and H. Silva. Nonlinear semi-analytical model for simulation of few-mode fiber transmission. *Photonics Technology Letters, IEEE*, 24(4):240–242, 2012.
- [104] "OFS Two Mode Graded Index". ofscatalog.specialtyphotonics.com. Accessed on 9 Oct 2013. <http://ofscatalog.specialtyphotonics.com/item/non-standard-optical-fibers/non-standard-optical-fibers-few-mode-fibers-series/two-mode-graded-index?>
- [105] Eric L. Buckland and Robert W. Boyd. Electrostrictive contribution to the intensity-dependent refractive index of optical fibers. *Opt. Lett.*, 21(15):1117–1119, Aug 1996.
- [106] A. Melloni, M. Frasca, A. Garavaglia, A. Tonini, and M. Martinelli. Direct measurement of electrostriction in optical fibers. *Opt. Lett.*, 23(9):691–693, May 1998.
- [107] RS Krishnan. Fine structure of the rayleigh line in amorphous substances. *Nature*, 165(4206):933–934, 1950.
- [108] A Boh Ruffin. Stimulated brillouin scattering: An overview of measurements,

- system impairments, and applications. In *Proc. Symp. Opt. Fiber Meas*, pages 23–28, 2004.
- [109] R. G. Smith. Optical power handling capacity of low loss optical fibers as determined by stimulated raman and brillouin scattering. *Appl. Opt.*, 11(11):2489–2494, Nov 1972.
  - [110] C McIntosh, A Yeniay, J Toulouse, and J-MP Delavaux. Stimulated brillouin scattering in dispersion-compensating fibers. *Optical Fiber Technology*, 3(2):173–176, 1997.
  - [111] A.P. Kung, A. Agarwal, D. F. Grosz, S. Banerjee, and D.N. Maywar. Analytical solution of transmission performance improvement in fiber spans with forward raman gain and its application to repeaterless systems. *Lightwave Technology, Journal of*, 23(3):1182–1188, 2005.
  - [112] P. Bayvel and P.M. Radmore. Solutions of the sbs equations in single mode optical fibres and implications for fibre transmission systems. *Electronics Letters*, 26(7):434–436, 1990.
  - [113] Andrey Kobayakov, Shiva Kumar, Dipak Chowdhury, A. Boh Ruffin, Micheal Sauer, Scott Bickham, and Raj Mishra. Design concept for optical fibers with enhanced sbs threshold. *Opt. Express*, 13(14):5338–5346, Jul 2005.
  - [114] H. Haus. Optical fiber solitons, their properties and uses. *Proceedings of the IEEE*, 81(7):970–983, 1993.
  - [115] D.J. Kane and R. Trebino. Characterization of arbitrary femtosecond pulses using frequency-resolved optical gating. *Quantum Electronics, IEEE Journal of*, 29(2):571–579, 1993.
  - [116] N.S. Bergano. Wavelength discriminator method for measuring dynamic chirp in dfb lasers. *Electronics Letters*, 24(20):1296–1297, 1988.
  - [117] C. Laverdiere, A. Fekecs, and M. Tetu. A new method for measuring time-resolved frequency chirp of high bit rate sources. *Photonics Technology Letters, IEEE*, 15(3):446–448, 2003.
  - [118] Regan T Watts, Kai Shi, and Liam P Barry. Time-resolved chirp measurement for 100gbaud test systems using an ideal frequency discriminator. *Optics Communications*, 285(8):2039–2043, 2012.
  - [119] Kenji Sato, Shoichiro Kuwahara, and Yutaka Miyamoto. Chirp characteristics of 40-gb/s directly modulated distributed-feedback laser diodes. *Journal of Light-wave technology*, 23(11):3790, 2005.
  - [120] Francesco Poletti and Peter Horak. Description of ultrashort pulse propagation in multimode optical fibers. *JOSA B*, 25(10):1645–1654, 2008.

- [121] D Gloge and EAJ Marcatili. Multimode theory of graded-core fibers. *Bell Syst. Tech. J.*, 52(9):1563–1578, 1973.
- [122] Antonio Mecozzi, Cristian Antonelli, and Mark Shtaif. Coupled manakov equations in multimode fibers with strongly coupled groups of modes. *Optics express*, 20(21):23436–23441, 2012.
- [123] D.J. Malyon, T. Widdowson, E.G. Bryant, S.F. Carter, J.V. Wright, and W.A. Stallard. Demonstration of optical pulse propagation over 10000 km of fibre using recirculating loop. *Electronics Letters*, 27(2):120–121, 1991.
- [124] Govind P Agrawal. Self-phase modulation in optical fiber communications: Good or bad? In *Lasers and Electro-Optics, 2007. CLEO 2007. Conference on*, pages 1–2. IEEE, 2007.
- [125] PV Mamyshev. All-optical data regeneration based on self-phase modulation effect. In *Optical Communication, 1998. 24th European Conference on*, volume 1, pages 475–476. IEEE, 1998.
- [126] Rogers H Stolen. Nonlinearity in fiber transmission. *Proceedings of the IEEE*, 68(10):1232–1236, 1980.
- [127] Rene-Jean Essiambre, Roland Ryf, Miquel A. Mestre, Alan H. Gnauck, Robert Tkach, Andy Chraplyvy, Sebastian Randel, Yi Sun, Xinli Jiang, and Robert Lingle. Inter-modal nonlinear interactions between well separated channels in spatially-multiplexed fiber transmission. In *European Conference and Exhibition on Optical Communication*, page Tu.1.C.4. Optical Society of America, 2012.
- [128] R. Essiambre, M.A. Mestre, R. Ryf, A.H. Gnauck, R.W. Tkach, A.R. Chraplyvy, Yi Sun, Xinli Jiang, and R. Lingle. Experimental observation of inter-modal cross-phase modulation in few-mode fibers. *Photonics Technology Letters, IEEE*, 25(6):535–538, 2013.
- [129] G. Rademacher, S. Warm, and K. Petermann. Analytical description of cross-modal nonlinear interaction in mode multiplexed multimode fibers. *Photonics Technology Letters, IEEE*, 24(21):1929–1932, 2012.
- [130] P. Poggiolini. Analytical modeling of non-linear propagation in coherent systems. In *Optical Fiber Communication Conference and Exposition and the National Fiber Optic Engineers Conference (OFC/NFOEC), 2013*, pages 1–132, 2013.
- [131] S. Mumtaz, R. Essiambre, and G.P. Agrawal. Reduction of nonlinear penalties due to linear coupling in multicore optical fibers. *Photonics Technology Letters, IEEE*, 24(18):1574–1576, 2012.
- [132] O.V. Sinkin, J. Cai, D.G. Foursa, G. Mohs, and A.N. Pilipetskii. Impact of broadband four-wave mixing on system characterization. In *Optical Fiber Communi-*

- cation Conference and Exposition and the National Fiber Optic Engineers Conference (OFC/NFOEC), 2013, pages 1–3, 2013.
- [133] E. Desurvire, C. Kazmierski, F. Lelarge, X. Marcadet, André Scavennec, F.A. Kish, D.F. Welch, R. Nagarajan, C.H. Joyner, R.P. Schneider Jr., S.W. Corzine, M. Kato, P.W. Evans, M. Ziari, A.G. Dentai, J.L. Pleumeekers, R. Muthiah, S. Bigo, M. Nakazawa, D.J. Richardson, F. Poletti, M.N. Petrovich, S.U. Alam, W.H. Loh, and D.N. Payne. Science and technology challenges in {XXIst} century optical communications. *Comptes Rendus Physique*, 12(4):387 – 416, 2011. <ce:title>Quantum Hall Effect and Metrology</ce:title> <ce:subtitle>Effet Hall quantique et métrologie</ce:subtitle>.
  - [134] F.P. Kapron, D.B. Keck, and R. D. Maurer. Radiation losses in glass optical waveguides. *Applied Physics Letters*, 17(10):423–425, 1970.
  - [135] Peter C Schultz. Fabrication of optical waveguides by the outside vapor deposition process. *Proceedings of the IEEE*, 68(10):1187–1190, 1980.
  - [136] John B. MacChesney. Materials and processes for preform fabrication. modified chemical vapor deposition and plasma chemical vapor deposition. *Proceedings of the IEEE*, 68(10):1181–1184, 1980.
  - [137] H. Osanai, T. Shioda, T. Moriyama, S. Araki, M. Horiguchi, T. Izawa, and H. Takata. Effect of dopants on transmission loss of low-oh-content optical fibres. *Electronics Letters*, 12(21):549–550, 1976.
  - [138] Charlene M Smith, Natesan Venkataraman, Michael T Gallagher, Dirk Müller, James A West, Nicholas F Borrelli, Douglas C Allan, and Karl W Koch. Low-loss hollow-core silica/air photonic bandgap fibre. *Nature*, 424(6949):657–659, 2003.
  - [139] B.J. Mangan, L. Farr, A. Langford, P.J. Roberts, D. P. Williams, F. Couny, M. Lawman, M. Mason, S. Coupland, R. Flea, H. Sabert, T.A. Birks, J.C. Knight, and P.S.J. Russell. Low loss (1.7 db/km) hollow core photonic bandgap fiber. In *Optical Fiber Communication Conference, 2004. OFC 2004*, volume 2, pages 3 pp. vol.2–, 2004.
  - [140] P. J. Roberts, F. Couny, H. Sabert, B. J. Mangan, D. P. Williams, L. Farr, M. W. Mason, A. Tomlinson, T. A. Birks, J. C. Knight, and P. St.J. Russell. Ultimate low loss of hollow-core photonic crystal fibres. *Opt. Express*, 13(1):236–244, Jan 2005.
  - [141] J. K. Lyngsø, B. J. Mangan, C. Jakobsen, and P. J. Roberts. 7-cell core hollow-core photonic crystal fibers with low loss in the spectral region around 2  $\mu\text{m}$ . *Opt. Express*, 17(26):23468–23473, Dec 2009.
  - [142] Natalie V. Wheeler, Marco N. Petrovich, Radan Slavik, Naveen K. Baddela, Eric Rodrigue Numkam Fokoua, John R. Hayes, David Gray, Francesco Poletti, and David Richardson. Wide-bandwidth, low-loss, 19-cell hollow core photonic

- band gap fiber and its potential for low latency data transmission. In *National Fiber Optic Engineers Conference*, page PDP5A.2. Optical Society of America, 2012.
- [143] Naoise Mac Suibhne, Zhihong Li, Benedikt Baeuerle, Jian Zhao, John Wooler, Shaif ul Alam, Francesco Poletti, Marco Petrovich, Alexander Heidt, Natalie Wheeler, Naveen Baddela, Eric Rodrigue Numkam Fokoua, Ian Giles, Dean Giles, Richard Phelan, John O'Carroll, Brian Kelly, Brian Corbett, Dominic Murphy, Andrew D. Ellis, David J. Richardson, and Fatima Garcia Gunning. Wdm transmission at 2 $\mu$ m over low-loss hollow core photonic bandgap fiber. In *Optical Fiber Communication Conference/National Fiber Optic Engineers Conference 2013*, page OW1I.6. Optical Society of America, 2013.
- [144] KC Kao and George A Hockham. Dielectric-fibre surface waveguides for optical frequencies. *Electrical Engineers, Proceedings of the Institution of*, 113(7):1151–1158, 1966.
- [145] Tingye Li. Advances in optical fiber communications: An historical perspective. *Selected Areas in Communications, IEEE Journal on*, 1(3):356–372, 1983.
- [146] S.E. Miller and A. C. Beck. Low-loss waveguide transmission. *Proceedings of the IRE*, 41(3):348–358, 1953.
- [147] J.H. Bryant. Coaxial transmission lines, related two-conductor transmission lines, connectors, and components: A u.s. historical perspective. *Microwave Theory and Techniques, IEEE Transactions on*, 32(9):970–981, 1984.
- [148] R. D. Maurer. Light scattering by glasses. *The Journal of Chemical Physics*, 25(6):1206–1209, 1956.
- [149] Andrew D. Ellis and N. Mac Suibhne. The mode-gap project. In *Frontiers in Optics 2012/Laser Science XXVIII*, page FW1D.1. Optical Society of America, 2012.
- [150] R. Phelan, J. O'Carroll, D. Byrne, C. Herbert, J. Somers, and B. Kelly. In<sub>0.75</sub>Ga<sub>0.25</sub>As/InP multiple quantum-well discrete-mode laser diode emitting at 2  $\mu$  m. *Photonics Technology Letters, IEEE*, 24(8):652–654, 2012.
- [151] I. Hayashi, M.B. Panish, P.W. Foy, and S. Sumski. Junction lasers which operate continusly at room temperature. *Applied Physics Letters*, 17(3):109–111, 1970.
- [152] CA Burrus and BI Miller. Small-area, double-heterostructure aluminum-gallium arsenide electroluminescent diode sources for optical-fiber transmission lines. *Optics Communications*, 4(4):307–309, 1971.
- [153] J.J. Hsieh, J. Rossi, and J.P. Donnelly. Room-temperature cw operation of gainasp/inp double-heterostructure diode lasers emitting at 1.1  $\mu$ m. *Applied Physics Letters*, 28(12):709–711, 1976.

- [154] "Eblana Photonics", Accessed on 9 Nov 2013. <http://www.eblanaphotonics.com/>.
- [155] S. Bouchoule, J. Decobert, S. Grosmaire, D. Leclerc, and C. Kazmierski. Low-capacitance laser heterostructure selectively buried in si-inalas by ap-movpe. In *Optical Communication, 2001. ECOC '01. 27th European Conference on*, volume 2, pages 120–121 vol.2, 2001.
- [156] Hideki YAGI, Yutaka ONISHI, Kenji KOYAMA, Yukihiro TSUJI, Hiroyuki ICHIKAWA, Hiroyuki YOSHINAGA, Noriaki KAIDA, Toshio NOMAGUCHI, Kenji HIRATSUKA, and Katsumi UESAKA. 1.3  $\mu\text{m}$  wavelength algainas/inp ridge-waveguide lasers utilizing benzocyclobutene planarization process. *SEI TECHNICAL REVIEW*, (69):93, 2009.
- [157] H. Yang, N. Ye, R. Phelan, J. O'Carroll, B. Kelly, W. Han, X. Wang, N. Nudds, N. MacSuibhne, F. Gunning, P. O'Brien, F.H. Peters, and B. Corbett. Butterfly packaged high-speed and low leakage ingaas quantum well photodiode for 2000nm wavelength systems. *Electronics Letters*, 49(4):281–282, 2013.
- [158] Z. Li, A. M. Heidt, J. M. O. Daniel, Y. Jung, S. U. Alam, and D. J. Richardson. Thulium-doped fiber amplifier for optical communications at 2  $\mu\text{m}$ . *Opt. Express*, 21(8):9289–9297, Apr 2013.
- [159] "OFS RightWave™ Ytterbium and Thulium Doped Fibre". ofscatalog.specialtyphotronics.com. Accessed on 9 Oct 2013. <http://ofscatalog.specialtyphotronics.com/viewitems/al-fibers-edf-fiber-lasers-and-other-light-sources/r-light-sources-ytterbium-and-thulium-doped-fibers>.
- [160] Marco N. Petrovich, Francesco Poletti, John Wooler, Alexander Heidt, Naveen K. Baddela, Zhihong Li, David R. Gray, Radan Slavík, Francesca Parmigiani, Natalie Wheeler, John Hayes, Eric Numkam Fokoua, Lars Grüner-Nielsen, Bera Pálsdóttir, Richard Phelan, Brian Kelly, Martin Becker, Naoise MacSuibhne, Jian Zhao, Fatima C. Garcia Gunning, Andrew Ellis, Periklis Petropoulos, Shaif ul Alam, and David Richardson. First demonstration of 2 $\mu\text{m}$  data transmission in a low-loss hollow core photonic bandgap fiber. In *European Conference and Exhibition on Optical Communication*, page Th.3.A.5. Optical Society of America, 2012.
- [161] "HITRAN Database 2012". Registered access through Harvard-Smithsonian Center for Astrophysics. Accessed on June 2013. <http://hitran.iaao.ru/>.
- [162] "Phoenix Photonics", Accessed on 9 Nov 2013. <http://phoenixphotronics.com/>.
- [163] Jian Zhao, S.K. Ibrahim, D. Rafique, P. Gunning, and Andrew D. Ellis. Symbol

- synchronization exploiting the symmetric property in optical fast ofdm. *Photonics Technology Letters, IEEE*, 23(9):594–596, 2011.
- [164] John Wooler, David Gray, Francesco Poletti, Marco Petrovich, Natalie Wheeler, Francesca Parmigiani, and David J. Richardson. Robust low loss splicing of hollow core photonic bandgap fiber to itself. In *Optical Fiber Communication Conference/National Fiber Optic Engineers Conference 2013*, page OM3I.5. Optical Society of America, 2013.

# Appendix A

## Author's Publications

- A1. Andrew D Ellis and Naoise Mac Suibhne. The mode-gap project. In *Frontiers in Optics*. Optical Society of America, 2012.
- A2. Andrew D Ellis, Naoise Mac Suibhne, Fatima Garcia Gunning, and Stylianos Sygletos. Expressions for the nonlinear transmission performance of multi-mode optical fiber. *Opt. Express*, 21(19):22834–22846, 2013.
- A3. Naoise Mac Suibhne, AD Ellis, FC Gunning, and S Sygletos. Experimental verification of four wave mixing efficiency characteristics in a few mode fibre. In *39th European Conference and Exhibition on Optical Communication (ECOC 2013)*, pages 1–3. IET, 2013.
- A4. Naoise Mac Suibhne, Zhihong Li, Benedikt Baeuerle, Jian Zhao, John Wooler, Shaif-ul Alam, Francesco Poletti, Marco Petrovich, Alexander Heidt, Natalie Wheeler, Naveen Baddela, Eric Rodrigue Numkam Fokoua, Ian Giles, Dean Giles, Richard Phelan, John O'Carroll, Brian Kelly, Brian Corbett, Dominic Murphy, Andrew D. Ellis, David J. Richardson, and Fatima Garcia Gunning. WDM transmission at 2 $\mu$ m over low-loss hollow core photonic bandgap fiber. In *Optical Fiber Communication Conference 2013*. Optical Society of America, 2013.
- A5. Naoise Mac Suibhne, Zhihong Li, Benedikt Baeuerle, Jian Zhao, John P Wooler, Shaif-ul Alam, Francesco Poletti, Marco N Petrovich, Alexander Heidt, Ian Giles, Dean J. Giles, Bera Pálsdóttir, Lars Grüner-Nielsen, Richard Phelan, John O'Carroll, Brian Kelly, Dominic Murphy, Andrew Ellis, David Richardson, and Fatima C. Garcia Gunning. Wavelength division multiplexing at 2 $\mu$ m. In *European Conference and Exhibition on Optical Communication 2012*. Optical Society of America, 2012. (Post-Deadline)
- A6. Naoise Mac Suibhne, ReganWatts, Stylianos Sygletos, Fatima C Garcia Gunning, Lars Grüner-Nielsen, and Andrew Ellis. Nonlinear pulse distortion in few-mode



- fiber. In *European Conference and Exhibition on Optical Communication 2012*. Optical Society of America, 2012.
- A7. LE Nelson, X Zhou, N Mac Suibhne, Andrew D Ellis, and P Magill. Experimental comparison of coherent polarization-switched QPSK to polarization-multiplexed QPSK for 10×100 km WDM transmission. *Opt. Express*, 19(11):10849–10856, 2011.
- A8. Marco N Petrovich, Francesco Poletti, John Wooler, Alexander Heidt, Naveen K Baddela, Zhihong Li, David R Gray, Radan Slavík, Francesca Parmigiani, Natalie Wheeler, John Hayes, Eric Numkam Fokoua, Lars Grüner-Nielsen, Bera Pálsdóttir, Richard Phelan, Brian Kelly, Martin Becker, Naoise Mac Suibhne, Jian Zhao, Fatima C. Garcia Gunning, Andrew Ellis, Periklis Petropoulos, Shaif-ul Alam, and David Richardson. First demonstration of 2µm data transmission in a low-loss hollow core photonic bandgap fiber. In *European Conference and Exhibition on Optical Communication 2012*. Optical Society of America, 2012. (Post-Deadline)
- A9. MN Petrovich, F Poletti, JP Wooler, AM Heidt, NK Baddela, Z Li, DR Gray, R Slavík, F Parmigiani, NV Wheeler, JR Hayes, E Numkam, L Grüner-Nielsen, B Pálsdóttir, R Phelan, B Kelly, J O'Carroll, M Becker, N Mac Suibhne, J Zhao, FC Garcia Gunning, AD Ellis, P Petropoulos, SU Alam, DJ Richardson. Demonstration of amplified data transmission at 2µm in a low-loss wide bandwidth hollow core photonic bandgap fiber. *Opt. Express*, 21(23):28559–28569, 2013.
- A10. Naoise Mac Suibhne, Regan Watts, Stylianos Sygletos, Fatima C Garcia Gunning, Lars Gruner-Nielsen, and Andrew D Ellis. Nonlinear soliton propagation in a few mode optical fibre. In *17th Opto-Electronics and Communications Conference (OECC), 2012*, pages 497–498. IEEE, 2012.
- A11. H Yang, N Ye, R Phelan, J O'Carroll, B Kelly, W Han, X Wang, N Nudds, N Mac-Suibhne, F Gunning, P O'Brien, FH Peters, B Corbett. Butterfly packaged high-speed and low leakage InGaAs quantum well photodiode for 2000nm wavelength systems. *Electronics Letters*, 49(4):281–282, 2013.

### A.0.1 Publications Not Related to This Thesis

- B1. Paola Frascella, Naoise Mac Suibhne, Fatima C Garcia Gunning, Selwan K Ibrahim, Paul Gunning, Andrew D Ellis. Unrepeated field transmission of 2 Tbit/s multi-banded coherent WDM over 124 km of installed SMF. *Opt. Express* 18 (24), 24745-24752.
- B2. Andrew D Ellis, Fatima C Garcia Gunning, Jian Zhao, Selwan K Ibrahim, Paola Frascella, Naoise MacSuibhne, Francesca Parmigiani, Radan Slavík, Joseph Kakande, Carl Lundström, Martin Sjödin, Peter Andrekson, Ruwan Weera-

suriya, Stylianos Sygletos, Lars Grüner-Nielsen, D Jakobsen, Søren Herstrøm, Richard Phelan, James O'Gorman, Adonis Bogris, Dimitri Syvridis, Sonali Dasgupta, Periklis Petropoulos, David J Richardson. Future Directions to Realize Ultra-High Bit-Rate Transmission Systems. *Proceedings of OptoElectronics and Communications Conference, OECC 2010, Sapporo, Japan, 5-9 July 2010*, invited paper.

- B3. R Freund, M Nolle, C Schmidt-Langhorst, R Ludwig, C Schubert, G Bosco, A Carena, P Poggiolini, L Oxenløwe, Michael Galili, HC Hansen Mulvad, M Winter, D Hillerkuss, R Schmogrow, W Freude, J Leuthold, AD Ellis, FC Garcia Gunning, J Zhao, P Frascella, SK Ibrahim, N Mac Suibhne. Single-and multi-carrier techniques to build up Tb/s per channel transmission systems. *12th International Conference on Transparent Optical Networks (ICTON)*, 1-7, 2010.